DEVELOPMENT OF PPLN BASED MID-WAVE INFRARED TRANSMITTER AND RECEIVER FOR SATCOM

DEVELOPMENT OF PPLN BASED MID-WAVE INFRARED TRANSMITTERS AND RECEIVERS FOR OPTICAL SATELLITE COMMUNICATION

By LIAM FLANNIGAN, B.ENG.

A Thesis Submitted to the School of Graduate Studies in Partial Fulfilment of the Requirements for the Degree Doctor of Philosophy

McMaster University

Doctor of Philosophy (2025) McMaster University

Department of Engineering Physics Hamilton, Ontario

TITLE: MID-WAVE INFRARED TRANSMITTERS AND RECEIVERS FOR OPTICAL SATELLITE COMMUNICATION

AUTHOR: Liam Flannigan, B.Eng. (McMaster University).

SUPERVISOR: Dr. Chang-qing Xu, Ph.D.

NUMBER OF PAGES: xxii, 176

i Abstract

Recent advances in optical satellite communication (SatCom) have demonstrated the potential of laser-based systems to surpass traditional radio-frequency methods in terms of data rates, size, weight, and power efficiency (SWaP). A series of international proof-of-concept missions over the past several decades have showcased the feasibility of optical SatCom, most utilizing short-wave infrared (SWIR, 0.8-1.7 μm) wavelengths due to their favorable atmospheric transmission and the maturity of terrestrial telecom-derived technologies. However, SWIR systems suffer from severe performance degradation under adverse weather conditions such as haze, fog, and clouds. This remains an unsolved challenge that limits system reliability.

This thesis addresses this challenge by proposing a novel optical transmitter/receiver pair operating in the mid-wave infrared band (MWIR, 3–5 μm), which is significantly less affected by atmospheric scattering and turbulence. The key innovation lies in leveraging nonlinear optical processes to achieve compact, high-speed wavelength conversion. A proprietary intracavity design enables efficient conversion of 1550 nm C-band laser light into 3.4 μm (MWIR) at the transmitter, and then back into 810 nm SWIR light at the receiver, using difference frequency generation (DFG) and sum frequency generation in a periodically poled lithium niobate (PPLN) nonlinear crystal, respectively. This two-stage conversion strategy allows the use of commercially available, high-speed C-band laser sources and high-performance SWIR silicon detectors, preserving the information

bandwidth of the original signal throughout the optical link while offering significant gains in overall detectivity versus direct MWIR detectors.

In this thesis, a proof-of-principle prototype for the transmitter and receiver system is designed, built, and experimentally characterized. A novel model that combines a spatially dependent rate equation laser simulation with a two-dimensional gaussian nonlinear three-wave coupling simulation is presented as well. The experimental results agree well with the model, and further optimizations relating to cavity design and beam overlap in the nonlinear medium are identified for future work.

ii Acknowledgments

First and foremost, I would like to express my deepest gratitude to my supervisor, Dr. Chang-qing Xu, for his unending support, guidance, and mentorship throughout this journey. His expertise and encouragement helped shape this research and allowed me to develop many skills that I will use throughout my career. I am sincerely thankful for the opportunities he provided me with. I am also grateful to the members of my advisory committee, Dr. Jonathan Bradley and Dr. Adrian Kitai. Their thoughtful feedback, constructive criticism, and the time they generously dedicated to reviewing my work have made me a better scientist.

To my lab mates, colleagues, and friends in the department, thank you for the camaraderie and stimulating discussions that made even the most stressful days manageable. I especially want to acknowledge Tyler Kashak, Andres Gustavo Escobar Moya, and Alexandre Chiasson. Your help in the lab and the frequent games of Magic the Gathering outside of the lab kept me sane and were a highlight of my time at McMaster. I look forward to staying friends and to seeing what accomplishments the future holds in store for all of you.

I would like to thank Brendan, Hani, Geoff, Shaun, and Gabe for the countless hours of escapism shared over games of Pathfinder and Delta Green. Your warm welcome into the group and the absurd and thrilling stories we've created together provided a much-needed refuge from the stresses of thesis work. Those evenings of dice rolls and dark humor

were a reminder that even in the most chaotic of times, there's always room for imagination, laughter, and friendship. I look forward to many more adventures yet to come.

I am profoundly grateful to my friends, Gemma Gjorkes and Colleen Armstrong, for their steadfast presence throughout this journey. Gemma's frequent support and grounded perspective were a lifeline during the most difficult and demanding phases of this work. Her friendship has been nothing short of essential. Colleen's boundless optimism, patience, and warmth were a constant source of light; her encouragement helped me carry on when I felt overwhelmed. They were always there to listen when I needed to vent, and I truly could not have completed this PhD without the strength and joy that both of them brought into my life.

On a personal note, I would like to thank my late mother, Marie Adema, whose support was my foundation. For her advice, her patience, and her faith, because she always understood. Though she did not get to see this thesis completed, her strength, kindness, and sacrifices have carried me through every step of this journey. Her memory continues to inspire me, and I dedicate this work to her with all my heart.

Finally, to everyone who helped me along the way — in ways big and small — thank you. This thesis stands as much on your shoulders as on mine.

"*I have lived and fulfilled a dream, and yet my life is just beginning."*

- Unknown

iii Table of Contents

iv List of Figures

v List of Tables

vi List of Abbreviations

SWIR – Short Wave Infrared

MWIR – Mid Wave Infrared

PPLN – Periodically Poled Lithium Niobate

SFG – Sum Frequency Generation

DFG – Difference Frequency Generation

QPM – Quasi Phase Matching

OC – Output Coupler

DPSS – Diode Pumped Solid State

Nd:YVO4 – Neodymium Doped Yttrium Orthovanidate

Nd:YAG – Neodymium Doped Yttrium Aluminum Garnet

FWHM – Full Width Half Maximum

QCL – Quantum Cascade Laser

AR - Anti Reflection

HR – High Reflection

ISS - International Space Station

NICT - National Institute of Information and Communications Technology

HT - High Transmission

TEC - Thermo Electric Cooler

NEP - Noise Equivalent Power

RF - Radio Frequency

DFB - Distributed Feedback

OPO - Optical Parametric Oscillator

IEEE - Institute of Electrical and Electronics Engineers

vii Declaration of Authorship

I, Liam Flannigan, declare that this thesis "PPLN Based Mid-Wave Infrared Transmitters And Receivers For Optical Satellite Communication", was authored by and contains research work performed by the author, in consultation with Dr. Chang-qing Xu. To the best of my knowledge this thesis contains no material published by any other person except where due acknowledgement has been made. This thesis contains no material which has been accepted as part of the requirements of any other academic degree or non-degree program, in English or in any other language.

This thesis has resulted in several published journal papers in which I am the first author or shared first author. There have also been several co-authored publications, conference proceedings, and awarded patents. For completeness, these have been listed below, although please note that only the non-review article first author papers feature as chapters of this thesis.

1. **First Author Publications**

    a. **L. Flannigan,** T. Kashak, and C.Q. Xu, "Study of fundamental wave depletion in intracavity second harmonic generation," Opt. Express 29, 6810-6823 (2021).

b. **L. Flannigan,** L. Yoell, C.Q. Xu, "Mid-wave and long-wave infrared transmitters and detectors for optical satellite communications – a review," J. Opt. 24 043002 (2022). Doi: 10.1088/2040-8986/ac56b6

c. **L. Flannigan,** A. Atwi, T. Kashak, Daniel Poitras, and C.Q. Xu, "Compact Diode-Pumped Solid-State Laser with Intracavity Pump-Enhanced DFG Emitting at ~3.5 Microns," Photonics vol. 10 no. 10, 1164 (2023).

d. T. Kashak*, **L. Flannigan*,** A. Atwi, Daniel Poitras, and C.Q. Xu, "Compact Intracavity Mid-Infrared Upconversion Detector – A Systematic Study," Opt. Continuum 3, 1660-1678 (2024). (* denotes shared first authorship due to equally significant contributions).

2. **Conference Publications**

a. **L. Flannigan** and C. Q. Xu, “LWIR FSO Receivers using Orientation Patterned Semiconductors,” in 2022 Photonics North (PN), May 2022, pp. 1–1. doi: 10.1109/PN56061.2022.9908335.

b. **L. Flannigan** and C. Q. Xu, “Comparison of near-infrared and mid-infrared link budgets for optical satellite communication,” in 2022 Photonics North (PN), May 2022, pp. 1–2. doi: 10.1109/PN56061.2022.9908400.

c. D. Poitras, **L. Flannigan**, and C. Q. Xu, "Optical Coatings for mid-IR DFG-based Next Generation Transceivers for Optical SATCOM," in Optical Interference Coatings Conference (OIC) 2022, R. Sargent and A. Sytchkova, eds., Technical Digest Series (Optica Publishing Group, 2022), paper WA.3.

d. **L. Flannigan**, A. Atwi, T. Kashak, D. Poitras and C. Q. Xu, "High Efficiency Pump-Enhanced Difference Frequency Generation for Mid-IR Communications," *2024 Photonics North (PN)*, Vancouver, BC, Canada, 2024, pp. 1-2, doi: 10.1109/PN62551.2024.10621807.

e. R. Cheriton, **L. Flannigan**, S. S. Rizi, M. Khalil, M. Gadalla, D. Poitras, L. Graham, and C. Q. Xu, "Towards a Long-Range Mid-Infrared Optical Communication Testbed for Weather-Resistant Optical SatCom using C-band transmitters and silicon detectors", Photonics North, 2025, Ottawa, ON, Canada, paper 256-ecHG-152.

3. **Co-authored Journal Publications**

a. M. Mohamed, M. A. Qianli, **L. Flannigan**, and C. Q. Xu, "Laser speckle reduction utilized by lens vibration for laser projection applications," Eng. Res. Express, vol. 1, no. 1, p. 015036, Sep. 2019, doi: 10.1088/2631-8695/ab42eb.

b. T. Kashak, **L. Flannigan**, and C. Q. Xu, "A systematic study of PPLN length dependence in intracavity SHG," *Sci Rep*, vol. 11, no. 1, p. 22246, Nov. 2021, doi: 10.1038/s41598-021-01699-0.

c. J. Kneller, **L. Flannigan**, and C. Q. Xu, "Theoretical study of diode pumped intracavity backward optical parametric oscillator based on periodically poled lithium niobate," *Appl. Phys. B*, vol. 129, no. 6, p. 99, May 2023, doi: 10.1007/s00340-023-08045-4.

d. J. Kneller, **L. Flannigan**, and C. Q. Xu, "Design Considerations for Continuous Wave Intracavity Backwards Optical Parametric Oscillators," *Photonics*, vol. 11, no. 4, Art. no. 4, Apr. 2024, doi: 10.3390/photonics11040318.

e. J. Kneller, S. Salimian Rizi, **L. Flannigan**, and C. Q. Xu, "The effects of thermalization on the performance of passively Q-switched IC-OPOs," *Front. Phys.*, vol. 12, Jul. 2024, doi: 10.3389/fphy.2024.1428671.

f. B. Zhang, Q. Ma, **L. Flannigan**, and C. Q. Xu, "Tri-wavelength blending method for speckle reduction and color space enhancement in laser projection systems," *Displays*, vol. 84, p. 102748, Sep. 2024, doi: 10.1016/j.displa.2024.102748.

g. S. Salimian Rizi, **L. G. K. Flannigan**, A. Chiasson, T. Kashak, D. Poitras, and C. Q. Xu, "Efficient, Compact Mid-Infrared Sources: A Systematic Study of Intracavity Difference-Frequency Generation," *Photonics*, vol. 12, no. 1, Art. no. 1, Jan. 2025, doi: 10.3390/photonics12010025.

4. **Patents**

a. C. Q. Xu, **L. Flannigan**, and J. Kneller, "Laser apparatus and method," US20230128226A1, Apr. 27, 2023 Accessed: Jun. 09, 2025. [Online]. Available: https://patents.google.com/patent/US20230128226A1/en

b. C. Q. Xu, J. Kneller, and **L. Flannigan**, "Mid-infrared wavelength optical transmitter and receiver," US11815783B2, Nov. 14, 2023 Accessed: Jun. 09, 2025. [Online]. Available: https://patents.google.com/patent/US11815783B2/en

c. C. Q. Xu, **L. Flannigan**, and J. Kneller, "Apparatus of optical transmitters and receivers operating in long wave infrared wavelength ranges," CA3135390A1, Apr. 21, 2022 Accessed: Jun. 09, 2025. [Online]. Available: https://patents.google.com/patent/CA3135390A1/en?inventor=Liam+Flannigan

d. C. Q. Xu, **L. Flannigan**, J. Kneller, and F. J. M. Jr, "Measuring concentrations of mixed gases at an endpoint," US11879866B2, Jan. 23, 2024 Accessed: Jun. 09, 2025. [Online]. Available: https://patents.google.com/patent/US11879866B2/en

e. C. Q. Xu, M. M. T. M. I. E. K. Mohamed, **L. Flannigan**, and Q. Ma, "Speckle reduced laser image projection method and apparatus," WO2020202011A1, Oct. 08, 2020 Accessed: Jun. 09, 2025. [Online]. Available: https://patents.google.com/patent/WO2020202011A1/en?inventor=Liam+Flannigan

5. Papers Submitted/Under Review

a. V. Theenathayalan, C. Binding, **L. Flannigan**, N. Pahlevan, R. O'Shea, G. Gariépy, "Assessing PRISMA performance for water quality retrievals in Lake Erie," Remote Sensing of Environment, Manuscript Number RSE-D-25-02224, Under Review (2025).

Chapter 1. Introduction

1.1 Background and Motivation

The demand for increased satellite communication bandwidth has grown significantly in recent years, driven by the proliferation of advanced spaceborne sensors and the rapidly expanding data requirements of both scientific and commercial missions. Applications such as high-resolution Earth observation, deep-space exploration, and global broadband internet provision have pushed the limits of conventional radio frequency (RF) communication systems. In response, optical satellite communication (SatCom) has emerged as a compelling alternative, offering the promise of higher data rates, improvements in payload size, weight, and power efficiency (SWaP), increased security through narrower beam divergence, and better spectrum availability.

Interest in optical SatCom has accelerated in the past two decades, as evidenced by a series of successful proof-of-concept missions. These include the first inter-satellite optical link between Artemis and SPOT 4 (2001), satellite-to-ground communication via TerraSAR-X and NFIRE (2008), and high-speed links such as NASA's OPALS mission (2014), which demonstrated 400 Mbps downlinks and link re-acquisition following weather disruption [1], [2], [3]. More recently, missions like JAXA's SOLISS (2017) and the HICALI project (2018) illustrate

sustained international commitment to the maturation of optical communication technologies for space applications [4], [5]. There are many more recent missions to choose from, but this representative sample should demonstrate that interest in the field is high.

Most of these demonstrations have employed laser systems operating within the short-wave infrared (SWIR) band (approximately 0.8–1.7 μm), owing largely to the commercial maturity of SWIR photonic components. SWIR lasers, including Nd:YAG and distributed feedback (DFB) semiconductor devices, benefit from widespread use in the telecommunications industry, offering watt-level optical powers and gigabit-per-second data rates at relatively low cost. Additionally, well-developed amplifier technologies such as erbium-doped fiber amplifiers (EDFAs) enable further enhancement of SWIR link performance. However, a critical limitation of SWIR systems is their vulnerability to adverse weather conditions. Phenomena such as fog, clouds, and precipitation can introduce severe attenuation in the optical channel, dramatically reducing link availability and reliability, particularly in high-latitude or high-humidity regions [6], [7], [8].

This limitation has prompted growing interest in the mid-wave infrared (MWIR, 3–5 μm) spectral region as a potential alternative for robust optical communication. Atmospheric propagation models and terrestrial experimental data suggest that these longer wavelengths exhibit reduced scattering and absorption under inclement weather conditions compared to SWIR. The transmission spectrum in Figure 1-1

also shows that atmospheric transmission is high over a majority of the MWIR window, making it a suitable candidate for long distance transmission. Consequently, MWIR systems may offer improved link resilience, particularly in ground-to-satellite scenarios where atmospheric effects are more pronounced. Despite these promising indications, comprehensive evaluations of MWIR photonic components, particularly in terms of their suitability for high-speed satellite communication, remain limited in the literature.

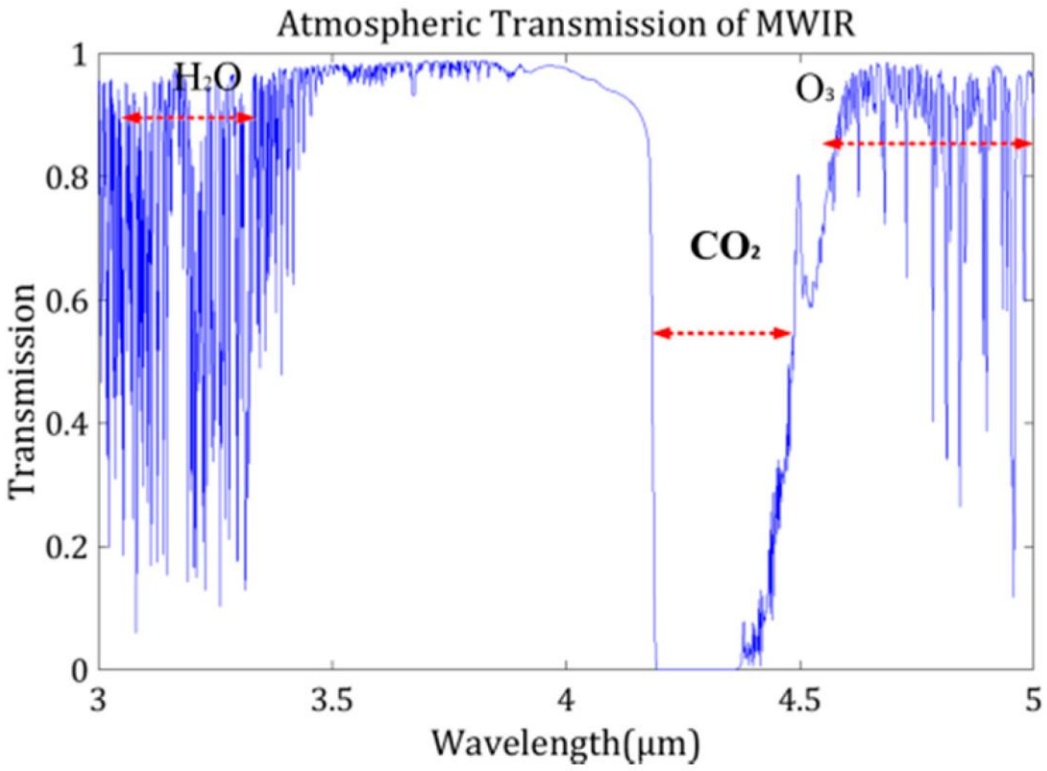

Figure 1-1 Diagram depicting the atmospheric transmission in MWIR. It is clear that from 3.5 microns to ~4.1 microns the transmission is quite high and relatively stable, making it a strong candidate for free space communication. [9]

When considering a laser-based SatCom link, the enabling components are the optical source for the transmitter and the detector used for the receiver. The author has previously published a review article covering the pros and cons of different optical sources and mid-infrared detectors [10]. What follows is a summarized version of the conclusions from the article. Fig 1-2 shows the general idea behind the mid-infrared links the proposed transmitter and receiver could be used for.

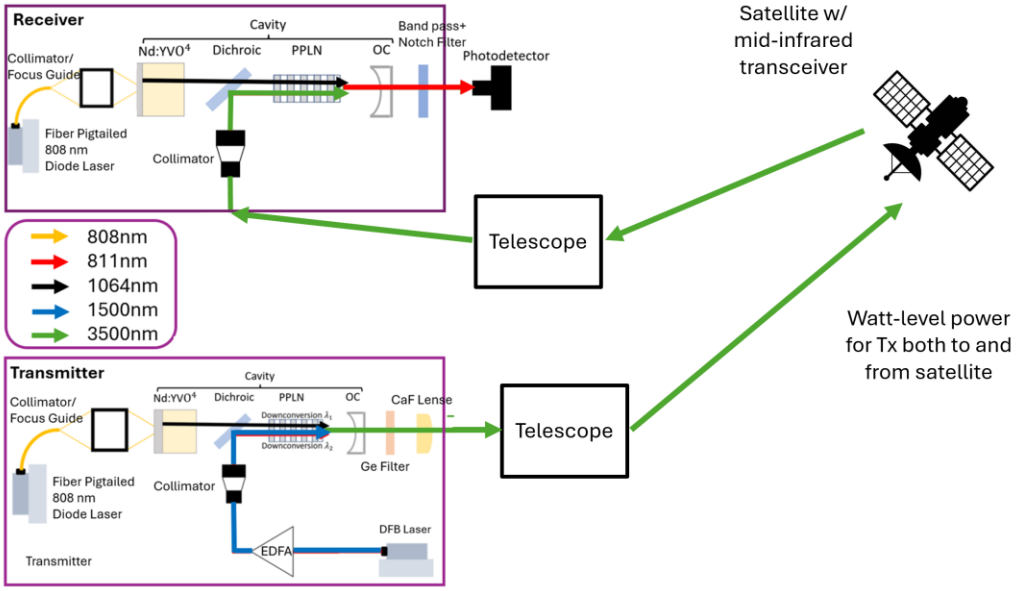

Figure 1-2 The envisioned LEO link the proposed transmitter and receiver technology might be used for. Watt-level power ensures sufficient link budget to reach the satellite in LEO, and the satellite is equipped with similar transmitter and receiver technology to convert the mid-infrared signal and re-transmit it to ground as needed.

An optical source for SatCom must have sufficient output power, modulation bandwidth, and beam quality to support high-data-rate transmission through

atmospheric channels. Three primary classes of optical sources have emerged as promising candidates for MWIR links: quantum cascade lasers (QCLs), nonlinear wavelength conversion systems, and rare-earth-doped fiber lasers.

Quantum cascade lasers (QCLs) are among the most mature MWIR laser technologies, offering direct emission in the desired wavelength range through intersubband transitions in semiconductor quantum wells [11]. QCLs can be engineered for specific wavelengths within the MWIR band by tailoring the active region design, providing an excellent degree of wavelength selectivity. They can provide continuous-wave output with watt-level powers, and their compact, electrically pumped architecture is well-suited for satellite payloads. Additionally, they have modulation bandwidths in the GHz thanks to short carrier lifetimes, meaning they can be directly modulated at gigabit speeds [12]. The main challenge with QCLs is thermal management, as their performance depends heavily on maintaining a stable operating temperature. An added challenge to this is that many QCLs only perform optimally at cryogenic temperatures, limiting their usefulness for satellite payloads where cryogenic cooling is not feasible. This means there can be a trade-off between cooling and device efficiency, although cascade laser operating temperatures have improved in recent years [13]. Nonetheless, QCLs remain a promising candidate for MWIR transmission.

Nonlinear wavelength converters present another approach to generating MWIR light by leveraging well-established SWIR laser sources. Techniques such as

difference frequency generation (DFG) or optical parametric oscillation (OPO) allow the conversion of near-infrared pump beams into mid-infrared output via nonlinear crystals (e.g., periodically poled lithium niobate (PPLN)) [14]. These systems benefit from the maturity of telecom-band lasers and can achieve high beam quality and tunability [15]. However, their complexity, alignment sensitivity, and relatively low overall conversion efficiencies pose challenges for deployment in space environments, particularly where size, weight, and power (SWaP) constraints are critical.

Lastly, rare-earth-doped fiber lasers doped with dysprosium (Dy^{3+}) offer the potential for efficient lasing beyond 2.7 μm, potentially extending into the MWIR band with proper fiber and pump configurations [16]. These systems can deliver high-quality beams and leverage the modularity and robustness of fiber-based designs. Nevertheless, their development is less mature than QCLs, and performance in the 3–5 μm range is still an active area of research, particularly regarding fiber transparency, nonlinear effects, and thermal management. One notable hurdle to overcome is the difficulty of modulating MWIR fiber lasers. There is a lack of effective external modulators in the MWIR region, and direct modulation of MWIR fiber lasers has not been demonstrated at speeds sufficient for high-speed data transmission [17].

In summary, while there is no obvious “most practical” MWIR laser source for near-term applications, ongoing advancements in nonlinear optics and cascade laser

technologies are posed to be promising options as the field progresses. Each technology brings its own trade-offs in terms of power, bandwidth, integration complexity, and space qualification. Nonlinear optics has the potential to offer stable room-temperature operation with bandwidth limits matching current commercial-off-the-shelf C-band (1550 nm) lasers. Additionally, the low conversion efficiencies could potentially be addressed by implementing compact intracavity designs, as nonlinear wavelength conversion efficiency is intensity dependent. Since laser intensity inside of an optical resonant cavity can be many times greater than the intensity outside of the cavity, this approach could solve one of the main issues with nonlinear approaches and make it a more compelling alternative to QCLs for optical SatCom.

While there is some competition for optical sources, there is a more noticeable gap in performance considering MWIR detectors. A useful figure-of-merit for comparing detectors is detectivity, measured in Jones. Detectivity can be thought of as the inverse of the noise-equivalent power for a detector that also factors out dependence on bandwidth and active area size. As such, high detectivities are a sign that a detector would generally outperform a detector with a lower detectivity if the bandwidth and active area size were the same between the two. Figure 1-3 reproduced from Rogalski et al. illustrates the main problem with MWIR detectors compared to the SWIR. There is a noticeable drop in detectivity as detection wavelength increases (gets longer). Top of the line direct MWIR detectors struggle

to breach detectivities on the order of 10^{10} Jones, while silicon detectors operating in the SWIR can reach detectivities several orders of magnitude higher.

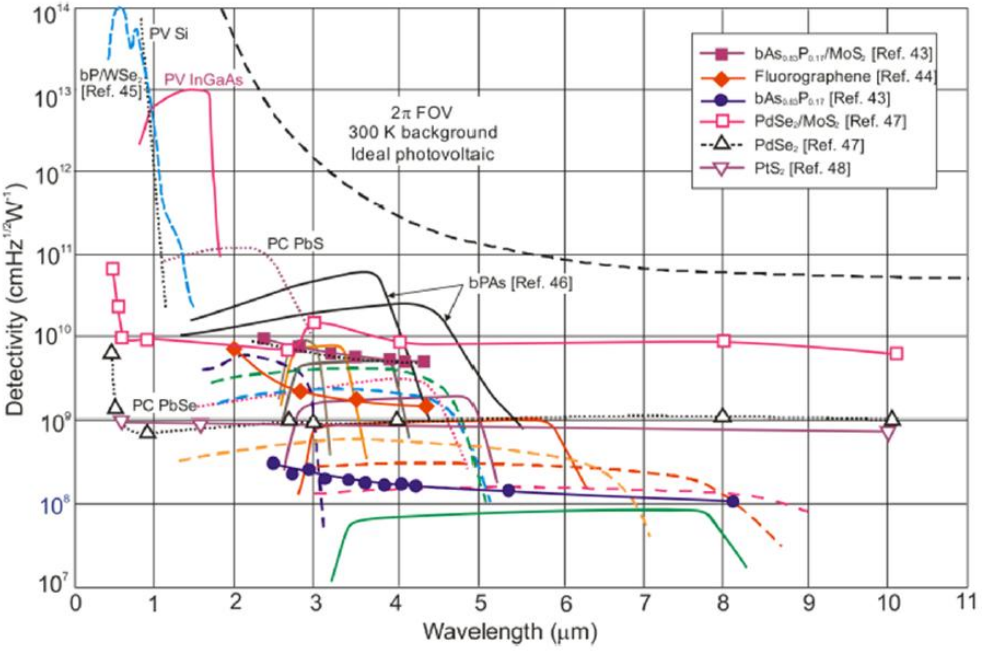

Figure 1-3 Room temperature detectivity values as a function of detection wavelength for a variety of modern MWIR detectors. The reference numbers in the legend can be found in the cited paper, and are separate from those in this thesis. [18]

This is a long-standing problem in direct MWIR detection. While there have been significant advancements in materials like InSb and Mercury Cadium Telluride (MCT), the performance gap with Silicon and InGaAs is quite large. A promising work-around is to convert the MWIR light to be detected into the SWIR region to take advantage of improved detector performance. This process is known as sum frequency generation (SFG) or upconversion. One of the earliest reports of mid-infrared upconversion was by Karstad et al. in 2005 [19]. A quantum cascade laser

was combined with a pump laser in periodically poled lithium niobate (PPLN), with the resulting upconverted light being detected via silicon APD. The authors noted that even with the experimental conversion efficiency being 50 times lower than the calculated efficiency (due to experimental error), the upconversion approach had the potential to outperform direct detection in terms of both speed and noise. This field has been an active area of research, although the majority of the literature focuses on single photon detection and mid-infrared imaging applications over communication applications. Creating a compact wavelength converter that could convert modulated MWIR light back into the SWIR band for use with high performance silicon detectors could significantly bridge the gap between MWIR and SWIR detection.

1.2 Thesis Objectives

The objectives of this research are to produce prototypes of both an intracavity DFG-based MWIR transmitter and an intracavity SFG-based MWIR receiver suitable for free space optical communications. The end result should be a systematic study of both devices outlining the relevant physical phenomena, modelling how they impact the efficiency and overall design of the proposed devices, and modelling work that is in good agreement with collected experimental data characterizing the performance of the prototypes.

The deployment of mid-infrared links in space-to-ground optical communications

presents a trade-off between improved atmospheric resilience and the penalties associated with longer wavelengths. Optical telescope gain decreases as the operational wavelength increases into the mid-IR. This reduction in gain implies that, to maintain comparable link budgets, larger aperture telescopes are required with corresponding penalties in size, weight, and power (SWaP). Despite this drawback, mid-IR wavelengths offer substantial benefits in terms of reduced sensitivity to adverse weather conditions, turbulence, and scintillation, making them attractive for more robust link performance under less-than-ideal atmospheric conditions.

When considering orbital regimes, these factors weigh differently. For geosynchronous orbit (GEO) and highly elliptical orbit (HEO) missions, the extremely long propagation distances impose stringent requirements on optical gain and beam divergence, making the larger apertures required for mid-IR operation especially challenging to accommodate. Additionally, most of the propagation distance in these orbits takes place in vacuum, limiting the overall link budget gain from switching to a longer wavelength. Similarly, for medium Earth orbit (MEO), link distances are sufficiently long that the loss of telescope gain becomes a limiting factor for practical SWaP budgets. In contrast, low Earth orbit (LEO) systems benefit from much shorter propagation distances, reducing the link margin penalties introduced by longer wavelengths while still offering a significant improvement in the budget from reduced scattering and scintillation. As such, LEO represents the

most favorable orbital regime for near-term deployment of mid-IR wavelength conversion devices. The focus on LEO deployments therefore reflects the best trade-off between SWaP constraints and the performance gains afforded by longer-wavelength operation. This scaling continues as the link distance shrinks, and longer wavelengths seem especially promising for short-distance terrestrial links where the entire link propagates in turbulent atmospheric conditions, and the required increase in optical aperture size to balance the link budget is minimized.

As established in the prior section, nonlinear optics is a promising solution to providing MWIR light that can be modulated quickly and can lead to improved detectivity and bandwidth over direct MWIR semiconductor detectors. Despite this, it was also noted by the author that publications on nonlinear wavelength conversion devices for communication applications are somewhat infrequent. The concept of using nonlinear optics to shift the wavelength to the mid-infrared is not new, with publications specifically targeting communication applications in the MWIR appearing in the literature at least as early as 2005 [19]. There are some notable publications afterwards maintaining the focus on communication [7], [20], [21], [22]. However, the majority of upconversion publications are focused on single photon conversion or imaging applications, where modulation and detector bandwidth is not a significant factor [23], [24], [25], [26], [27]. This is likely due to the overall popularity of mid-infrared imaging and spectroscopy applications as a topic compared to optical free space communication at the time. There is a notable

uptick in upconversion publications in the late 2010's onwards, which is when there was a renewed push for advances in laser free space communication with the advent of commercial services like SpaceX's Starlink constellation, coupled with the potential cost-reduction of free space links for replacing expensive underground last-mile fiber infrastructure.

One of the most prolific groups innovating in the upconversion detector space includes authors A. Barh, J. Dam, C. Pedersen, and P. Tidemand-Lichtenberg [24], [28], [29]. Their upconversion detector published in Nature Photonics in 2012 held the record for MWIR upconversion quantum efficiency at 20% until quite recently, where a new record was set by Z. Ge et al. achieving a quantum efficiency of 37.9% using a 45W pump single pass scheme [30]. Of particular note is that most of these publications feature single pass systems utilizing bulk nonlinear crystals (usually PPLN thanks to its wide transparency region and high nonlinear coefficient). While the occasional publication uses a nonlinear waveguide to maximize conversion efficiency, as waveguides guarantee optimal overlap between the two input beams, this also limits the field-of-view of the detector. This is undesirable for many imaging and spectroscopy applications, hence the preference for bulk crystals. While simple to construct, single pass systems generally sacrifice size and overall efficiency versus intracavity devices. This is due to nonlinear processes being intensity dependent, and the intensity inside of a laser cavity is generally much higher for a given pump laser versus what can be achieved using the same laser in

a single pass set-up, due to the feedback effect provided by the addition of the resonator. A systematic study that applied modern focused gaussian beam theory and investigated the impact of various design variables on the performance of the upconversion detector was notably lacking in the literature, and so this thesis aims to fill that gap.

Compared to upconversion detectors, publications including a nonlinear optics-based transmitter element for generating MWIR light at high bandwidths are significantly harder to find. The most notable examples in the literature are from Q. Hao et al. demonstrating what may be the first complete single-pass MWIR transmitter and receiver system. Their experiment used a single-pass DFG transmitter with a modulated C-band source for encoding information onto the converted MWIR light. This MWIR signal was then coupled into a single pass SFG receiver to convert the light into a SWIR wavelength suitable for use with SiAPDs. To the best of the author's knowledge, this is the first publication featuring such a system, and it was characterized at a modulation speed of 200 Mbps. There were a series of follow-up publications from Y. Su et al (2018) and Gray et al. (2020) that featured gains in modulation bandwidth up to 10 Gbps and conversion efficiency up to 0.105%, but the single pass structure remained quite similar between these works [15], [31]. To the best of the author's knowledge, there are no notable intracavity DFG publications for communication applications, and so these single pass structures serve as the current state-of-the-art.

As a result of these gaps in literature, the goals of this thesis are as follows:

1. Create a proof-of-principle prototype demonstrating a novel intracavity DFG-based transmitter. The prototype will combine a diode-pumped solid state laser with an intracavity PPLN crystal to maintain a compact size. The cavity will provide, in theory, much higher input power for the circulating fundamental wavelength in the cavity. Then, a C-band source will be coupled into the nonlinear medium using an intracavity dichroic mirror. The two input lasers will then produce a MWIR signal that can be modulated up to the bandwidth limit of the C-band laser. To the best of the author's knowledge, such a device would be first-of-its-kind for optical communication.
2. Create a proof-of-principle prototype demonstrating a novel intracavity SFG-based receiver. The device structure is similar to the DFG structure, with the main differences being a different PPLN with a period engineered to optimize SFG, and that the input wavelengths will be 1064 nm and ~3.5 microns to produce ~814 nm light for use with SiAPDs. This structure is less novel than the transmitter, as an intracavity structure was reported by Dam et al. in 2012 while there is no comparable intracavity transmitter structure [24]. However, the device from Dam et al. is significantly larger than the potential intracavity design envisioned, reducing the number of mirrors needed from 7 to 2. Additionally, the design from Dam et al. was

designed for imaging applications, and so focused on maximizing field of view. It is hypothesized that gains in performance are possible, as the required field of view for communication applications is generally lower than that required for imaging. This would allow for the use of a longer nonlinear crystal, potentially increasing conversion efficiency.

3. Present a systematic study for both devices comparing their experimental performance with modern two-dimensional focused gaussian beam theory including overlap. The theory should also be able to model the gain medium and the cavity, accounting for both linear cavity losses (scattering, absorption, coating quality, etc.) and the nonlinear losses that arise due to the depletion of the circulating wave caused by three-wave mixing. The usage of modern theory in the previously reported publications is scattered at best. Additionally, the focus on imaging applications in upconverters means that much of the theory that is discussed uses the plane wave approximation due to the desire to maximize field of view. In a communication context, the FoV requirements are smaller, and so there is potential to use focused gaussian beams to maximize the conversion efficiency in bulk nonlinear materials. Coupling gaussian beam theory with a rate equation treatment to estimate circulating fundamental power inside the cavity should allow for accurate characterization of these intracavity devices. This thesis aims to provide this modern treatment and to discuss the different physical properties and design variables that can be used to

optimize intracavity wavelength converter performance.

1.3 Thesis Outline

Chapter 2 is the Theory chapter. This covers the physical and mathematical background to understand the devices developed in this thesis. The first section covers a brief review of the physical origin of second-order nonlinear optical phenomena and points out which phenomena are relevant to the following chapters. The second section covers the importance of maintaining phase matching in the nonlinear medium and its impact on overall device efficiency. Section three discusses how rate equations can be used to model continuous wave laser operation, which is important for understanding how the circulating fundamental power was calculated for simulation work. This section covers the author's contributions in terms of modelling the laser medium, mode overlap in the laser cavity and integrating linear and nonlinear losses into the rate equation approach. Finally, in section four, modelling the three-wave mixing processes difference frequency generation and sum frequency generation are discussed. There is also a discussion on the modifications necessary to model beam overlap inside of the nonlinear medium and the general trends to maximize device efficiency. The finished model presented in this thesis is a combination of the theory presented in sections three and four.

Chapter 3 covers the development of a theoretical model that combines rate equation cavity modelling with the nonlinear wave equations for second harmonic generation, a special case of sum frequency generation. By combining these two methods, the goal was to successfully show the importance of the nonlinear losses inside of the laser cavity induced by wavelength conversion of the fundamental into the second harmonic wave. The model is shown to have good agreement with experimental data, and also successfully predicts features of the temperature tuning curves that other models struggle to predict. This was the first test of the model combining rate equations with the nonlinear wave equation and is built upon in the following chapters, so it is important foundational work for the transmitter and receiver devices.

Chapter 4 discusses the implementation of the proof-of-principle prototype for the DFG transmitter, while also building on the model developed in Chapter 3. The goal of the prototype was to successfully demonstrate that a C-band signal laser could be combined in the nonlinear medium inside the cavity of a diode-pumped solid state 1064 nm laser to produce ~3.5 micron MWIR light. The prototype performed well, achieving a conversion efficiency of C-band signal to MWIR idler power of 10%. In this instance, conversion efficiency is defined as the internal conversion efficiency by taking the input signal power and dividing it by the output DFG power in Watts. The model from Chapter 3 was updated from a simplified plane wave cavity model to a more accurate spatially dependent model that factored

in the dependence of mode matching the diode pump laser to the cavity mode. The SHG coupled wave equations were also replaced with those for DFG. The experimental results matched the modelling in good agreement, and the overall black box efficiency of the device was higher than several comparable devices in the literature.

Chapter 5 covers the development of the proof-of-principle prototype for the SFG receiver and also represents the most developed and accurate modelling work by building upon the improvements in Chapter 4. The receiver prototype would take 3.5 micron light from the DFG transmitter and combine it inside the cavity of a 1064 nm diode-pumped solid state laser, similar to the transmitter design. Through sum frequency generation, this would convert the MWIR light into ~814 nm light, which was selected due to the availability of high performance commercial-off-the-shelf silicon photodetectors at this wavelength. The conversion efficiency from MWIR to 814 nm was good, achieving 36% internal conversion efficiency (input MWIR power divided by output 814 nm power). The modelling work was improved by adding the overlap integrals necessary to model beam overlap inside of the nonlinear medium. It was discovered that the beam overlap was not optimal and could be improved significantly, leading to large gains in overall device efficiency. This would later be applied to the DFG transmitter as well, increasing the efficiency from 10% to 15% for C-band to MWIR conversion efficiency. At this point, both transmitter and receiver were working in good agreement with theory and were

packaged for transport to the National Research Council for high-speed modulation experiments.

Chapter 6 is a concluding chapter, summarizing the work accomplished in the thesis and outlining potential future work that could be carried out for these devices.

The References section contains all of the references for Chapters 1 and 2 in Institute of Electrical and Electronics Engineers (IEEE) format.

The following published papers completed by the author appear in chapters 3, 4, and 5, respectively:

1. **L.Flannigan,** T. Kashak, and C.Q. Xu, "Study of fundamental wave depletion in intracavity second harmonic generation," Opt. Express 29, 6810-6823 (2021).
2. **L.Flannigan,** A. Atwi, T. Kashak, Daniel Poitras, and C.Q. Xu, "Compact Diode-Pumped Solid-State Laser with Intracavity Pump-Enhanced DFG Emitting at ~3.5 Microns," Photonics vol. 10 no. 10, 1164 (2023).
3. T. Kashak*, **L.Flannigan***, A. Atwi, Daniel Poitras, and C.Q. Xu, "Compact Intracavity Mid-Infrared Upconversion Detector – A Systematic Study," Opt. Continuum 3, 1660-1678 (2024). (* denotes shared first authorship due to equally significant contributions).

Chapter 2. Theory

2.1 Introduction to Nonlinear Optics

In order to understand the different nonlinear wavelength conversion techniques used throughout this thesis, it is helpful to understand how nonlinear optical phenomena are derived from Maxwell's equations and the fundamentals of linear optics. This derivation is standard and reported in many nonlinear optics textbooks. Two popular introductory books are those by Boyd and Powers [32], [33].

Nonlinear processes arise from the nonlinear terms in the polarization term for a given optical medium. In linear optics, the polarization of a medium $\widetilde{\mathrm{P}}$ is dependent on the magnitude of the incident electric field $\widetilde{\mathrm{E}}$ and the linear susceptibility of the medium $\chi^{(1)}$ which is a property of the material. To explain an important point about notation: in line with Boyd's derivation, a tilde (~) represents a quantity that varies rapidly with respect to time. If there is no tilde, then the quantity is constant, slowly varying, or a Fourier amplitude. Variables in **Bold** are vector quantities. The polarization can then be described using the formula:

$$\widetilde{\mathbf{P}}(\mathrm{t}) = \epsilon_0 \chi^{(1)} \widetilde{\mathbf{E}}(\mathrm{t}) \tag{2-1}$$

Where ϵ_0 is the permittivity of free space. We can see that the relationship between

polarization and the magnitude of the incident electric field is linear. However, this only holds for lower magnitudes of the electric field. Once the electric field magnitude inside the medium increases beyond a certain point (a criteria which lasers are well suited to meet), this linear relationship is no longer sufficient to describe the polarization. In order to adjust the model for higher intensities, it is common to break down the polarization as a power series of the electric field strength:

$$\widetilde{\mathbf{P}}(t) = \epsilon_0[\chi^{(1)}\tilde{\mathbf{E}}(t) + \chi^{(2)}\tilde{\mathbf{E}}(t)^2 + \cdots] \quad (2\text{-}2)$$

Here we can see an introduction of a new term $\chi^{(2)}$ which represents the second order nonlinear susceptibility of the medium. It is from this term that all second order nonlinear phenomena arise: rectification, second harmonic generation, and sum and difference frequency generation. There are additional terms omitted from the equation, with a third order susceptibility proportional to the cube of the electric field magnitude and so on. These third order effects are interesting and an active field of study, but as the contents of this thesis only cover second order phenomena, they are omitted for brevity. The units for the susceptibility terms are m/V for $\chi^{(2)}$, m^2/V^2 for $\chi^{(3)}$, and so on. This power series approach assumes that the general magnitude of these susceptibility terms tends to drop with increasing order, requiring higher and higher field intensities to become significant. This is the case for many materials and scenarios and is also why linear optics often omit the second

order and higher susceptibility terms. For many applications the electric field strength is nowhere near sufficient to cause observable nonlinear optical effects.

To quickly see the origin of nonlinear effects thanks to relation shown in Eq. (2-2) above, we can consider an incident field consisting of two linearly polarized monochromatic plane waves travelling in the z-direction. The total input field is represented as a superposition of the two fields with different frequencies:

$$\tilde{\mathbf{E}}(t) = \mathbf{E_1} e^{-i\omega_1 t} + \mathbf{E_2} e^{-i\omega_2 t} + c.c. \tag{2-3}$$

With the convention that frequency $\omega_1 > \omega_2$. ω_i represents the angular frequency, E_i represents the field amplitude, and c.c. represents the complex conjugate. If we substitute the field in Eq. (2-3) into Eq. (2-2) considering only the second order nonlinearity term, we get the following polarization response:

$$\tilde{\mathbf{P}}^{(2)}(t) = \epsilon_0 \chi^{(2)} \tilde{\mathbf{E}}(t) = \epsilon_0 \chi^{(2)} \left[\mathbf{E_1^2} e^{-2i\omega_i t} + \mathbf{E_2^2} e^{-2i\omega_2 t} + 2\mathbf{E_1 E_2} e^{-i(\omega_1+\omega_2)t} + 2\mathbf{E_1 E_2^*} e^{-i(\omega_1-\omega_2)t} + c.c. \right] + 2\epsilon_0 \chi^{(2)} [\mathbf{E_1 E_1^*} + \mathbf{E_2 E_2^*}] \tag{2-4}$$

The polarization response can be summarized as

$$\tilde{\mathbf{P}}^{(2)}(t) = \sum_n \mathbf{P}(\omega_n) e^{-i\omega_n t} \tag{2-5}$$

Where the sum is taken over all positive and negative frequencies ω_n. We can then look at the complex amplitudes of each of the frequency components in Eq. (2-4) or Eq. (2-5) and associate them with each of the second order nonlinear processes

that result from this nonlinear polarization:

$$\mathbf{P}(2\omega_1) = \epsilon_0\chi^{(2)}\mathbf{E_1^2} \text{ (SHG)}$$

$$\mathbf{P}(2\omega_2) = \epsilon_0\chi^{(2)}\mathbf{E_2^2} \text{ (SHG)}$$

$$\mathbf{P}(\omega_1 + \omega_2) = 2\epsilon_0\chi^{(2)}\mathbf{E_1}\mathbf{E_2} \text{ (SFG)} \tag{2-6}$$

$$\mathbf{P}(\omega_1 - \omega_2) = 2\epsilon_0\chi^{(2)}\mathbf{E_1}\mathbf{E_2^*} \text{ (DFG)}$$

$$\mathbf{P}(0) = 2\epsilon_0\chi^{(2)}[\mathbf{E_1}\mathbf{E_1^*} + \mathbf{E_2}\mathbf{E_2^*}] \text{ (OR)}$$

Each of the expressions in Eq. (2-6) represent a different second order nonlinear process: second harmonic generation (SHG), sum frequency generation (SFG), difference frequency generation (DFG), and optical rectification (OR). There are also equivalent expressions for all of the relations in Eq. (2-6) that represent the complex conjugate. And so we can see that two incident plane waves produce nonlinear polarizations at the sum and difference frequencies of the incident waves, as well as the second harmonics of both incident waves. Note that the derivation by Boyd drops the dependence on position which is reintroduced later. However, for completeness, a real field tends to travel in a direction denoted by z, with the complex form of the field written as:

$$\widetilde{\mathbf{E}}_\mathbf{i}(z,t) = \frac{1}{2}\mathbf{A_i}(z)e^{i(k_i z - \omega_i t)} + c.c. \tag{2-7}$$

Where $k_i = \omega_i n_i/c$ is the wave vector for field i, n_i is the refractive index for field i, c is the speed of light, and $A_i(z)$ is the complex field amplitude. Some authors (including Boyd) choose to drop the $\frac{1}{2}$ term and so it can be ambiguous which convention is being used. If including the $\frac{1}{2}$ term, this would modify Eq. (2-

3) and (2-5) as follows:

$$\tilde{\mathbf{E}}(t) = \frac{1}{2}(\mathbf{E_1'}e^{-i\omega_1 t} + \mathbf{E_2'}e^{-i\omega_2 t} + c.c.) \quad (2\text{-}8)$$

$$\tilde{\mathbf{P}}^{(2)}(t) = \frac{1}{2}\sum_n \mathbf{P}'(\omega_n)e^{-i\omega_n t} \quad (2\text{-}9)$$

And all of the amplitudes in (2-6) would be multiplied by a factor of $\frac{1}{2}$ as well. For the purposes of this thesis, we use the same convention as Boyd, and so the factor $1/2$ is not visibly present.

A more useful form of these nonlinearities comes from using Maxwell's equations to derive a nonlinear wave equation. This wave equation can then be used as a starting point for simulating nonlinear interactions in optical media, with suitable assumptions. Variables in **Bold** are vector quantities. Maxwell's equations in a dielectric are as follows:

$$\vec{\nabla} \cdot \tilde{\mathbf{D}} = \tilde{\rho}_f \quad (2\text{-}10)$$

$$\vec{\nabla} \times \tilde{\mathbf{E}} = -\frac{d\tilde{\mathbf{B}}}{dt} \quad (2\text{-}11)$$

$$\vec{\nabla} \cdot \tilde{\mathbf{B}} = 0 \quad (2\text{-}12)$$

$$\vec{\nabla} \times \tilde{\mathbf{H}} = \tilde{\mathbf{j}}_f - \frac{d\tilde{\mathbf{D}}}{dt} \quad (2\text{-}13)$$

Where $\tilde{\mathbf{E}}$ is the electric field, $\tilde{\mathbf{D}}$ is the electric displacement, $\tilde{\mathbf{H}}$ is the magnetic field, $\tilde{\mathbf{B}}$ is the magnetic induction, $\tilde{\rho}_f$ is the free charge density, and $\tilde{\mathbf{J}}_f$ is the free

current density. We assume the waves are travelling in mediums that contain no free charges, so $\widetilde{\rho}_f = 0$, and no free currents, so $\widetilde{\mathbf{J}}_\mathbf{f} = 0$. We also assume the material is nonmagnetic:

$$\widetilde{\mathbf{B}} = \mu_0 \widetilde{\mathbf{H}} \tag{2-14}$$

and we allow the material to be nonlinear so that this relation between $\vec{D}$ and $\vec{E}$ holds:

$$\widetilde{\mathbf{D}} = \epsilon_0 \widetilde{\mathbf{E}} + \widetilde{\mathbf{P}} \tag{2-15}$$

Where the polarization depends nonlinearly on the value of the electric field. Then we start deriving the optical wave equation by taking the curl of Eq. (2-11), change the order of the space and time derivatives on the right-hand side of the resulting equation, and use Eqs. (2-13) and (2-14) to replace the curl of $\widetilde{\mathbf{B}}$ with $\mu_0(\frac{d\widetilde{\mathbf{D}}}{dt})$, giving us the equation:

$$\vec{\nabla} \times \vec{\nabla} \times \widetilde{\mathbf{E}} + \mu_0 \left(\frac{d^2\widetilde{\mathbf{D}}}{dt^2}\right) = 0 \tag{2-16}$$

We can then substitute in Eq. (2-15) to eliminate $\vec{D}$, which gives the following equation:

$$\vec{\nabla} \times \vec{\nabla} \times \tilde{\mathbf{E}} + \frac{1}{c^2}\left(\frac{d^2\tilde{\mathbf{E}}}{dt^2}\right) = -\frac{1}{\epsilon_0 c^2}\frac{d^2\tilde{\mathbf{P}}}{dt^2} \tag{2-17}$$

With the substitution $\mu_0 = 1/\epsilon_0 c^2$. At this point Eq. (2-17) is the most general form of the nonlinear wave equation, although it can be simplified further. The first simplification is to use the vector calculus identity for the curl of the curl of the electric field:

$$\vec{\nabla} \times \vec{\nabla} \times \tilde{\mathbf{E}} = \vec{\nabla}\left(\vec{\nabla} \cdot \tilde{\mathbf{E}}\right) - \vec{\nabla}^2\tilde{\mathbf{E}} \tag{2-18}$$

The first term of Eq. (2-18) vanishes entirely as Eq. (2-10) implies. This gives us a new form of the nonlinear wave equation:

$$\vec{\nabla}^2\tilde{\mathbf{E}} - \frac{1}{c^2}\left(\frac{d^2\tilde{\mathbf{E}}}{dt^2}\right) = \frac{1}{\epsilon_0 c^2}\frac{d^2\tilde{\mathbf{P}}}{dt^2} \tag{2-19}$$

We can take this a step further by separating the polarization into its linear and nonlinear components $\tilde{\mathbf{P}} = \epsilon_0\chi^{(1)}\tilde{\mathbf{E}} + \tilde{\mathbf{P}}_{\mathrm{NL}}$, which we can substitute in Eq. (2-19):

$$\vec{\nabla}^2\tilde{\mathbf{E}} - \frac{1}{c^2}\left(\frac{d^2\tilde{\mathbf{E}}}{dt^2}\right) = \frac{1}{\epsilon_0 c^2}\frac{d^2(\epsilon_0\chi^{(1)}\tilde{\mathbf{E}}+\tilde{\mathbf{P}}_{\mathrm{NL}})}{dt^2} \tag{2-20}$$

We can simplify this by introducing the relative permittivity $\epsilon_r = 1 + \chi^{(1)}$ and rearranging the equation to a new form:

$$\vec{\nabla}^2\tilde{\mathbf{E}} - \frac{\epsilon_r}{c^2}\left(\frac{d^2\tilde{\mathbf{E}}}{dt^2}\right) = \frac{1}{\epsilon_0 c^2}\frac{d^2\tilde{\mathbf{P}}_{NL}}{dt^2} \tag{2-21}$$

This is the simplified general form of the nonlinear wave equation. It will be useful in Section 2.4 when deriving the coupled wave equations that govern three-wave mixing processes, which can be used to simulate both DFG and SFG. One last assumption we can make is that we are often only concerned with waves travelling in a single direction. If we choose this axis to be the z-direction and use the plane wave assumption, we can simplify Eq. (2-21) to a useful form for many problems:

$$\frac{d^2\tilde{\mathbf{E}}}{dz^2} - \frac{\epsilon_r}{c^2}\left(\frac{d^2\tilde{\mathbf{E}}}{dt^2}\right) = \frac{1}{\epsilon_0 c^2}\frac{d^2\tilde{\mathbf{P}}_{NL}}{dt^2} \tag{2-22}$$

2.2 Phase Matching

As one might expect, it is important to ensure that these wavelength conversion processes conserve both energy and momentum. For energy, this is straightforward to check. Let us consider sum frequency generation as an example. From the prior section, it is known from Eq. (2-6) that if we combine two waves with frequencies ω_1 and ω_2, we expect to produce a new frequency that is the sum of the two input frequencies $\omega_3 = \omega_1 + \omega_2$. Considering that the energy of a photon is directly tied to its frequency through the relation $E_{phot} = hv = hc/\lambda$, where $v_i = \omega_i/2\pi$ is the wave frequency,

h is Planck's constant, and λ is the wavelength, we can clearly see that energy is conserved so long as this condition is met. The same holds true for difference frequency generation $\omega_3 = \omega_2 - \omega_1$, and second harmonic generation is simply a special case of SFG where the two input waves have the same frequency.

In order to conserve momentum, we must ensure that the phase matching condition is met. In its most general form, the phase matching relation is often presented as:

$$\Delta k = k_p - k_s - k_i \tag{2-23}$$

Where $k_{p,s,i}$ is the wave vector amplitude from Eq. (2-4). The subscripts indicate the pump, signal, and idler wave, respectively. This is a historic naming convention, and the names are always assigned according to the energy of the input waves. The highest energy wave is the pump, the intermediate energy is the signal, and the lowest is the idler (pump > signal > idler by energy). This relation ensures that momentum is conserved if the difference between the pump, signal, and idler wave vector amplitudes is 0, $\text{i.e.}\, \Delta k = 0$. This causes a bit of a problem, however, as we can quickly note that the wave vector amplitude depends on the refractive index of the nonlinear medium. Given that the majority of materials are dispersive (the refractive index varies with wavelength), it is going to be difficult to find a combination of wavelengths that satisfy the requirement of $\Delta k = 0$.

There are two ways to work around this problem. The first is what is known as perfect phase matching. In perfect phase matching, a birefringent crystal is selected, and the incident angle of the input beams is varied by rotating the crystal through the desired axis. This allows fine control over the refractive index that each input wave "sees" in the crystal, and so there can be angular ranges where the phase matching condition is met. One restriction on this approach is the accuracy required for the rotation, which must be kept stable over time otherwise efficiency will suffer. The other more restrictive requirement for many practical applications is that any prospective wavelength conversion devices must find a suitable birefringent crystal. Depending on the desired input and output wavelengths, there may be no suitable material with the necessary birefringence in order to meet the perfect phase matching condition. Another related restriction is that the experiment is limited to using the crystal axis orientation that gives access to the necessary birefringence. Many nonlinear crystals have nonlinear coefficients that vary with crystal axis, and since the magnitude of the nonlinear coefficient is directly proportional to the overall efficiency of nonlinear processes, it would be desirable to use the axis with the largest nonlinearity which is not always possible.

This restriction in part led to the development of an alternative method of phase matching known as quasi-phase matching. The idea behind quasi-phase matching is to periodically invert the orientation of one of the crystal axes as a function of

position along one axis. In lithium niobate, this process can be achieved by ferroelectric domain engineering as lithium niobate is a ferroelectric material. This involves depositing electrical leads following the desired periodic structure and applying a strong local electric field (>20,000 V/mm) to permanently invert the domain in these regions. Different poling patterns can be used to custom-tailor the response of the crystal, but the most common choice is a simple 50:50 duty cycle square wave pattern. In the inverted regions of the crystal the PPLN's nonlinear coupling coefficient's sign is inverted as well. This approach allows the customization of the crystal period in order to cancel out any momentum mismatch for the targeted wavelengths. In practice, this can be represented by adding an additional term to the phase matching Eq. (2-23), the mathematical origin of which will be discussed shortly:

$$\Delta k = k_p - k_s - k_i - \frac{2\pi}{\Lambda} \tag{2-24}$$

Where Λ is the period of the domain inversion. This is illustrated in Figure 2-1, which is an illustrative model of the effect of domain inversion on phase matching.

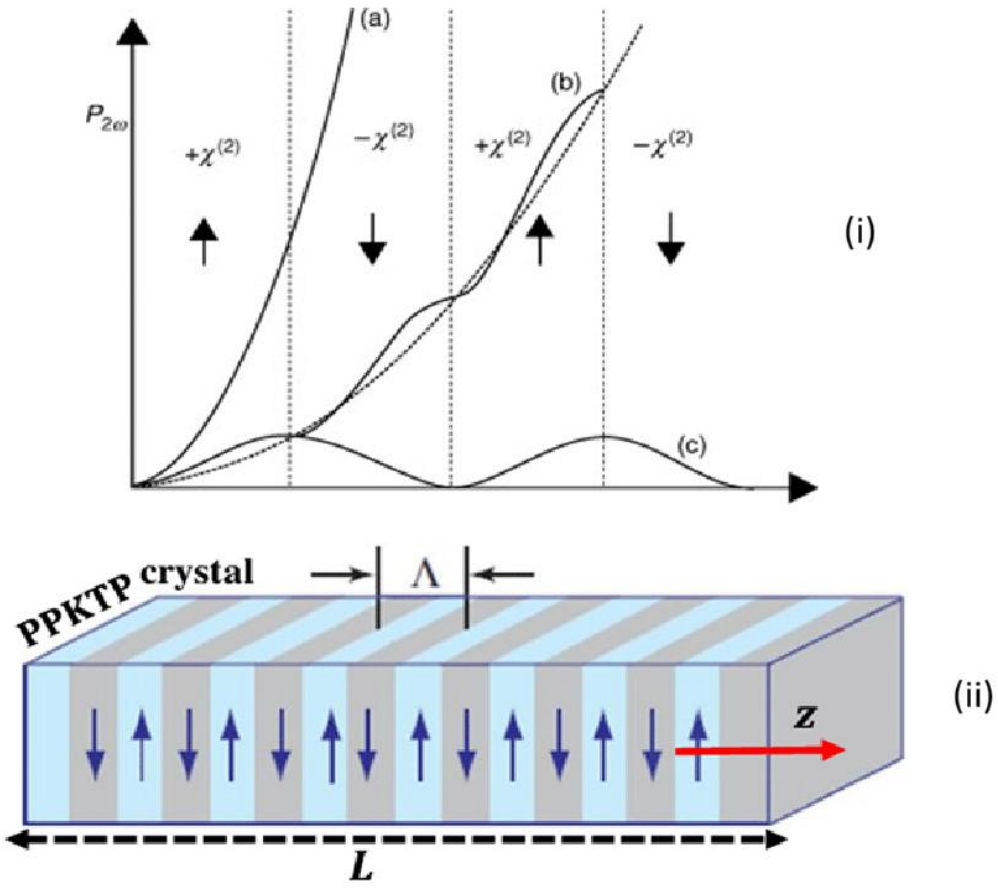

Figure 2-1 (i) A graph demonstrating the relative efficiency of different phase matching approaches. (a) represents perfect phase matching, (b) represents quasi-phase matching, and (c) represents the efficiency when there is a phase mismatch ($\Delta k \neq 0$) [34]. (ii) a diagram of a periodically poled crystal of length L demonstrating the poling period Λ and the direction of light propagation through the crystal (in this case the z-axis indicated by the red arrow).

In Fig (2-1) (i) the x-axis represents the propagation distance along one of the crystal axes (the z-axis indicated in Fig (2-1) (ii)), while the y-axis of the plot represents the hypothetical conversion efficiency for a second harmonic generation process. The line labelled (a) represents the conversion efficiency for perfect phase

matching ($\Delta k = 0$) using an equivalent birefringent crystal. There is a potential efficiency penalty to using quasi-phase matching if using the same crystal axis (and thus nonlinear coefficient) for perfect and quasi-phase matching which will be explained shortly. The line labelled (c) represents the case of wave vector mismatch ($\Delta k \neq 0$). In this case the conversion efficiency oscillates with distance travelled through the crystal, and the average conversion efficiency is very low. The line labelled (b) represents the case of quasi-phase matching where $\Delta k = 0$. We can see qualitatively that if $\Delta \mathrm{k} = 0$, the nonlinear polarization and the second harmonic wave reinforce each other constructively along the crystal, leading to growth of the second harmonic power. If $\Delta \mathrm{k} \neq 0$, the polarization and the second harmonic gradually shift out of phase, so the energy transfer isn't purely constructive; in fact, the average energy transfer is too low to be useful for practical applications. This may prompt the question for why the energy oscillates at all in the non-phase matched case. This is due to the propagation taking place inside of a dispersive medium and the mismatch of the fundamental and second harmonic k vectors. When the phase matching condition is not met, the second harmonic field at one point in the medium has contributions from different slices of the medium, each with a slightly different phase due to the phase mismatch. These contributions interfere with one another, leading to the result that the second harmonic power grows and reaches a maximum when the interference is mostly constructive, and then decreases back to zero when the interference is mostly destructive. Functionally, the power transfers back and forth between the fundamental and the

second harmonic, rather than steadily transferring from the fundamental to the second harmonic over the length of the crystal. These oscillations occur over a coherence length defined mathematically as:

$$L_{coh} = \frac{\pi}{\Delta k} \tag{2-25}$$

The dotted vertical lines in Fig (2-1) indicate integer multiples of the coherence length. Every two coherence lengths, the second harmonic energy has fully transferred back into the fundamental, and the process repeats. Thus, to maximize conversion energy in the quasi-phase matched case, the domain is inverted every coherence length. This way, the energy continues to transfer into the second harmonic instead of transferring back into the fundamental, leading to the increase in power seen in curve (b).

Mathematically, we can represent the poling pattern in Fig (2-1) (ii) with the function $d(z)$ that represents the spatial dependence of the nonlinear coefficient. In this case, it is a square wave function:

$$d(z) = d_{eff}\text{sign}\left[\cos\left(\frac{2\pi z}{\Lambda}\right)\right] \tag{2-26}$$

where d_{eff} is the effective nonlinear coefficient of the nonlinear crystal. It is common to express $d(z)$ using a Fourier series:

$$d(z) = d_{eff}\sum_{m=-\infty}^{\infty} G_m \exp\left(ik_m z\right) \tag{2-27}$$

Where $k_m = 2\pi m/\Lambda$ is the magnitude of the grating vector associated with the mth Fourier component of $d(z)$. Boyd shows that for square wave modulation in the nonlinear crystal given by Eq. (2-27), the Fourier coefficients G_m are given by:

$$G_m = \left(\frac{2}{m\pi}\right) \sin\left(\frac{m\pi}{2}\right) \tag{2-28}$$

And so for 1st order phase matching where m=1, the fundamental Fourier coefficient is given by $G_1 = 2/\pi$. Thus, we have the nonlinear coefficient for Fourier order m $d_m = d_{eff} G_m$ and the wave vector mismatch for order m is given by $\Delta k_m = k_1 + k_2 - k_3 + k_m$. We can see from Eq. (2-28) that higher orders of m will generally lead to a decrease in the value of the nonlinear coefficient, and so most practical devices use the first-order interaction for quasi-phase matching, providing the following phase matching and nonlinear coefficient relations for square wave modulated nonlinear crystals:

$$\Delta k_m = k_1 + k_2 - k_3 - \frac{2\pi}{\Lambda}, \qquad d_m = \left(\frac{2}{\pi}\right) d_{eff} \tag{2-29}$$

There are a couple notable advantages for quasi phase matching over perfect phase matching. One advantage is that quasi-phase matching allows the use of the highest nonlinear coefficient. We can see from Eq. (2-29) that for square wave patterned nonlinear crystals (common commercially), the nonlinear coefficient is reduced by a factor of $\frac{2}{\pi}$ when using quasi-phase matching compared to perfect phase matching [32]. However, this penalty is often still preferable to using perfect phase matching for many applications. To clarify, lithium niobate's highest nonlinear

coefficient is 25 pm/V, while the axis often used for birefringent phase matching has a coefficient of 4.4 pm/V [35]. Even with the reduction factor, the effective nonlinear coefficient is $\mathrm{d_{eff}} = \frac{2}{\pi}\ (25\ \mathrm{pm/V}) = 14\ \mathrm{pm/V}$, which is much higher. Another advantage is the additional phase matching term introduced by the poling process representing the grating vector as seen in Eq. (2-29). This additional term allows for many combinations of pump, signal, and idler wavelength combinations to be used so long as the required grating period for the nonlinear crystal can be fabricated and the nonlinear crystal is transparent to the required wavelengths. This can be combined with the temperature dependence for the refractive indices of the nonlinear material to allow for fine control of the phase matching by attaching the nonlinear medium to a thermoelectric cooler or similar temperature control device. The temperature dependence of the refractive index can be modelled using the Sellmeier equation for magnesium doped PPLN:

$$n_e^{\,2} = a_1 + b_1 f + \frac{a_2 + b_2 f}{(\lambda^2 - (a_3 + b_3 f))^2} + \frac{a_4 + b_4 f}{\lambda^2 - a_5^{\,2}} - a_6 \lambda^2 \qquad (2\text{-}30)$$

where a1, a2, … a6 and b1, … b4 are the Sellmeier coefficients provided in Gayer et al. and the temperature dependent parameter f is defined as $\mathrm{f} = (\mathrm{T} - 24.5°\mathrm{C})(\mathrm{T} + 570.82)$ where T is the temperature of the crystal in °C [36].

All of this combined means that quasi-phase matching is often used due to its flexibility, less restrictive axis requirements, and the availability of high-quality commercial-off-the-shelf periodically poled crystals. This thesis makes frequent

use of periodically poled lithium niobate (PPLN) as the Xu group has access to the necessary equipment to fabricate and pole custom lithium niobate for a variety of applications.

2.3 Rate Equations for Continuous Wave Lasers

In order to accurately simulate an intracavity frequency converter, you must be able to simulate both the input wave circulating within the resonator at steady state, and use this wave as an input for simulating the nonlinear three-wave mixing process. The latter is covered in Section 2.4; this section will focus on covering the rate equation used throughout this thesis. The model that was selected is derived by W.P. Risk for longitudinally pumped solid-state lasers, which matches the Nd:YVO_4 end-pumped solid state laser used to produce the 1064 nm pump beam through all of the experiments in this thesis [37]. The derivation is detailed in the cited manuscript, so this section will focus on the final equations and the computational steps to solve them.

After setting up the relevant set of coupled wave equations for a four-level energy system relevant to lasers like Nd:YVO_4, Risk makes one important change to modify this model from a plane wave rate equation model to a spatially dependent rate equation model that can take into account the gaussian mode overlap between the diode pump laser and the laser cavity. This is done by assuming the pump beam

is a circular gaussian, given in cylindrical coordinates by:

$$r_p(r,z) = \frac{2\alpha}{\eta_a \pi w_p^2} \exp\left(-\frac{2r^2}{w_p^2}\right) \exp(-\alpha z) \quad (2\text{-}31)$$

Where z is the propagation direction, r represents the transverse coordinates, α is the absorption coefficient of the gain medium at the wavelength of the pump diode, η_a is the fraction of the incident pump power absorbed by the gain medium according to length, and w_p is the waist of the pump laser. This allows for optimization of the pump diode relative to the size of the cavity mode, which will increase the overall efficiency of the intracavity laser. A similar approach is used to estimate the total number of photons in the cavity, with an assumed circularly symmetric cylindrical distribution of photons throughout the cavity. After deriving the photon density population inversion density rate equations, the gain of the laser can be calculated and combined with the intensity profile of the laser beam as it propagates through the gain medium to estimate the intracavity power of the laser. The final form of the equation is given below:

$$F = \frac{1+\frac{B}{fS}\ln(1+fS)}{f\int_0^{\infty} \frac{\exp[-(a^2+1)x]}{1+fS\exp(-a^2x)}} \quad (2\text{-}32)$$

This equation can be solved to determine the threshold of the laser (S=0) and the slope efficiency of the laser above threshold (S>0). F represents the normalized

pump power from the diode pump laser, a is the ratio of the pump diode beam waist to the laser cavity mode waist, f is the sum of the Boltzmann factors of the lower and upper laser levels in the gain medium, $x = \frac{2r^2}{w_p^2}$, and S is the normalized intracavity power. Term B represents the ratio of reabsorption loss in the laser crystal to the losses in the cavity and is given by:

$$B = \frac{2N_1^0 \sigma l}{(L+T)} \tag{2-33}$$

Where l is the gain medium crystal length, L is the round-trip cavity loss, T is the output transmission coefficient of the output coupling mirror, σ is the gain cross section, and N_1^0 is the population of the lower laser level. The round trip cavity loss includes both the linear losses from non-ideal coatings, scattering, and absorption, as well as the nonlinear losses from converting the circulating cavity power into a different wavelength. The nonlinear loss can be calculated by accounting for the number of photons converted from the pump wavelength to the idler wavelength as $\alpha_{NL} = \frac{\lambda_i}{\lambda_p}\frac{P_i}{P_p}$ where P_i and P_p represents the total converted idler power and the total circulating pump power in the cavity, respectively. Thus the total loss in the cavity would be $L = \alpha_{cav} + \alpha_{abs} + \alpha_{scat} + \alpha_{NL}$. F can be calculated using the relation:

$$F = \frac{4P_p \tau \sigma \eta_a}{\pi h v_p w_L^2 (L+T)} \tag{2-34}$$

Where P_p is the pump diode power in watts, τ is the upper-level lifetime of the gain medium, h is Planck's constant, v_p is the frequency of the pump laser, and w_L is the waist of the cavity mode.

In order to use these formulas to predict the circulating cavity power, we start by numerically solving Eq. (2-32) for the variable S. This is done by substituting in $x, B, \text{and } F$ using the known experimental values for the gain medium and laser experimental setup. Then, a modified Powell's method root finding algorithm can be used by leveraging SciPy's (SciPy is a scientific python package that implements many common scientific algorithms numerically) implementation of the hybrd and hybrj routines in MINPACK (a Fortran library). This approach allows for the value of S to be found for all values of F representing the pump power. The slope efficiency can be found by taking the gradient of the found F and S values representing dS/dF. Then, the normalized slope efficiency dS/dF can be used to calculate the real external slope efficiency via the relation:

$$\frac{dP_{out}}{dP_p} = \frac{T}{L+T}\frac{v_L}{v_p}\eta_a\frac{dS}{dF} \tag{2-35}$$

With the external slope efficiency solved, the final step is to calculate the threshold power using the formula:

$$P_{p,th} = \frac{\pi h v_p (w_L^2 + w_p^2)(L + T + 2N_1^0 l)}{4\sigma\tau\eta_a f} \quad (2\text{-}36)$$

And the normalized pump power threshold:

$$F_{th} = \frac{(1+a^2)(1+B)}{f} \quad (2\text{-}37)$$

Which can be used to convert the normalized pump powers back into real pump powers via $P_p = \left(\frac{P_{p,th}}{F_{th}}\right) F$, and the slope efficiency is constant past the threshold so it can be used to calculate the external laser power past threshold. Then, since the external laser power is known at all calculated pump powers, we can easily work backwards and figure out the circulating cavity power at steady state from the transmission coefficient T of the output coupling mirror. This circulating steady state cavity power can then be used as an input to the simulation work in Section 2.4 to estimate the nonlinear three wave mixing power produced as a result.

2.4 Cavity Considerations for the Presented Device

The initial cavity architecture employed in this work is a hemispherical resonator consisting of a high-reflectivity (HR) coating deposited directly onto the Nd:YVO_4 gain medium, paired with a 150 mm radius-of-curvature output coupler to form the primary cavity. A dichroic mirror is included within the cavity to enable coupling of the modulated input field, which subsequently mixes with the intracavity

fundamental beam in a periodically poled lithium niobate (PPLN) crystal. The hemispherical configuration was chosen for its practicality: it is straightforward to fabricate and align, leverages significant prior experience within our research group in diode-pumped solid-state laser development, and offers a relatively compact footprint suitable for integration into a portable system. Fig 2-2 details a conceptual schematic diagram as well as the packaged prototype for this design as implemented in the lab.

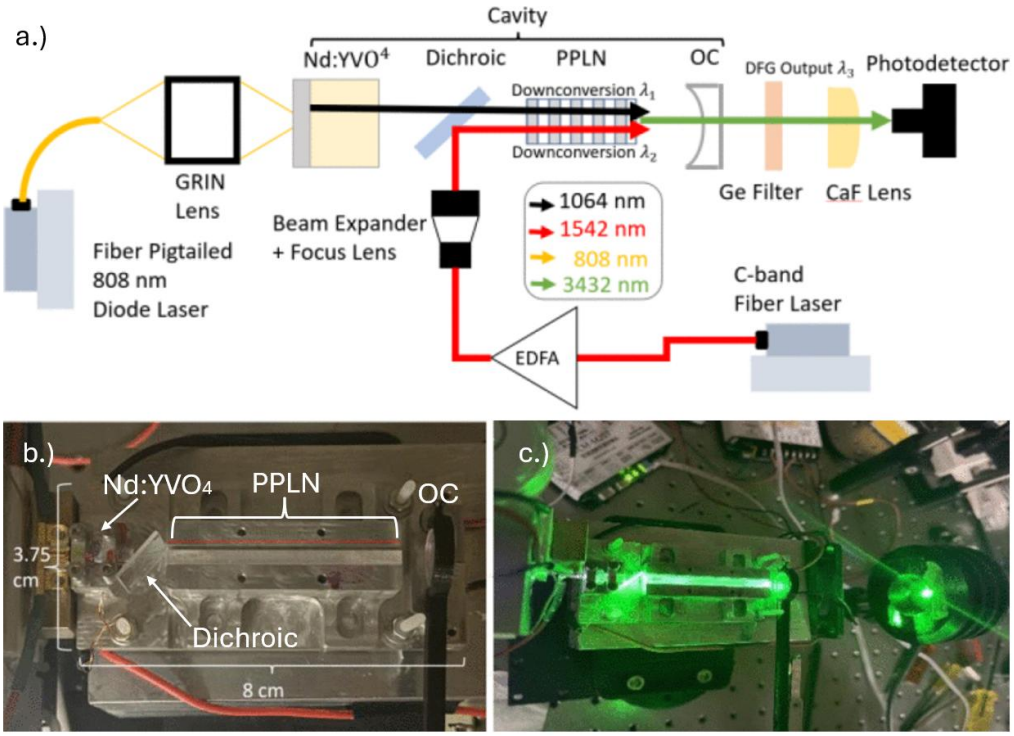

Figure 2-2 A diagram detailing the cavity design of the transmitter and receiver prototype presented in this thesis. a.) a conceptual diagram of the intracavity frequency converter for the DFG-based transmitter. The modulated C-band light is coupled into the PPLN via the dichroic mirror, while the Nd:YVO_4 provides the 1064 nm light. The cavity is a hemispherical design made up of the HR coating on the Nd:YVO_4 and the curved output coupler. b.) A picture of the packaged prototype of

the intracavity transmitter with the overall dimensions and important components labelled. c.) an image of the transmitter operating at full power, with the leaking green light a result of parasitic second harmonic generation of the 1064 nm fundamental light in the PPLN [38].

The cavity was analyzed using the reZonator software package, which implements ABCD matrices in Python for cavity analysis [39]. ABCD matrices are covered in depth in the textbook Lasers by Siegman, and a more detailed treatment and derivation of the method can be found there [40]. Despite the aforementioned advantages, numerical modeling revealed a key limitation of the hemispherical cavity. Specifically, the fundamental 1064 nm mode is restricted to a relatively large beam waist within the PPLN crystal, around 110 microns as shown in Fig 2-3. Using the Boyd-Kleinman focus factor, this provides a factor around ~0.3, which is significantly underfocused. This underfocusing condition leads to reduced spatial overlap with the modulated input beam and consequently limits the nonlinear conversion efficiency. The compactness and simplicity of the hemispherical cavity therefore come at the expense of optimal focusing conditions in the nonlinear medium. This cavity modelling was used to inform the nonlinear modelling in Section 2.5, and this modelling agreed well with the experimental results.

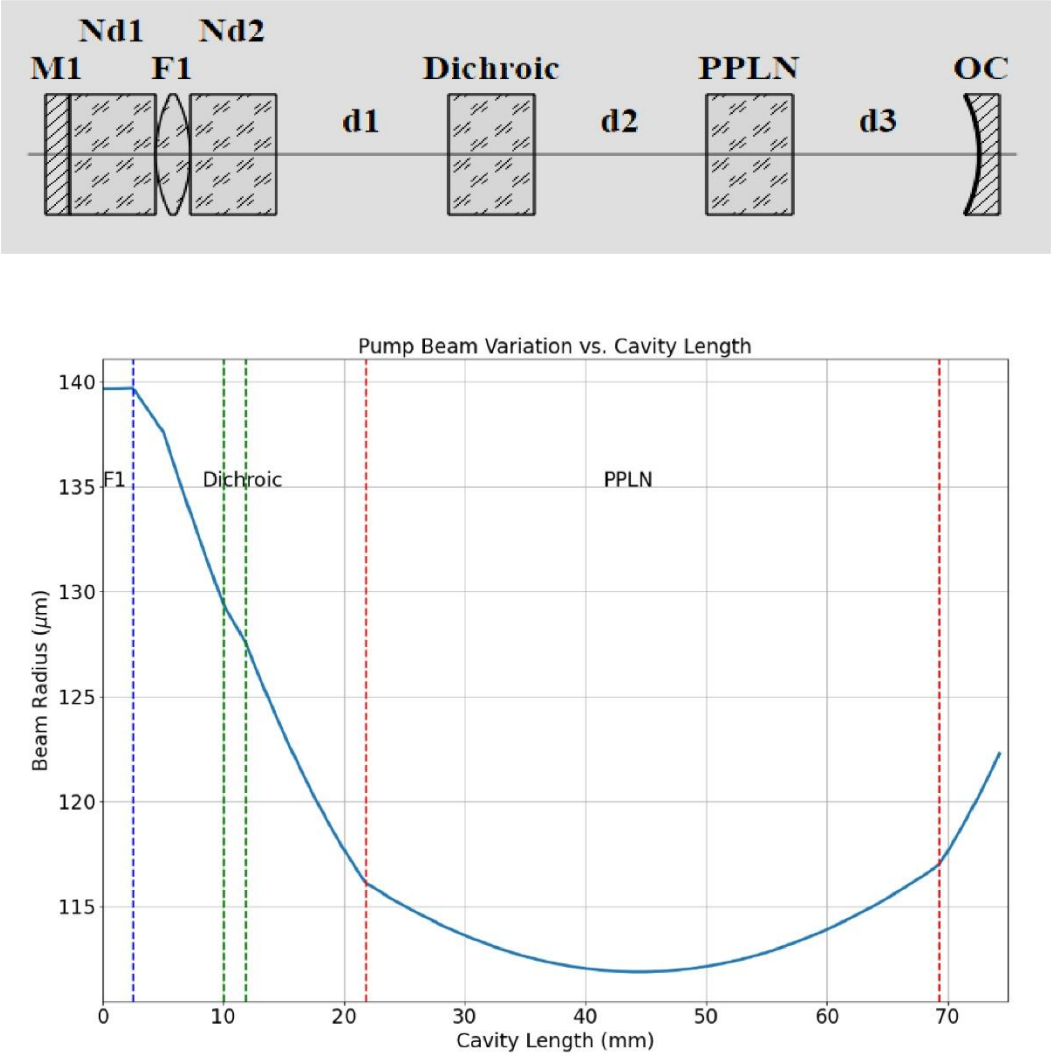

Figure 2-3 A block diagram of the cavity as modelled in reZonator. M1 is the planar HR coating, the Nd medium is split into two halves of equal length with a thin lens F1 in the middle to model thermal lensing. The distances d1-d3 were measured experimentally as well. The plot on the bottom shows the steady state beam waist of the 1064 nm light inside the cavity as a function of distance from mirror M1. The vertical dashed blue line indicates the location of the thermal lens, the two vertical green dashed lines represent the input and output facets of the dichroic mirror, and the vertical dashed red lines represent the input and output facets of the PPLN crystal.

To address this drawback, alternative cavity geometries were considered that

provide tighter mode confinement and well-defined intracavity foci away from the mirrors. Two promising candidates are the Z-fold cavity and the bow-tie cavity. Both geometries incorporate additional mirrors to fold the optical path, enabling the placement of the nonlinear crystal at a natural beam waist formed in free space between the curved mirrors. This allows for improved control of the mode size within the PPLN and facilitates stronger beam overlap with the injected field, thereby enhancing the efficiency of the frequency conversion process. Fig 2-4 below illustrates all three cavity designs, highlighting how the waist position is in a more beneficial location versus the hemispherical cavity.

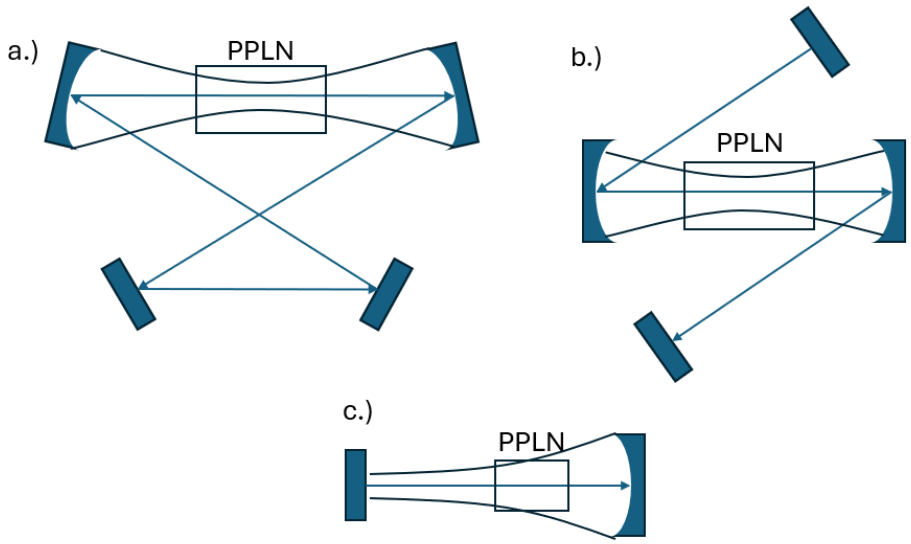

Figure 2-4 A diagram highlighting the three cavity designs being discussed. a.) represents a bowtie cavity, where the waist is well defined in the center of the two curved mirrors, making it an obvious spot to place the nonlinear medium for beam overlap tailoring. b.) demonstrates a typical z-fold cavity, with the similar advantage of having a well-defined and easy to modify waist in the center of the two curved mirrors. c.) demonstrates a simplified version of the hemispherical cavity currently in use, which is much simpler to fabricate, but the waist is located at the plane mirror and so it is not straightforward to tailor the beam waist inside of the PPLN, which is further exacerbated by the Nd:YVO4 gain medium in the prototype preventing the PPLN from being placed closer to the waist.

The Z-fold design offers the advantage of maintaining linear propagation through

the gain medium while introducing a stable focus that can be precisely positioned within the nonlinear crystal. Meanwhile, the bow-tie cavity provides even greater flexibility in beam waist tailoring, along with inherent spatial separation of forward and backward propagating beams, which may reduce undesired feedback and parasitic effects. Although these designs require more complex alignment and slightly increase the physical footprint of the system, they hold clear advantages in optimizing the focusing conditions within the nonlinear medium. Using such cavity designs for wavelength converters is not a novel idea, and waist sizes as low as 20 microns at 1064 nm have been reported for SFG frequency converters in the literature [41], [42]. This added flexibility in tailoring the 1064 nm beam waist means that the beam overlap can be fully optimized for both the transmitter and receiver designs. As such, both architectures present viable pathways to overcome the focusing limitations inherent to the hemispherical cavity, enabling higher conversion efficiencies in compact wavelength converter systems. Of course, this does come with the potential trade-off of higher alignment sensitivity, higher manufacturing cost, and a potential increase in cavity size, so a cost-benefit analysis for the intended application would help decide whether the increase in efficiency is worth the potential drawbacks.

2.5 Simulation Methods for Three-Wave Mixing

2.5.1 Plane Wave Approach

In order to simulate three-wave mixing processes (SFG and DFG), it is necessary

to use the nonlinear wave Eq. (2-22) derived previously as a starting point. We must also make some assumptions about the configuration of the nonlinear medium and the waves entering the medium. A sum frequency configuration is illustrated in Figure 2-5.

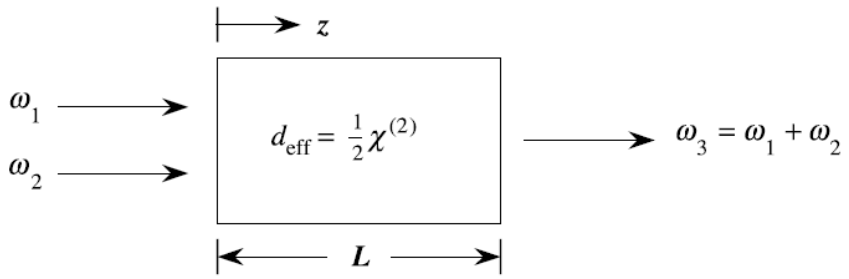

Figure 2-5 A high-level diagram depicting sum frequency generation. Two input waves ω_1 and ω_2 travelling in the z-direction are combined in a second order nonlinear medium of length L to produce a third wave ω_3 whose frequency is the sum of the two input waves.

We assume that there were two input waves ω_1 and ω_2 that propagate onto the input facet of the nonlinear medium at normal incidence. These waves will combine in the medium to produce an output wave $\omega_3 = \omega_1 + \omega_2$. We assume the solution to this equation will be a plane wave at the frequency ω_3 propagating in the positive z direction:

$$\widetilde{E}_3(z,t) = A_3(z)e^{i(k_3 z - \omega_3 t)} + c.c. \tag{2-38}$$

Where $A_3(z)$ is the complex amplitude of the wave, which is assumed to be a

slowly varying function of z, and c.c. indicates the complex conjugate. Note that since we assume the electric field is linearly polarized, it and the following equations are re-cast as scalar equations. We also define a nonlinear source term for the wave to substitute into the right hand side of Eq. (2-22) derived from the nonlinear susceptibility [33]:

$$\widetilde{P}_3(z,t) = P_3 e^{-i\omega_3 t} + c.c. \tag{2-39}$$

Where $P_3 = 4\epsilon_0 d_{eff} E_1 E_2$ is the amplitude of the nonlinear polarization and d_{eff} is the effective nonlinear coefficient (~14 pm/V for PPLN). We then write the wave equations for the two input waves (i=1, 2):

$$\widetilde{E}_i(z,t) = E_i e^{-i\omega_i t} + c.c. \text{ where } E_i = A_i e^{ik_i z} \tag{2-40}$$

We can then re-write the amplitude of the nonlinear polarization term as:

$$P_3 = 4\epsilon_0 d_{eff} A_1 A_2 e^{i(k_1+k_2)z} \tag{2-41}$$

We can then substitute Eqs. (2-37), (2-38), and (2-40) into Eq. (2-21) to obtain:

$$\left[\frac{d^2A_3}{dz^2} + 2ik_3\frac{dA_3}{dz} - k_3^2 A_3 + \left(\frac{\epsilon_r(\omega_3)\omega_3^2 A_3}{c^2}\right)\right] e^{i(k_3 z - \omega_3 t)} + c.c.$$

$$= \left(-\frac{4d_{eff}\omega_3^2}{c^2}\right) A_1 A_2 e^{i[(k_1+k_2)z-\omega_3 t]} + c.c. \quad (2\text{-}42)$$

We can observe that the third and fourth terms on the left hand side cancel since $k_3^2 = \epsilon_r(\omega_3)\omega_3^2/c^2$, we can also cancel the factor $\exp(-i\omega_3 t)$, and we can drop the complex conjugate terms from both sides. This gives the simplified equation:

$$\frac{d^2A_3}{dz^2} + 2ik_3\frac{dA_3}{dz} = \frac{-4d_{eff}\omega_3^2}{c^2} A_1 A_2 e^{i(k_1+k_2-k_3)z} \quad (2\text{-}43)$$

We can further simplify the equation using an assumption known as the slowly varying wave approximation. So long as the change in the amplitude A_3 over a distance on the order of the optical wavelength is much smaller than one, the second derivate of A_3 with respect to z is often negligible compared to the first derivative term. The slowly varying amplitude approximation is expressed mathematically as:

$$\left|\frac{d^2A_3}{dz^2}\right| \ll \left|k_3\frac{dA_3}{dz}\right| \quad (2\text{-}44)$$

This assumption generally holds for continuous wave operation and was used for the simulation work in this thesis. This assumption tends to break down for pulsed input waves, and so the full Eq. (2-43) must be solved instead. With this approximation, Eq. (2-43) can be simplified to:

$$\frac{dA_3}{dz} = \frac{2id_{eff}\omega_3}{n_3 c} A_1 A_2 e^{i\Delta kz} \tag{2-45}$$

where n_3 is the refractive index for wave 3, and we have simplified the wave field amplitudes by introducing the phase matching term for SFG from Section 2.2:

$$\Delta k = k_1 + k_2 - k_3 \tag{2-46}$$

Eq. (2-45) is known as a coupled amplitude equation, which is due to the dependence of the resulting sum frequency amplitude on the amplitude of the two input waves. This form of the equation assumes no spatial mismatch, but spatial coupling is an important consideration that will be expanded upon in Section 2.5.2. If we repeat the derivation above for the other two waves, we will end up with two more coupled amplitude equations fully describing sum frequency generation in the plane wave limit:

$$\frac{dA_1}{dz} = \frac{2id_{eff}\omega_1}{n_1 c} A_3 A_2^* e^{-i\Delta kz} \tag{2-47}$$

$$\frac{dA_2}{dz} = \frac{2id_{eff}\omega_2}{n_2 c} A_3 A_1^* e^{-i\Delta kz} \tag{2-48}$$

Where the * denotes the complex conjugate. This form also assumes the medium is lossless, that the two input fields are undepleted (no significant change in their

magnitude). and that the nonlinear coefficient is the same for each wavelength. The latter is usually a safe assumption to make for PPLN, as it features a wide transparency region with low total losses due to absorption and scattering.

The validity of the depletion assumption will depend on the application at hand. For upconversion devices like the one presented in this thesis, the power of the idler light to be converted is typically several orders of magnitude lower than the circulating pump power in the cavity. Using the prior notation, we assume one of the input fields (say the circulating cavity light at frequency ω_2) is strong and will not deplete. The other input field (at frequency ω_1) is weak. As a result, the weak idler beam is generally depleted significantly in order to produce the sum frequency / upconverted frequency ω_3, and this assumption of strong input fields is no longer valid.

We can start with the coupled wave equations above and make some modifications to account for the input field at frequency ω_1 being weak. Since we've assumed the field at frequency ω_2 is strong, we can assume that the amplitude A_2 is effectively constant. This means we are left with two coupled wave equations for the weaker fields:

$$\frac{dA_1}{dz} = K_1 A_3 e^{-i\Delta kz} \tag{2-49}$$

$$\frac{dA_3}{dz} = K_3 A_1 e^{+i\Delta kz} \tag{2-50}$$

Where the coefficients K_1 and K_3 are used to tidy up the equations:

$$K_1 = \frac{2i\omega_1^2 d_{eff}}{k_1 c^2} A_2^*, \qquad K_3 = \frac{2i\omega_3^2 d_{eff}}{k_3 c^2} A_2 \tag{2-51}$$

And $\Delta k = k_1 + k_2 - k_3$. The simplest practical solution can be found by assuming that perfect phase matching has been attained ($\Delta k = 0$), taking the derivative of Eq. (2-49) with respect to z, and using Eq. (2-50) to eliminate the derivative dA_3/dz from this new equation to get it into a form that only depends on A_1:

$$\frac{d^2 A_1}{dz^2} = -\kappa^2 A_1 \tag{2-52}$$

Where a coupling coefficient has been defined to simplify the equation:

$$\kappa^2 = -K_1 K_3 = \frac{4\omega_1^2 \omega_3^2 d_{eff}^2 |A_2|^2}{k_1 k_3 c^4} \tag{2-53}$$

Eq. (2-52) has a general solution of the form:

$$A_1(z) = B\cos(\kappa z) + C\sin(\kappa z) \tag{2-54}$$

We can then rearrange Eq. (2-49) such that $A_3(z) = \left(\frac{dA_1}{dz}\right) K_1$ so that:

$$A_3(z) = -\frac{B\kappa}{K_1}\sin(\kappa z) + \frac{C\kappa}{K_1}\cos(\kappa z) \tag{2-55}$$

To find the solution, we apply boundary conditions that assume there is no field for ω_3 at the input of the nonlinear crystal (which is common) so that $A_3(0) = 0$, and $A_1(0)$ is known experimentally. The first boundary condition combined with Eq. (2-54) gives us $C = 0$, and Eq. (2-54) shows that $B = A_1(0)$. Thus the solutions take the forms:

$$A_1(z) = A_1(0)\cos(\kappa z) \tag{2-56}$$

$$A_3(z) = -A_1(0)\frac{\kappa}{K_1}\sin(\kappa z) \tag{2-57}$$

The physical interpretation of these solutions is that the input field amplitude A_1 will deplete and the amplitude of the upconverted wave A_3 will increase until the input field is fully converted from frequency ω_1 to $\omega_3 = \omega_1 + \omega_2$ (i.e. $A_1 = 0$ and A_3 is maximized). If this occurs before the end facet of the nonlinear crystal, the periodic nature of these solutions means that back conversion will occur, and the upconverted field at ω_3 will begin to convert back into the input field at ω_1. In practice, the conversion efficiency in bulk PPLN upconversion devices is low enough that you do not see full conversion of the weak input wave into the upconverted frequency even with long crystal lengths, and so back conversion does not occur. This would be a greater concern in waveguide devices, where the conversion efficiency as a function of device length is much higher due to the improved confinement of the three waves involved in the upconversion process.

A similar process can be used for difference frequency generation. With a slight change in notation, DFG is described by two incident waves with frequencies ω_3 and ω_1 incident to a nonlinear medium, producing a new wave with frequency $\omega_2 = \omega_3 - \omega_1$. This process is represented in Figure 2-6.

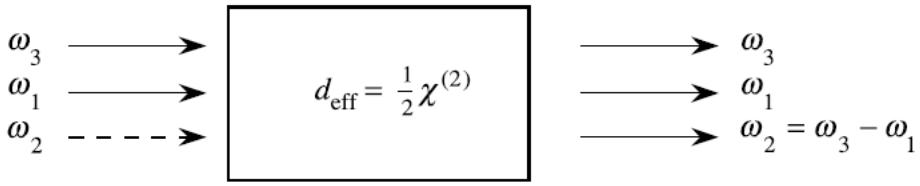

Figure 2-6 A high level block diagram of difference frequency generation. The dashed line for ω_2 indicates that there is often no input wave for frequency ω_2.

It is often assumed that the input wave with frequency ω_3 has a large enough magnitude that it is effectively constant (the wave is undepleted), which allows us to treat A_3 as constant. This means that we end up with two coupled wave equations for DFG, derived using a similar process as for SFG:

$$\frac{dA_1}{dz} = \frac{2id_{eff}\omega_1^2}{k_1c^2} A_3 A_2^* e^{-i\Delta kz} \tag{2-58}$$

$$\frac{dA_2}{dz} = \frac{2id_{eff}\omega_2^2}{k_2c^2} A_3 A_1^* e^{-i\Delta kz} \tag{2-59}$$

Where $\Delta k = k_3 - k_1 - k_2$ is the new phase matching condition for DFG. These equations for DFG and SFG form sets of coupled ordinary differential equations. They can be solved using numerical integrators like a 4th-order Runge-Kutta algorithm. This is a common package in scientific computing packages like SciPy for Python or the ode45 function in Matlab [43], [44]. As the powers of the two input waves are often known or planned experimentally, and the SFG or DFG output wave has a starting magnitude of zero at the input facet, all of the boundary

conditions necessary to solve the coupled wave equations are known and solving the equations is straightforward.

2.5.2 Accounting for Beam Overlap

The method in Section 2.4.1 was derived for plane waves. However, in practice, real lasers are more accurately modelled using Gaussian beams. The name refers to the intensity profile of the beam, which takes the form of a gaussian distribution. A cylindrically symmetric Gaussian beam can be modelled using the equation:

$$\mathrm{A}(\mathrm{r},\mathrm{z}) = \mathrm{A}_0(\mathrm{z})\mathrm{e}^{-\mathrm{r}^2/\mathrm{w}^2(\mathrm{z})} \tag{2-60}$$

Where $\mathrm{A}_0(\mathrm{z})$ is the complex field amplitude on axis, $\mathrm{w}(\mathrm{z})$ is the field's $1/\mathrm{e}$ radius, and r represents the transverse dimension. This is an important problem to resolve, as the plane wave assumption used prior assumes perfect spatial overlap between the two input beams for three-wave mixing. In reality, there are numerous physical reasons why the overlap may not be perfect: one or both of the input beams could be misaligned relative to the optical axis, the usage of different wavelengths means that different focusing conditions will lead to potential mismatch between the two beams, and the focus for each beam may be in different locations within the nonlinear medium. All of these experimental errors have the potential to decrease the overall device efficiency, so it is vital to be able to model the beam overlap to ensure that the final device is close to optimum overlap.

Despite the importance of beam overlap and the Gaussian nature of experimental laser beams, the plane wave formulas derived above are still useful under certain conditions. Gaussian beams have a quantity known as the Rayleigh length (or Rayleigh range) z_R. It is defined as the distance from the beam waist where the radius of the gaussian beam increases by a factor of $\sqrt{2}$. The curvature of the wavefront of a gaussian beam is planar at the focus and can be assumed to change slowly enough that we can assume it remains planar until the Rayleigh range. That is to say, if the Gaussian beam's focus is located at the center of a nonlinear medium of length L, so long as the relation $2z_R > L$ holds, we can treat Gaussian beams focused on nonlinear media as plane waves with a high degree of accuracy. Another way of visualizing this is to look at Eq. (2-60): with the right experimental conditions (beam focus centered in nonlinear crystal, crystal length L is greater than or equal to twice the Rayleigh range), we can assume the beam size changes slowly enough that we approximate $w(z)$ as a constant and equal to the beam waist w_0. This condition is called confocal focusing and it is often used for experimental work, as it provides >80% of the maximum efficiency while requiring a less tight focus inside of the nonlinear medium, reducing the chance for thermal damage to the crystal.

So, the equations from Section 2.5.1 are valid when the Gaussian beams are confocally focused. However, confocal focusing is not the optimum focusing condition if we aim to maximize the conversion efficiency, so we must consider arbitrary focusing and beam overlap. This problem was first treated in the literature

by Boyd and Kleinman in 1968 as a foundational paper deriving optimal focusing conditions for gaussian beams [45]. This thesis makes use of a more modern derivation that simplifies some of the computational work involved by Guha et al., but the underlying ability to model Gaussian beam focusing remains the same [14], [46]. The main result is a two-dimensional overlap integral that is a function of dimensionless parameters representing the focusing conditions and the phase mismatch, both of which can be controlled during the experiment to optimize conversion efficiency. The derivation is lengthy and takes up the majority of the paper, so only the final result is presented here. The derived function h represents the complex double integral with numerous dimensionless terms defined in order to simplify the notation and the numerical calculations:

$$h = \left(\frac{1}{4\xi_4}\right) I,$$

$$I = \int_0^1 \int_0^1 dz_1 dz_2 \times \frac{\exp[i\Delta kl(z_1 - z_2)] \exp\left[-\left(\frac{4B^2}{\alpha}\right)(z_1 - z_2)^2 f\right]}{(z_1 - A)(z_2 - A_1^*) + C_1} \qquad (2\text{-}61)$$

Where:

$$k = \frac{k_1}{k_2}$$

$$B = \frac{\rho}{2}\left(\frac{l(k_1 + k_2)}{2}\right)^{\frac{1}{2}}$$

$$\xi_1 = l/(2z_{R1})$$

$$\xi_2 = l/(2z_{R2})$$

$$\xi_3 = \frac{\xi_1\xi_2(1+k)}{\xi_2+k\xi_1}$$

$$\xi_4 = \frac{\xi_1+k\xi_2}{1+k} \tag{2-62}$$

$$\alpha = \frac{\xi_1+k\xi_2}{(1+k)\xi_1\xi_2}$$

$$A_1 = \frac{1}{2} + \frac{i}{4}\left(\frac{1}{\xi_3} + \frac{1}{\xi_4}\right)$$

$$C_1 = -\frac{1}{16}\left(\frac{1}{\xi_3} - \frac{1}{\xi_4}\right)^2$$

$$z_3' = \frac{1}{2} + \frac{i}{2\xi_3}$$

And

$$f = \frac{(z_1 - z_3')\left(z_2 - z_3'^{*}\right)}{(z_1 - A_1)(z_2 - A_1^{*}) + C_1} \tag{2-63}$$

This integral allows us to plot the efficiency as a function of the overlap between the two input beams according to the focus factors $\xi_{1,2} = L/2z_{r1,2}$ which are simply the length of the nonlinear medium divided by twice the Rayleigh range. When $\xi = 1$ the confocal focusing condition is met. This h integral can be converted into overall predicted DFG output power in watts using the following relation from Guha et al. [14]:

$$P_1 = \frac{P_2 P_3}{P_{DFG}} h \tag{2-64}$$

Where P_1 is the DFG power at the output facet of the nonlinear medium, P_2 and

P_3 are the powers of the pump and signal beams at the input of the nonlinear medium, and $P_{DFG} = (c\epsilon_0 n_3^2 \lambda_1 \lambda_2^2)/(32\pi^2 d_{eff}^2 L)$ is a collection of constants and experimental parameters. A similar relation was derived by Guha and Falk for SFG [46].

To illustrate how this can be used to optimize the beam overlap, consider Figure 2-7, which is a plot of h versus some experimental data from one of the author's co-authored research articles [47]:

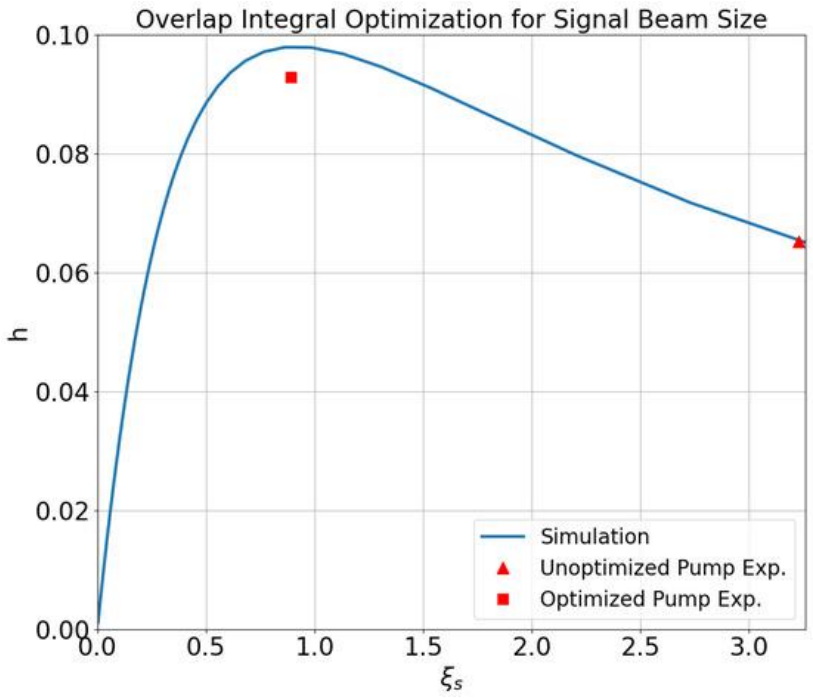

Figure 2-7 A plot of the overlap integral for the case of difference frequency generation utilizing a 1064 nm pump beam and a C-band signal beam to produce a MWIR idler beam. The x-axis represents the focus factor of the C-band signal beam which is varied, while the focus factor of the 1064 nm pump is fixed due to the cavity design. The y-axis represents the value of h which can be tied directly to device efficiency.

In this experiment, a 1064 nm diode-pumped solid state laser was used as one of the input beams for DFG, where the nonlinear medium was located inside of the cavity. This fixed the focus factor of the 1064 nm beam, which in this case was $\xi_p = 0.394$, which represents a defocused beam. The C-band signal was initially over-focused, represented by the red triangle in Figure 2-7 with a focus factor of $\xi_s = 3.23$. The simulation curve in blue predicted that by defocusing the signal beam, the efficiency could be improved from $h = 0.0652$ to $h = 0.0963$, representing an improvement of $\text{Efficiency} = \frac{0.0963}{0.0652} = 47.7\%$. When experimentally implemented, the new efficiency matched a value of $h = 0.09282$ at a signal focus factor of $\xi_s = 0.8922$, which is in good agreement with the prediction from the simulation. Adding this functionality allowed the modelling of the beam overlap, showing that the beam overlap in the original design was poor and leading to >40% gain in efficiency with minimal adjustments to the overall experimental setup. This should demonstrate the importance of incorporating this consideration when performing any three-wave mixing experiments, as it can have a significant impact on the overall device performance.

2.5.3 Guoy Phase

Another important physical phenomenon that arises using focused Gaussian beams is the Guoy phase shift. As a Gaussian beam passes through the focus, it acquires

an extra longitudinal phase shift known as the Guoy phase shift, represented mathematically as [48]:

$$\phi_G(z) = \arctan\left(\frac{z}{z_R}\right) \tag{2-65}$$

Where z_R is the Rayleigh range. Over the entire propagation through the focus, the beam accumulates a π phase shift. This must be considered in addition to the propagation phase from the k vectors discussed previously. This was considered previously in Boyd and Kleinman's paper deriving the optimal focus factor of $\xi = 2.84$, and is a result of maximizing the intensity of the pump field inside the nonlinear medium while considering the constraints imposed by the Guoy phase shift. Using SHG as an example, we can see that the fundamental beam and the second harmonic beams will accumulate differing Guoy phases. This is due to the second harmonic having a smaller Rayleigh length, and so the Guoy phase increases at a faster rate relative to the fundamental. This introduces a length-dependent phase mismatch in addition to the k-vector mismatch due to dispersion derived previously. This means that the phase matching condition can only be satisfied locally, and not globally throughout the crystal when using focused gaussian beams.

The Guoy phase also introduces an interesting observable phenomenon as a result. We know from plane-wave theory that the phase matching curve is predicted to be a symmetrical sinc^2 function. However, the extra phase shift introduced by the Guoy phase term means that the nonlinear conversion efficiency is no longer maximized when $\Delta k = 0$. Instead, the symmetry is broken, and the optimal phase

matching occurs when the Guoy phase induced mismatch is compensated by a small nonzero material phase mismatch. In other words, by deliberately de-tuning Δk to a small positive value, it is possible to cancel the Gouy contribution and maximize net constructive interference. This is demonstrated by Boyd in his textbook on nonlinear optics and has been demonstrated experimentally. If one plots the nonlinear output power as a function of one of the variables that affect Δk, such as temperature, the asymmetry becomes obvious and more pronounced as the beam becomes more tightly focused [49]. This can be seen in Fig 2-6 below, taken from some experimental work in our lab [50].

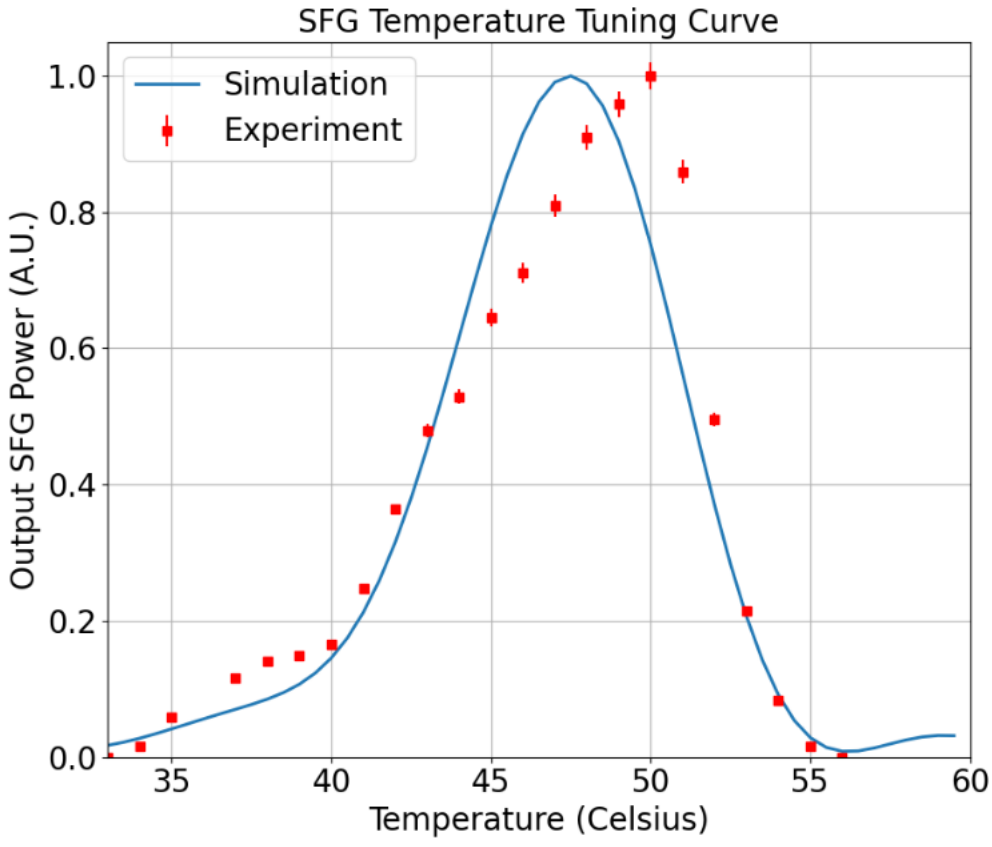

Figure 2-8 Theoretical temperature tuning curve (blue line) compared to experimental data (red

squares). The pronounced asymmetry on the left side of the curve is a direct result of using tightly focused gaussian beams, and the resulting Guoy phase shift.

This phase shift is mentioned here as it is another important consideration that differs significantly from the predictions used in plane wave theory. When using confocal focusing or loose focusing, the plane wave theory is sufficient and shows good agreement with experimental results. However, when attempting to maximize conversion efficiency, tightly focused gaussian beams can achieve higher efficiencies, although this introduces new challenges represented by the optimization of the focus factors and compensating the Guoy phase shift that were previously unimportant. The maximum focus factor derived by Boyd and Kleinman represents the average power density across the crystal that best compensates the Guoy phase shift for the case of using focused Gaussian beams. For generalized three-wave mixing, simulation work is required as the ideal focus factor will depend on the input wavelengths and waist sizes of the two input beams, as well as the length and material of the nonlinear medium.

Chapter 3. Study of Fundamental Wave Depletion in Intracavity Second Harmonic Generation

This chapter is reproduced from a journal article ***L.Flannigan,*** *T. Kashak, and C.Q. Xu, "Study of fundamental wave depletion in intracavity second harmonic generation," Opt. Express 29, 6810-6823 (2021). Reproduced with permission from Optica under BOIA open access agreement. The author is the first author and main contributor of this publication.*

Preface: The goal of this research was to develop a model for intracavity SHG that combined the coupled nonlinear wave equations with a rate equation model for diode-pumped solid-state lasers. This would allow for accurate modeling of the depletion of the fundamental wave (1064 nm in this case) in the cavity as a result of the SHG nonlinear process. While depletion of the fundamental had been modelled previously through different methods, these prior models did not account for the dependence of this process on operation temperature and pump power simultaneously. Since this new method could capture these phenomena, the model successfully predicts all three main features of an intracavity SHG

temperature tuning curve and showed excellent agreement with experimental data. This foundation of using rate equation cavity modelling to estimate the circulating fundamental power to use as input to a nonlinear coupled wave simulation was generalized to SFG and DFG in the following chapters, and so this work proved to be quite useful in the development of this thesis.

This paper was coauthored with Tyler Kashak who helped with experimental work as well as helped edit the manuscript. This research article has been published in Optics Express.

3.1 Abstract

In this paper, a novel approach to modelling intracavity second-harmonic generation (SHG) in periodically poled MgO-doped lithium niobate (PPLN) is presented and verified against experimental results. This approach involves combining the coupled nonlinear wave equations with a rate equation model for a diode-pumped solid-state Nd:YVO_4 laser, taking into account both the depletion of the fundamental wave due to the energy conversion from the fundamental wave to the SHG wave and the reduction of the fundamental wave within a laser cavity due to the loss as a result of the SHG nonlinear process. It was shown that the theoretical simulation matched the experimental results well, while also providing physical insight into the importance of the fundamental wave depletion in the intracavity SHG nonlinear processes. The resulting model is computationally simple and has potential to generalize to the other nonlinear processes such as three-wave mixing and optical parametric oscillation.

3.2 Introduction

Intracavity second harmonic generation is one of the most fundamental frequency conversion techniques, and as such has served as the basis for several useful applications. Some example applications include laser ranging, medicine, satellite communication, and laser projection [1–4]. The advantage of the intracavity design over the simpler single pass design, where the crystal is located outside of the laser cavity, is tied to the intensity dependence of nonlinear frequency conversion. The

intensity of the fundamental wave is significantly higher when it is confined inside of a resonator structure, and thus efficient SHG can be achieved. Therefore, it was a natural conclusion to place the nonlinear crystal inside the laser cavity for higher conversion efficiencies. Many nonlinear crystals have been used for intracavity SHG applications, such as KH_2PO_4 (KDP), LiB_3O_5 (LBO), β-BaB_2O_4 (BBO), $KTiOPO_4$ (KTP), and $LiNbO_3$ (LN). These crystals have varying advantages and disadvantages, but all can be used to successfully frequency double light in the visible and near-infrared wavelength ranges. As a result of intracavity SHG's nature as a fundamental nonlinear process, it has been extensively studied. This has resulted in an evolving model of the physics of intracavity SHG over the last ~50 years. Early models developed by Polloni et al., Smith, Kennedy et al., and Volosov et al. focussed on single mode operation and derived several useful relations, such as the maximum output power of SHG being equal to the maximum output power at the fundamental wavelength and the well known "phase problem" resulting in half the generated SHG power being lost to absorption or destructive interference in the cavity [5–9]. Further developments of the model by Rice et al., Baer, and Oka et al. expanded the model to include multiple modes and polarization of the fundamental and second harmonic waves and showed that multiple longitudinal modes could cause instabilities through both SHG and sum frequency generation [10–12]. These models have been instrumental in furthering the understanding of intracavity SHG for both theoretical and practical purposes. It is well known that two mechanisms can cause the depletion of the fundamental wave in the intracavity

SHG process. First, the energy conversion from the fundamental wave to SHG wave in the SHG nonlinear process results depletion of the fundamental wave. Second, as a result of the first process, the circulating fundamental power within the laser cavity is reduced due to the additional loss of the fundamental wave caused by the SHG nonlinear process. However, to date, the depletion of the fundamental wave due to these two mechanisms and its dependence on operation temperature and pump power in intracavity SHG has not been well studied.

To date, a model that comprehensively examines the depletion of the fundamental wave in intracavity SHG and shows good agreement with experimental results has not been reported. In the models mentioned previously, the depletion effect was accounted for by fitting a nonlinear coupling coefficient to a rate equation model of the laser cavity, and this coefficient was used as a constant fitting parameter and was independent of operation temperature [5–12]. As a result of this approach, the previous models could not explain simultaneously both the main peak and side peaks in the measured SHG temperature tuning curve (in terms of SHG power and bandwidth).More specifically, the reported models could not predict all three main features of an intracavity SHG temperature tuning curve: the peak power of the main peak [7], [9–12], the width of the main peak (temperature tolerance, measured as full width half maximum of the main peak) [5], [7–9], [11,12], and the height of the side peaks [5–12].

In this paper, for the first time, we present a model that comprehensively and intuitively models the depletion of the fundamental wave in intracavity SHG due to

both the mechanisms mentioned above. It is shown that by considering the depletion of the fundamental wave as a function of temperature and pump power, it is now possible to explain the reduced peak power, wider temperature bandwidth, and taller side peaks observed in SHG temperature tuning curves. The model is validated against experimental data for periodically poled lithium niobate (PPLN).

3.3 Theory

In this model, we are considering the pump power incident on a laser crystal (e.g. Nd:YVO_4) to generate a fundamental wave within a laser cavity formed by two mirrors. The fundamental wave will be incident on a nonlinear crystal (e.g. PPLN) to generate an SHG wave. Linear and nonlinear losses in the cavity were considered in the model. The linear loss is a result of imperfect coatings at the facets of the laser crystal, nonlinear crystal, and mirrors, while the nonlinear loss is caused by both the depletion of the fundamental wave (due to the energy conversion from the fundamental wave to SHG wave) and reduction of the fundamental wave within the laser cavity due to the cavity loss as a result of the SHG nonlinear process. The novel part of this model is that we consider the nonlinear loss as a function of operation conditions (i.e., PPLN temperature and pump power) in simulating the temperature tuning curve, instead of treating the nonlinear loss as a fitting parameter to match the simulations with the measured experimental data as reported in the literature.

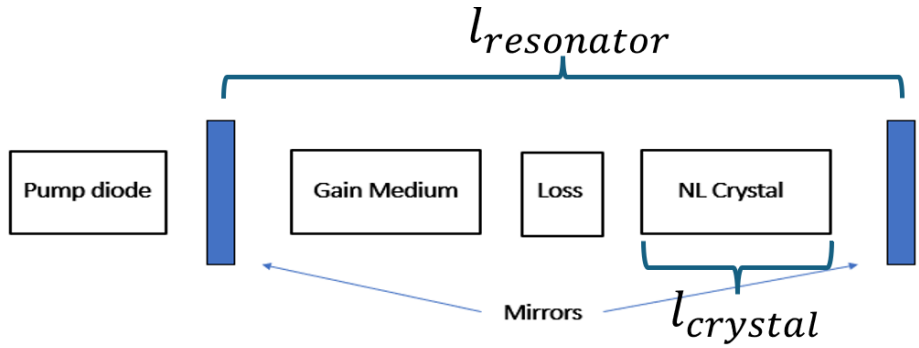

Figure 3-1 The intracavity SHG structure being simulated consists of a pump diode (808 nm), a gain medium (Nd:YVO_4), all sources of loss (absorption, scattering, nonlinear depletion, etc.) and the nonlinear crystal producing the SHG output (PPLN).

Thus, the first step is to determine the intracavity power for the fundamental wave, which was done using a plane wave solid state laser rate equation. Since the gain medium is the well-studied Nd:YVO_4, a four-level laser model is suitable, and results in the two following differential equations [13]:

$$\frac{d}{dt}N_2 = \frac{\eta_{pump}P_{inc}(1-\exp(-\alpha z))}{h\nu_{pump}V_{crystal}} - \frac{c\phi}{XYl_0}(\sigma_{em}N_2) - \frac{N_2}{\tau_2} \qquad (3\text{-}1)$$

$$\frac{d}{dt}\phi = \frac{c\phi l_{crystal}}{l_0}(\sigma_{em}N_2) - \frac{\phi}{\tau_c} \qquad (3\text{-}2)$$

where N_2 is the population of the upper level of the gain medium, ϕ is the photon density, η_{pump} is the efficiency of the pump as a percentage, P_{inc} is the incident optical power of the pump diode onto the gain medium, α is the absorption coefficient of the pump light in the gain medium, z is the length of the gain medium, h is Planck's constant, ν_{pump} represents the frequency of the pump light, c is the

speed of light, $V_{crystal}$ is the volume of the gain medium , XY is the facet area of the gain medium , $l_0 = l_{resonator} + (n-1)l_{crystal}$ represents the optical length of the resonator with $l_{resonator}$ being the length of the resonator and $l_{crystal}$ the length of the gain medium, n is the refractive index of the gain medium, σ_{em} is the stimulated emission cross section for the gain medium, τ_2 is the upper level lifetime of the gain medium, and τ_c is the photon lifetime term.

The first equation represents the population of atoms in the upper level of the gain medium, while the second equation represents the photon density in the resonator. The value of each parameter used in the simulations will be presented in Section 3. These equations can be numerically integrated to provide a steady-state photon density, which can be converted to an intracavity power using the following relation:

$$P_{cav} = \frac{V_{mode} h\nu_{laser} \phi}{t_r} \tag{3-3}$$

Where $V_{mode} = XYl_0$ is the mode volume where we have assumed that the mode diameter is equal to the facet area, ν_{laser} is the frequency of the fundamental wave, and $t_r = 2l_0 / c$ is the round-trip time of the resonator. The output power of the fundamental wave is calculated as

$$P_{out} = (1 - R_{oc}) P_{cav} \tag{3-4}$$

where R_{oc} is the reflectivity of the output coupling mirror. The one disadvantage of this plane wave approach is that the spatial distribution of the photons in the cavity is neglected. This is a reasonable assumption in this case as we are only interested in the total intracavity power, but it does prevent the modelling of more complicated phenomena such as beam overlap in the nonlinear crystal. It is also assumed that the circulating forward and backward power in the cavity is equal:

$$P_{cav} = P^{+} + P^{-} \cong 2P^{+} \tag{3-5}$$

where P+ and P- are the forwards and backwards power circulating in the cavity, respectively.

The novel part of the intracavity model with regards to previous models is introducing the nonlinear loss in the photon lifetime term τ_c. The photon lifetime is determined by dividing the round-trip time of the resonator with a loss term δ:

$$\tau_c = \frac{t_r}{\delta} \tag{3-6}$$

where the loss term includes the linear loss (such as mirror loss and facet reflection loss), and the nonlinear loss induced by the SHG nonlinear process, which in previous models is typically incorporated as a single nonlinear coupling coefficient that does not change with temperature and pump power:

$$\delta = \alpha_{mirror} + \alpha_l + \alpha_{NL} = \ln(\frac{1}{R_{oc}R_{in}}) + \alpha_l + \alpha_{NL} \quad (3\text{-}7)$$

where α_{mirror} is the loss caused by the end mirrors of the cavity, R_{in} is the input coupling mirror located after the pump diode, α_l is the linear loss which includes loss due to scattering, absorption, imperfect anti-reflection coatings, and any other sources of intrinsic loss, and α_{NL} is the nonlinear loss as a result of the SHG nonlinear process. In our model, nonlinear loss α_{NL} is continually updated at each temperature for a given pump power by multiple iterations of the intracavity equations and nonlinear wave equations. The nonlinear loss is defined using the depleted fundamental cavity power each iteration, ensuring that the depletion effect is accounted for in the nonlinear loss term. Additionally, the depletion of the fundamental wave inside the nonlinear crystal is accounted for in the nonlinear coupled wave equations, and so the calculated nonlinear coefficient includes both the nonlinear depletion and the additional nonlinear cavity loss mechanisms discussed previously. Initially, the nonlinear loss in the resonator is zero as there is no generated SHG power, and so we must determine the initial intracavity power available for SHG using equations 3-1, 3-2, and 3-3. Once the nonlinear SHG power P_{NL} is derived, the nonlinear loss is then calculated as:

$$\alpha_{NL} = \frac{532nm}{1064nm}(\frac{P_{NL}}{P_{cav}}) \quad (3\text{-}8)$$

As the rate equations track the number of photons inside of the cavity, it is important to track the number of photons lost to the nonlinear conversion. This is accounted for by adding the wavelength ratio in Eq. 3-8, converting the power ratio to a photon ratio. In all cases, the various loss terms are typically represented as decimal percentages (i.e. a 1% round trip loss would be α=0.01). The next step is to determine the SHG power using the coupled wave equations as derived by Boyd [14]:

$$\frac{dA_1}{dz} = \frac{2i\omega_1^2 d}{k_1 c^2} A_2 A_1^* \exp(-i\Delta k z) \tag{3-9}$$

$$\frac{dA_2}{dz} = \frac{i\omega_2^2 d}{k_2 c^2} A_1^2 \exp(i\Delta k z) \tag{3-10}$$

In which the first equation represents the evolution of the fundamental wave and the second equation represents the generated second harmonic wave. In the equations, A_1 and A_2 are the field amplitudes of the fundamental and second harmonic waves, respectively. d is the nonlinear coefficient of the nonlinear crystal along the propagation direction of the fundamental wave, which for PPLN is typically d_{33}, z is the propagation distance into the nonlinear crystal, ω_1 and ω_2 are the angular frequencies of the fundamental and second harmonic waves, respectively, and $\Delta k = 2k_1 - k_2 - 2\pi/\Lambda$ is the phase mismatch between the fundamental and second harmonic waves, where $k_i = 2\pi n_i / \lambda_i$ is the wave number and the last term represents the effective momentum imparted by the periodic

poling of the nonlinear crystal with period Λ. The temperature dependence of the phase matching can be modelled by the Sellmeier equation for magnesium doped PPLN [15]:

$$n_e^2 = a_1 + b_1 f + \frac{a_2 + b_2 f}{(\lambda^2 - (a_3 + b_3 f))^2} + \frac{a_4 + b_4 f}{\lambda^2 - a_5^2} - a_6 \lambda^2 \qquad (3\text{-}11)$$

where a1, a2, … a6 and b1, … b4 are the Sellmeier coefficients provided in [15], and the temperature dependent parameter f is defined as

$$f = (T - 24.5°C)(T + 570.82) \qquad (3\text{-}12)$$

where T is the temperature of the crystal in $°C$.

The coupled wave equations can then be numerically integrated by selecting an operating temperature for the nonlinear crystal, where we have assumed that the temperature is held constant via an attached heat sink and thermoelectric cooler in experiments. The step size for the numerical integration is half the poling period of the nonlinear crystal. This is due to the fact that the sign of the nonlinear coefficient will change when the domain of the nonlinear crystal is inverted. As we are assuming equal positive and negative poling (i.e. the poling follows a square wave pattern with a 50% duty cycle, alternating between positive and negative), this leads to a step size of one half the period as the domain flips each half-period. It is also assumed that the initial SHG power is zero.

Now that all the individual parts of the model are accounted for, they can be combined into the final numerical model. This is done by first determining the circulating fundamental wave power in the resonator with rate equations, and then using this fundamental power to calculate the appropriate SHG power and corresponding nonlinear loss. Then, the intracavity power is updated using the new loss, generating a new SHG power and loss, and the process continues until the SHG power is no longer changing between iterations. The flowchart in Figure 3-2 illustrates each step of the model, which is carried out at multiple temperatures to generate temperature tuning curves that can be easily replicated in the experiments using a thermoelectric cooler attached to the nonlinear crystal.

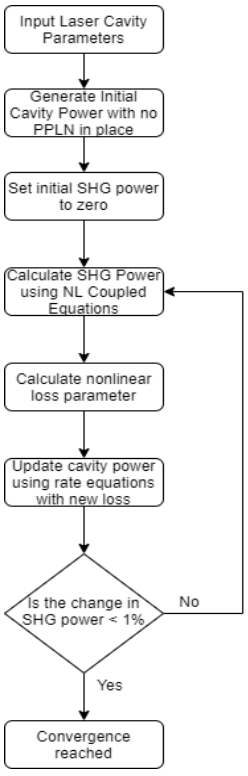

Figure 3-2 A flowchart illustrating the steps carried out by the Python script to generate the final

temperature tuning curves. This process is repeated at each temperature until a sufficient temperature tuning curve is generated.

Equations 3-1, 3-2, 3-9, and 3-10, were implemented in Python and numerically integrated using a fourth order Runge-Kutta solver from the SciPy library. We can infer from the flowchart that the initial nonlinear loss will be quite high, as the estimated SHG power will be highest in the first iteration. The nonlinear loss was determined using equation 3-8, where the total generated SHG power is compared to the initial fundamental power. While the forwards and backwards power circulating in the cavity contribute to the nonlinear loss, it is assumed that only the forward power generates useable SHG power, as Smith showed that the backwards SHG power is typically absorbed in the gain medium [6]. In the following iteration, the addition of the nonlinear loss greatly decreases the circulating cavity power, and thus the next estimate of the SHG power will be significantly lower. This leads to a lower nonlinear loss term than the first iteration. This process will continue, and each iteration the nonlinear loss will come closer to converging on the true "final" value of nonlinear loss, and thus the expected SHG power, at each temperature. In the previous models, it is typically assumed that the circulating fundamental power at each temperature is a constant determined by a fitting parameter called the nonlinear coupling coefficient. The novelty of our approach is that a unique nonlinear loss and thus a unique fundamental power is associated with each temperature, greatly increasing the height of the side peaks, and increasing the

temperature bandwidth of the main peak. The predicted temperature tuning curves generated by the model are compared to experimental results in Section 4.

3.4 Experimental Setup

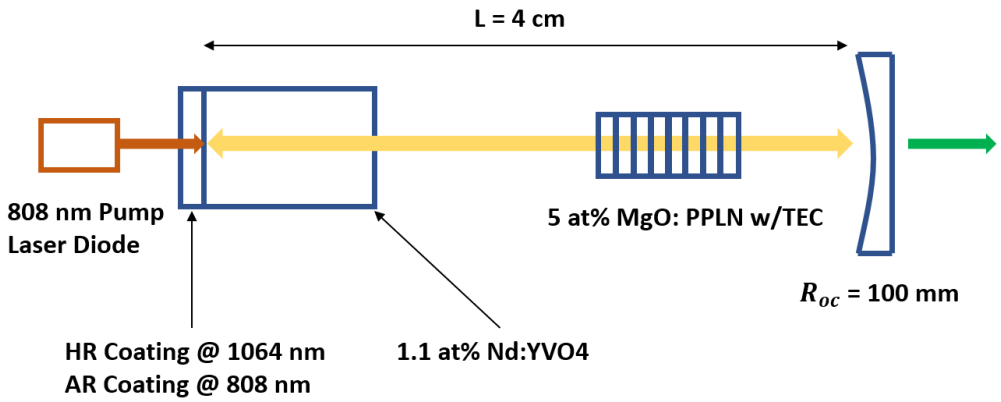

Figure 3-3 Experimental intracavity SHG setup

The experimental setup, illustrated in Figure 3-3, is a diode-pumped solid-state (DPSS) laser-based resonator with a frequency doubling nonlinear crystal inserted into the cavity. An 808 nm pump diode emitting up to 5.5 W optical power was launched into a 1.1 atomic percent Nd:YVO_4 laser crystal with dimensions of 3x3x5 mm. The Nd:YVO_4 input facet had a high reflection coating at 1064 nm and high transmittance coating at 808 nm that serves as the end mirror for the cavity. The output facet of the Nd:YVO_4 had an anti-reflection coating at 1064 nm, followed by a PPLN crystal which was mounted to a heat sink with a thermoelectric cooler that can be controlled to within 0.1 °C. There was an output coupler positioned after the output facet of the PPLN that had high reflectivity at 1064 nm and high

transmittance at 532 nm. The facets of PPLN were anti-reflection coated at 1064 nm to minimize round-trip losses in the cavity. The mirror-to-mirror cavity length was set to 40 mm. This forms the basic SHG intracavity structure used in the experiments. For the simulation inputs, some values that could not be easily measured via experiment such as the absorption and stimulated emission cross sections were taken from the reported papers [15–20]. The inputs to the simulation are listed in Table 3-1.

Table 3-1 The parameters used in the coupled rate equation model. Parameters were measured experimentally where possible.

Parameters	**Values**	**Ref.**
Nonlinear coefficient (d_{33})	27 pm/V	[16]
Pump efficiency (η)	70%	[17]
Nd:YVO_4 length ($l_{crystal}$)	0.5 cm	[this work]
Resonator length ($l_{resonator}$)	4 cm	[this work]
Output coupler reflectivity at 1064 nm (R_{oc})	99.87%	[this work]
Linear losses (α_l)	0.135%	[this work]
Nd:YVO_4 absorption cross section at 808 nm (σ_{abs}) [18]	$2.5 \times 10^{-19}\text{cm}^2$	[18]

Nd:YVO_4 stimulated emission cross section 1064 nm (σ_{em}) [19]	$25 \times 10^{-19}\text{cm}^2$	[19]
Density of active ions in 1 at. % Nd:YVO_4	$1.24 \times 10^{20}\ \text{cm}^{-3}$	[this work]
Nd doping	1.1 at. %	[this work]
Upper-level lifetime (τ_2) [18]	90 µs	[18]
Nd:YVO_4 refractive index ($n_{crystal}$) [20]	2.16	[20]
PPLN refractive index at 50°C (n_{PPLN}) [15]	2.155	[15]
Pump wavelength (λ_{pump})	808 nm	[this work]
Fundamental wavelength (λ_{fun})	1064 nm	[this work]
Nd:YVO_4 facet dimensions (A_{facet})	0.3x0.3 cm	[this work]
PPLN crystal length (l_{PPLN})	0.11 cm	[this work]
PPLN period (Λ)	6.93 µm	[this work]
Beam diameter in PPLN	65 µm	[this work]
808 nm optical pump power	5.11 W	[this work]
Output Coupler Radius	100 mm	[this work]

3.5 Discussion/Results

3.5.1 Model validation:

To validate the model, simulations are compared with the observed experimental results. The first thing that must be validated is the plane wave rate equation model, as modelling the laser cavity accurately is required to ensure accurate SHG results. The first experiment that was performed was measuring the leaking 1064 nm power from the laser cavity with a dummy PPLN crystal inserted. The dummy PPLN was a crystal of equivalent length to the PPLN used in the SHG experiments, however the temperature of the PPLN crystal was tuned to ensure that no SHG light was being generated. This allowed us to be confident that the experimental results included the additional insertion loss of the PPLN crystal without including any nonlinear loss from SHG. This was verified by measuring the output power of the laser with and without a 1064 nm optical filter placed in front of the power meter. The leaking pump power from the 808 nm pump diode was measured to be ~3 mW and was subtracted off all measurements, and the experimental results include the loss from the output coupler and the wavelength filter. This additional loss is accounted for in the simulation as well. In Figure 3-4, the x-axis is the 808 nm optical pump power, and the y-axis is the leaking 1064 nm power. The squares represent the experimental data while the solid line represents the predicted leaking power from the simulation. The simulation parameters used are shown in Table 3-1. As shown in Figure 3-4, after overcoming the laser threshold at ~0.15W pump

power, the leaking 1064 power increases linearly with pump power as expected. As shown in Figure 3-4, the simulation correctly predicts both the slope efficiency of the laser as well as the laser pump threshold, implying that the input parameters of the cavity simulation are correct. The simulation curve was generated by setting the pump power and output coupler reflectivity according to the experimentally measured values, and then varying the linear loss α_l until the slope and threshold predicted by the simulation is correct.

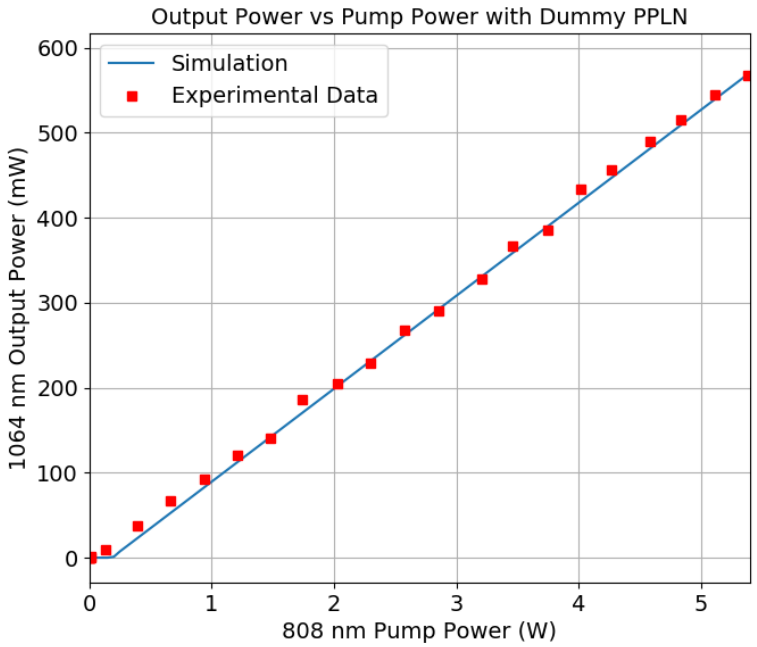

Figure 3-4 Leaking 1064 nm power vs 808 nm pump diode power.

The second verification was to measure the leaking 1064 nm power when the PPLN was temperature tuned to produce maximum SHG power. This metric allows

a direct comparison between the estimated total intracavity power of the simulation versus the experimental results, as the output power can be used to derive the total circulating intracavity power. These results were gathered by placing a 1064 nm filter in front of the power meter that has effectively 0% transmission at 532 nm and subtracting off the 808 nm pump power as mentioned previously. In Figure 3-5, the x-axis is the 808 nm optical pump power, and the y-axis is the leaking 1064 nm power. The squares represent the experimental data while the solid line represents the predicted leaking power from the simulation. The simulation parameters used are shown in Table 3-1. The "Correct" PPLN referred to in the title is a PPLN crystal that has been temperature tuned for optimal SHG conversion efficiency. As shown in Figure 3-5, with the increase of 808 nm pump power, the leaked 1064 nm fundamental wave power increases linearly. The simulations agree well with the experimental results, implying that there is a significant reduction in the circulating 1064 nm power once SHG begins due to the noticeable drop (~200 mW) in leaking 1064 nm power.

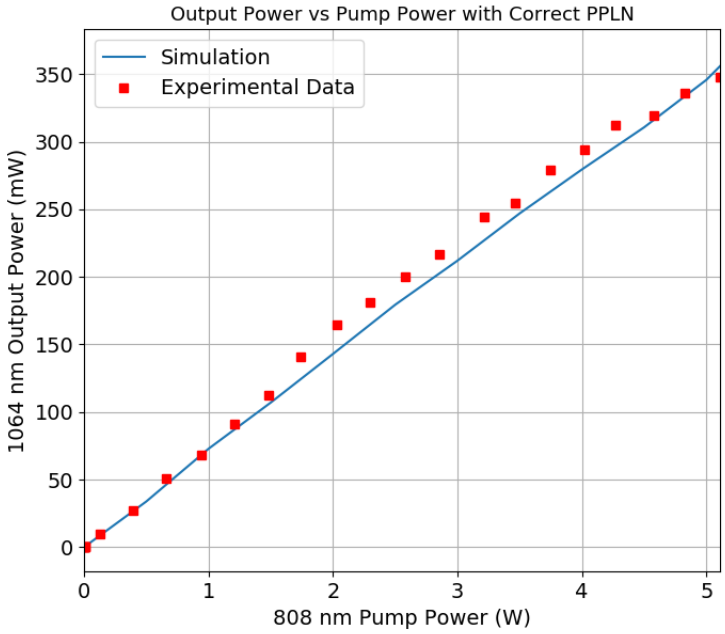

Figure 3-5 Leaking 1064 nm power vs. 808 nm pump power when SHG power was maximized.

The final validation was the comparison of the temperature tuning curves predicted by the simulation versus the experimental temperature tuning curve for a 1.1 mm long PPLN crystal. In Figure 3-6, the x-axis is the temperature of the nonlinear crystal in degrees Celsius and the y-axis is the 532 nm SHG power measured at the detector. The squares represent the experimental data while the solid line represents the predicted SHG power from the simulation. The simulation parameters used are shown in Table 3-1, and the experimental setup is described in Section 3. As shown in Figure 3-6, the changing temperature of the nonlinear crystal significantly affects the phase matching and thus the efficiency of the nonlinear process. We can see excellent agreement between the predicted temperature tuning curve and the experimental results, with the only discrepancy being the non-

symmetrical nature of the experimental data versus the simulated results. This is most likely a combination of two problems, which is defects in the PPLN due to manufacturing limitations, as well as the attached TEC being unable to completely eliminate temperature gradients in the crystal, causing thermal lensing which may differ with temperature. It can also be observed that the simulation correctly predicts the temperature bandwidth of the main peak and the peak SHG power. These results are promising, as it implies that the main factor that must be considered to properly model intracavity SHG is the induced depletion of the fundamental wave and the resultant loss of the circulating fundamental power within the cavity, which we have considered in our model. The results in Figure 3-6 were collected by introducing a 532 nm filter in front of the power meter to filter out the leaking 1064 nm light as well as accounting for the transmission of the output coupler for 532 nm (T~99%).

The experimental data in Figures 3-6 exhibit the three main features of intracavity SHG, with a lower peak power than that predicted from single pass theory, a noticeably higher temperature tolerance, and pronounced side peaks. As shown in Figure 3-6, our model successfully predicts the peak value and temperature bandwidth and matches the side peaks relatively well. For comparison's sake, the temperature bandwidth observed for intracavity SHG is ~30 degrees, while single pass theory predicts a temperature bandwidth of ~18 degrees for the same crystal. This illustrates the importance of modelling the intracavity SHG processes well, as the temperature bandwidth increases by ~67%.

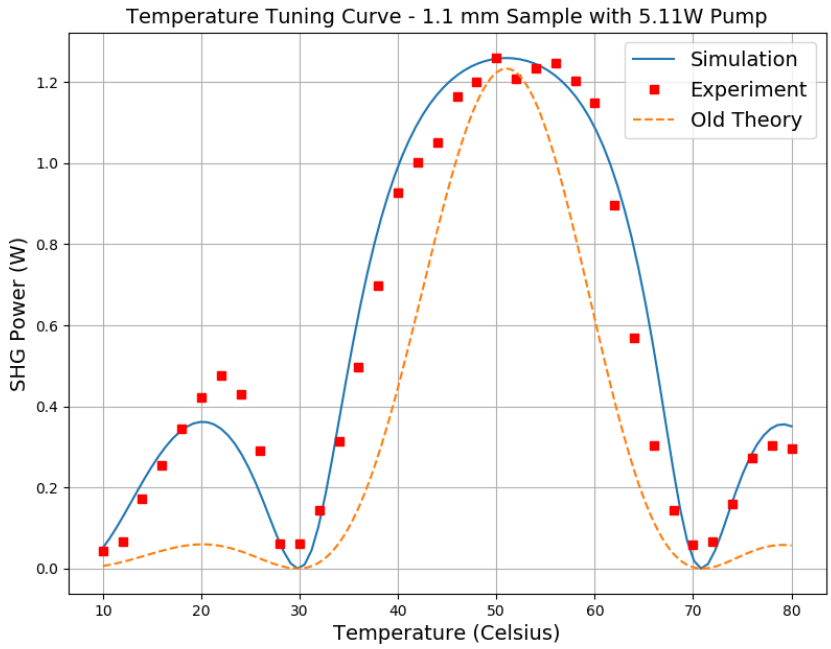

Figure 3-6 Experimental results for 1.1 mm long PPLN sample compared to the predicted results from the simulation. The asymmetry of the curve is likely due to imperfections in the PPLN and the thermal lensing in the PPLN as a result of temperature gradients in the crystal.

3.5.2 Depletion of fundamental wave:

We can use the results to intuitively explain the physical phenomena that causes these three main effects for intracavity SHG. The higher the efficiency of the nonlinear process, the greater the depletion of the fundamental light and the larger the nonlinear loss is. This results in a wider temperature bandwidth, as the lower SHG efficiency due to phase matching as we move away from the peak temperature is partially offset by a larger input fundamental power due to the lower loss. This also explains the larger side peaks that are observed, as while the phase matching

is much poorer at the side peaks, the fundamental power at the side peak is larger than that of the main peak.

The importance of the nonlinear loss is further reinforced when comparing the SHG temperature tuning curve with and without considering the nonlinear loss. In Figure 3-7, the x-axis is the temperature of the nonlinear crystal in degrees Celsius and the y-axis is the 532 nm SHG power predicted by the single pass theory. The solid line represents the simulation prediction when there is no nonlinear loss and so the single pass input power is equivalent to the circulating cavity power with no nonlinear loss, while the dashed line represents the predicted SHG power when a temperature independent nonlinear loss of 0.45% was added to the single pass model, reducing the input power to the nonlinear crystal significantly. The 0.45% value was calculated using equation 3-8 using only the peak SHG power for P_{NL} .. As an example, if the total forward and backward generated SHG power is 2.4W and the total intracavity power is 265W, then the loss would be 0.45% according to equation 3-8. It is important to keep in mind that only the forward SHG power (1.2 W from the example) would be observed experimentally, but both the forward and backward SHG power contribute to the nonlinear loss in the cavity. The main observation in Figure 3-7 is that if we do not account for nonlinear loss and the resulting drop in fundamental input power, the expected SHG power is significantly higher than what is experimentally observed. We also see that by adding a nonlinear loss term and using the reduced fundamental power results in a prediction that is

much closer to the observed experimental values. As a result, it is clear that the nonlinear depletion must be accounted for to obtain accurate predictions of SHG power.

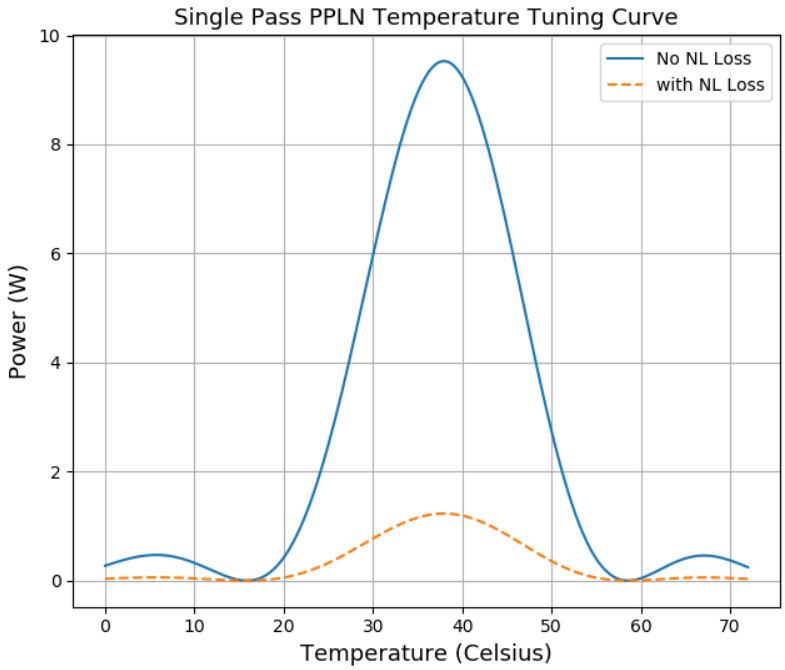

Figure 3-7 Single pass SHG power results when assuming no nonlinear loss versus incorporating the nonlinear loss. The y-axis represents the SHG output power, and the x-axis represents the PPLN temperature.

It is important to point out that the current model is not perfect, as it tends to slightly overestimate or underestimate the side peaks while correctly predicting the peak value and temperature bandwidth of the main peak. This could be due to a number of things, the first being the plane wave assumption used in the cavity rate equation model. This assumption was used as we were only interested in the total circulating intracavity power, and the plane wave assumption allows us to calculate this in a

simple manner. However, the lack of a Gaussian model means that it is not possible to account for the intensity variation in both the transverse plane of the laser and the photon density distribution throughout the cavity. This also means we cannot fully account for the difference in the fundamental beam diameter versus the SHG beam diameter in the PPLN, and so perfect beam overlap was assumed. Another potential issue is that we have assumed that the beam diameter in the PPLN is a constant with temperature. However, Rice et al. showed that even with an appropriate heat sink and temperature controller, significant temperature gradients can arise in the nonlinear crystal, and there is potential for non-uniform thermal effects to change the beam diameter in the PPLN [6]. This could partially account for the slightly incorrect side peaks, although it is still clear that the current model offers an improvement over previous models in this regard. As a result, there is room for improving the model in the future.

There are also two interesting physical phenomena that arise as a result of the new model. The first is that the fundamental wave depletion and nonlinear loss depend on the 808 nm pump power significantly. In Figure 3-8, the x-axis is the 808 nm pump optical power, and the y-axis is calculated nonlinear loss term due to fundamental wave depletion via SHG. The solid line represents the calculated nonlinear loss from the simulation. The simulation parameters used are shown in Table 3-1. The nonlinear loss increases quickly as the pump power increases, and the overall trend is that the rate of change of the nonlinear loss slowly decreases as

pump power is added. We can also observe that at high pump powers (7-8 W) the loss saturates as we reach the maximum SHG power attainable for the crystal. This is a result that, to the best of our knowledge, has not been reported previously and has implications on finding an optimal pump power for a given intracavity SHG application.

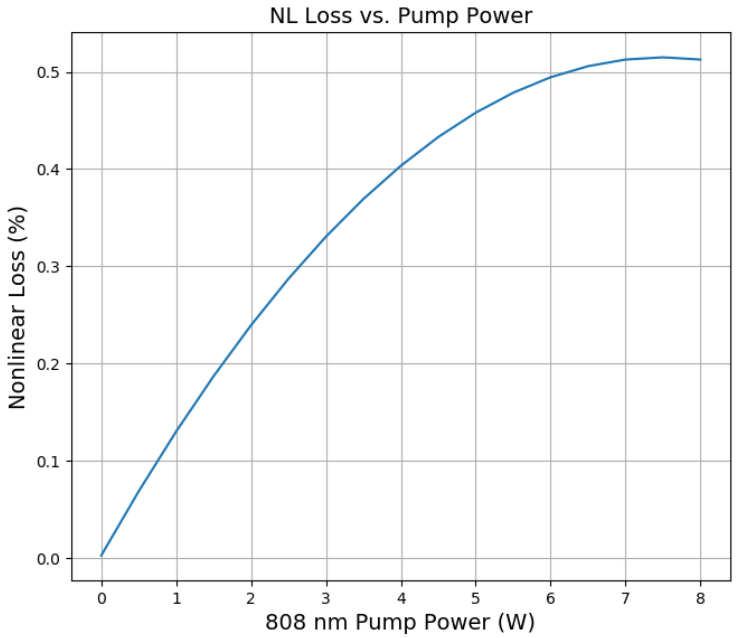

Figure 3-8 The nonlinear loss as a function of the pump power

The second interesting physical phenomenon is that the nonlinear loss and thus the circulating fundamental power has a strong dependence on the temperature. This is to be expected for an intracavity laser, as a small increase in round-trip loss can drastically decrease the fundamental power. As we change the temperature of the PPLN crystal, we also change the SHG efficiency. This greatly affects the induced nonlinear loss and the depletion of the fundamental wave. In Figure 3-9, the x-axis

is the temperature of the nonlinear crystal in degrees Celsius, the left y-axis is calculated nonlinear loss term due to fundamental wave depletion via SHG, and the right y-axis is the circulating fundamental power within the cavity.

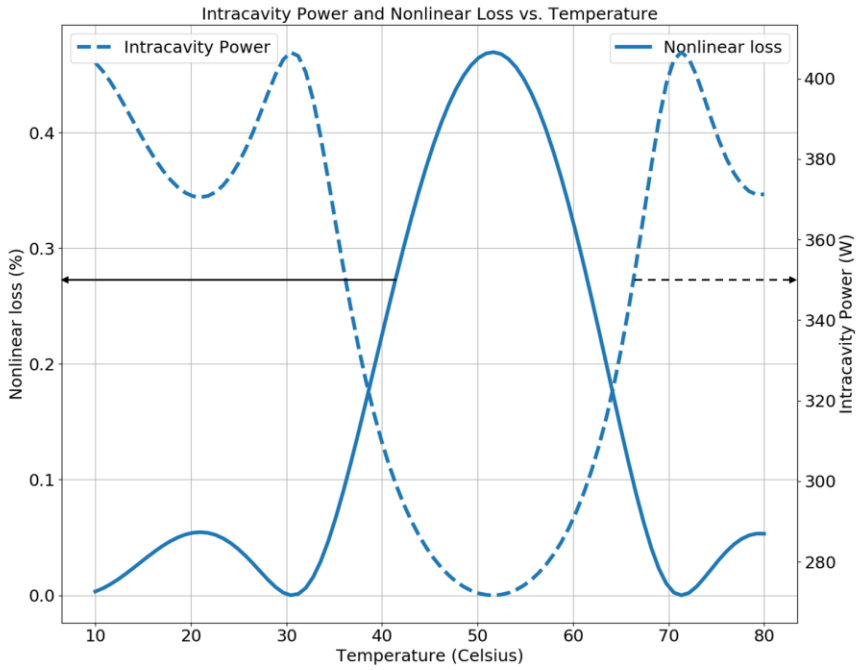

Figure 3-9 Total circulating intracavity power (right axis) and nonlinear loss (left axis) as a function of temperature.

The solid line represents the calculated nonlinear loss from the simulation and corresponds with the left y-axis, while the dashed line represents the circulating fundamental power and corresponds with the right y-axis. The simulation parameters used are shown in Table 3-1. We can see at the points with zero nonlinear loss, the circulating fundamental power is close to 400W, while with a maximum nonlinear loss of 0.45%, the circulating fundamental power drops to ~265W. This is a significant drop in circulating fundamental power and greatly reduces the expected SHG power and the leaking 1064 nm power, which is a result that cannot

be predicted by previous models that use a fixed nonlinear loss at all temperatures. We can see from the agreement of the model with the experimental results that the depletion of the fundamental wave is by far the most important physical phenomena to consider when attempting to model intracavity SHG, as it explains the three effects explained earlier that can be observed in experimental SHG results.

3.6 Conclusion

In conclusion, a plane wave DPSS laser model has been combined with the coupled nonlinear wave equations for second harmonic generation to create a simple and intuitive model of the physics of intracavity generation of green light using PPLN. The simulation results for intracavity SHG agree well with the experimental results. It has been shown that the dominant factor differentiating intra-cavity SHG from single pass SHG is the addition of accounting for the nonlinear loss and the corresponding drop in circulating fundamental power. As a result, the simulation correctly predicts the main peak SHG power, the wider temperature bandwidth, and the more prominent side peaks observed in intracavity SHG experiments. It has been found that the nonlinear loss and fundamental wave depletion depend heavily on both the 808 nm pump power and PPLN temperature. It is expected that the presented model can be applied to the other nonlinear processes such as three wave mixing.

3.7 Acknowledgements

The authors would like to thank Dr. Bin Zhang for the help with experimental setup, Dr. Yi Gan for helpful discussions on modeling, and the NSERC Discovery grant and the Optical Satellite Consortium for the support of the project.

3.8 References

1. G. A. Rines, P. F. Moulton, and J. Harrison, "Narrowband, High-Energy Ti:Al2O3 Lidar Transmitter for Spacecraft Sensing," in *Advanced Solid State Lasers (1989), Paper AA1* (The Optical Society, 2017), p. AA1.
2. H. M. Pask, P. Dekker, R. P. Mildren, D. J. Spence, and J. A. Piper, "Wavelength-versatile visible and UV sources based on crystalline Raman lasers," Prog. Quantum Electron. **32**(3–4), 121–158 (2008).
3. X. Sun, D. R. Skillman, E. D. Hoffman, D. Mao, J. F. McGarry, L. McIntire, R. S. Zellar, F. M. Davidson, W. H. Fong, M. A. Krainak, G. A. Neumann, M. T. Zuber, and D. E. Smith, "Free space laser communication experiments from Earth to the Lunar Reconnaissance Orbiter in lunar orbit," Opt. Express **21**(2), 1865 (2013).
4. T. Yokoyama, K. Mizuuchi, K. Nakayama, A. Kurozuka, T. Sugita, A. Morikawa, and K. Yamamoto, "Compact intracavity green light source with wide operation temperature range using periodically poled Mg:LiNbO3," Jpn. J. Appl. Phys. **47**(8 PART 2), 6787–6789 (2008).
5. R. Polloni and O. Svelto, "Optimum Coupling for Intracavity Second Harmonic Generation," IEEE J. Quantum Electron. **4**(9), 528–530 (1968).
6. R. G. Smith, "Theory of Intracavity Optical Second-Harmonic Generation," IEEE J. Quantum Electron. **6**(4), 215–223 (1970).
7. C. J. Kennedy and J. D. Barry, "Stability of an Intracavity Frequency-Doubled Nd:YAG Laser," IEEE J. Quantum Electron. **QE-10**(8), 596–599 (1974).
8. V. D. Volosov, S. G. Karpenko, N. E. Kornienko, V. L. Strizhevskii, A. A. Man'ko, and V. N. Krylov, "Second-Harmonic Generation in a Resonator.," Sov J Quantum Electron **5**(5), 500–506 (1975).
9. C. J. Kennedy, J. D. Barry, and R. R. Rice, "Measurement of parameters in a mode-locked and frequency-doubled Nd : YAG laser using relaxation oscillations," J. Appl. Phys. **47**(6), 2447–2449 (1976).

10. R. R. Rice, J. R. Teague, and J. E. Jackson, "The effects of optical absorption in Ba2NaNb5O 15 on internal frequency-doubled operation of Nd: YAG," J. Appl. Phys. **49**(12), 5750–5762 (1978).

11. T. Baer, "Large-amplitude fluctuations due to longitudinal mode coupling in diode-pumped intracavity-doubled Nd:YAG lasers," J. Opt. Soc. Am. B **3**(9), 1175 (1986).

12. M. Oka and S. Kubota, "Stable intracavity doubling of orthogonal linearly polarized modes in diode-pumped Nd:YAG lasers," Opt. Lett. **13**(10), 805 (1988).

13. E. H. Bernhardi, C. Bollig, M. J. D. Esser, A. Forbes, L. R. Botha, and C. Jacobs, "A single-element plane-wave solid-state laser rate equation model," S. Afr. J. Sci. **104**(9–10), 389–393 (2008).

14. R. W. Boyd, "Nonlinear Optics," in *Nonlinear Optics*, 4th ed. (Academic, 2020), pp. 91–100.

15. O. Gayer, Z. Sacks, E. Galun, and A. Arie, "Temperature and wavelength dependent refractive index equations for MgO-doped congruent and stoichiometric LiNbO3," Appl. Phys. B Lasers Opt. **91**(2), 343–348 (2008).

16. R. W. Boyd, "Nonlinear Optics," in *Nonlinear Optics* (Academic, 2020), p. 80.

17. Q. Y. Xu, Y. Gan, Y. Lu, X. Li, and C. Q. Xu, "Theoretical analysis of intra-cavity second-harmonic generation of semiconductor lasers by a periodically poled nonlinear crystal waveguide," IEEE J. Quantum Electron. **47**(4), 462–470 (2011).

18. L. Fornasiero, S. Kück, T. Jensen, G. Huber, and B. H. T. Chai, "Excited state absorption and stimulated emission of Nd3+ in crystals. Part 2: YVO4, GdVO4, and Sr5(PO4)3F," Appl. Phys. B Lasers Opt. **67**(5), 549–553 (1998).

19. Y. F. Chen and Y. P. Lan, "Comparison between c-cut and a-cut Nd:YVO4 lasers passively Q-switched with a Cr4+:YAG saturable absorber," Appl. Phys. B Lasers Opt. **74**(4–5), 415–418 (2002).

20. T. S. Lomheim and L. G. DeShazer, "Optical-absorption intensities of trivalent neodymium in the uniaxial crystal yttrium orthovanadate," J. Appl. Phys. **49**(11), 5517–5522 (1978).

Chapter 4. Compact Diode-Pumped Solid-State Laser with Intracavity Pump-Enhanced DFG Emitting at ~3.5 Microns

This chapter is reproduced from a journal article ***L.Flannigan,*** *A. Atwi, T. Kashak, Daniel Poitras, and C.Q. Xu, "Compact Diode-Pumped Solid-State Laser with Intracavity Pump-Enhanced DFG Emitting at ~3.5 Microns," Photonics vol. 10 no. 10, 1164 (2023). Reproduced with permission from MDPI under CC BY 4.0 license. The author is the first author and main contributor of this publication.*

Preface: The goal of this research was to develop a proof-of-principle prototype for the mid-infrared intracavity DFG transmitter making up one half of the transmitter + receiver pair. When designing this experiment, the modelling work built on the foundation of the previous chapter with some notable changes. First, the simplified plane wave cavity model used in the SHG paper was updated to a spatially dependent rate equation

model developed by Risk. This allowed for modelling the effects of the 808 pump beam overlap inside of the gain medium, and was generally more accurate than the plane wave model in predicting the circulating cavity power. Additionally, the SHG coupled wave equations were replaced with those for DFG. One important point is that due to the magnitude of the input signal power at 1550 nm relative to the 1064 nm fundamental power and lower conversion efficiency, the effect of nonlinear depletion was negligible. Several avenues for improving efficiency were discovered and noted in the discussion, mainly centered around improving beam overlap between the 1064 nm and C-band laser in the nonlinear crystal.

This paper was co-authored with Ali Atwi and Tyler Kashak who helped with experimental work and helped edit the manuscript, and Daniel Poitras who provided optical coatings for some of the experimental components. This research article has been published in Photonics.

4.1 Abstract

We report a diode pumped solid state (DPSS) laser used for intracavity pump-enhanced difference frequency generation (DFG) to create a 3.5 micron laser. Using a 50 mm-long periodically poled lithium niobate (PPLN) crystal inside the cavity of an Nd:YVO_4 solid state laser at 1064 nm with 4.5 W pump power at 808 nm, and a 310 mW C-band signal at 1529 nm, up to 31 mW of mid-infrared output power at 3499 nm is obtained. The cavity requires no active stabilization and/or locking, and the entire cavity is <8 cm in length. The obtained output power corresponds to a black box efficiency of 2.20 $\%W^{-1}$, which is the highest value reported to date for continuous wave DFG based on a bulk nonlinear optical crystal with no active stabilization. Potential future applications in free space optical communication are discussed as well.

4.2 Introduction

Free space optical communication has seen a surge in interest, both for terrestrial first and last mile solutions, as well as optical satellite communication [1], [2]. Current efforts have focused on utilizing the short-wave infrared (SWIR) atmospheric transmission window, containing the 1530-1565 nm C-band used in telecommunications. Successful demonstrations utilizing these wavelengths include the SOLISS terminal bidirectional link between the International Space Station (ISS) and an optical ground station at the National Institute of Information and Communications Technology (NICT) in 2019, as well as an inter-satellite

demonstration between the CubeSOTA and ETS9-HICALI satellites in 2019 [3], [4]. However, SWIR communication suffers significantly from scintillation, scattering, and weather effects. The 3-5 μm mid-infrared (MWIR) atmospheric transmission window should offer improved signal to noise ratio and resistance to these adverse effects and could lead to higher link availability and reliability [5], [6]. A previous review from our research group expanded on the benefits of the MWIR band and identified cascade lasers, as well as difference frequency generation (DFG) using nonlinear optical crystals, as the most promising lasers for use in MWIR transmitters [7]–[9]. Cascade lasers offer large modulation bandwidths and can cover the entire MWIR spectrum, but typically operate between 77-250 K, which is inconvenient for many applications [10], [11]. DFG offers room temperature operation and large modulation bandwidths, with potential to achieve up to watt-level continuous wave output power [12]. Typically, OPOs are used due to their resonant structure offering high output powers and tunable output wavelengths. However, the use of DFG allows us to inject a C-band signal beam, offering multi-gigabit per second modulation speeds, which can be faster than directly modulating the OPO pump beam [8]. In this paper, we aim to address the lack of high efficiency intracavity MWIR lasers by presenting a novel DFG laser that uses a simplified linear cavity to reduce the size and sensitivity to alignment, and to achieve high efficiency. The laser is stable while free running with no need for external cavity stabilization or locking. In the cavity, only the pump is resonant, as the signal is coupled into the cavity and the idler is coupled out of the cavity in

a single pass. We see this as the first step to demonstrating a viable high-power mid-infrared source capable of high-speed modulation.

A common metric used to evaluate DFG frequency converters is DFG efficiency, presented according to the formula in equation 4-1:

$$\eta_{\mathrm{DFG}} = 100\% \times \frac{\mathrm{P_{DFG}}}{\mathrm{P_{pump}P_{signal}}} \qquad (4\text{-}1)$$

With the efficiency expressed in units of $\%\mathrm{W}^{-1}$. Here, $\mathrm{P_{DFG}}$ is the output DFG power, $\mathrm{P_{pump}}$ is the input pump power directly before the nonlinear crystal, and $\mathrm{P_{signal}}$ is the input signal power directly before the nonlinear crystal. However, this approach does not consider the efficiencies and coupling losses of the pump and signal sources, which can be important in power limited scenarios where maximizing efficiency is key. So, from a practical application point of view, an interesting metric to compare the efficiency of various DFG structures is the black box efficiency with units of $\%\mathrm{W}^{-1}$, presented here as equation 4-2:

$$\eta_{\mathrm{BB}} = 100\% \times \frac{\eta_{\mathrm{signal}}\eta_{\mathrm{pump}}\mathrm{P_{DFG}}}{\mathrm{P_{pump}P_{signal}}} \qquad (4\text{-}2)$$

where η_{pump} is the diode pumping efficiency for the fiber pump source and η_{signal} is the diode pumping efficiency of the fiber signal source, assuming fiber

lasers are used as pump and signal sources. We mention fiber pump and signal sources specifically as these are commonly used for pumping both DFG and OPO structures. Many of the presented structures in the following section make use of 1064 nm Yb-doped fiber lasers (pumped by 9xx nm diode laser) as pump sources. These have optical-to-optical efficiencies of ~60%, so a value of $\eta_{\text{pump}} = 0.6$ was assumed for these fiber lasers [13]. For devices using direct 1064 nm diode pumping, there is no additional optical conversion step, and so a value of $\eta_{\text{pump}} = 1$ can be used. For the signal fiber, erbium doped fiber amplifiers (EDFAs) are often used. Unfortunately, it is harder to find a standard operating efficiency for the pump diodes in EDFAs, and most authors only include the output power from the EDFA (P_signal). Thus, we've assumed $\eta_{\text{signal}} = 1$ for all EDFAs so that they can be easily compared. This does increase the overall efficiency reported in this paper, so we mention this to avoid claims of inflating the efficiency values intentionally. While we do not claim that our device has the highest DFG efficiency reported, we do claim that it has the highest black box efficiency of the bulk crystal, free-running DFG devices we've reviewed.

In this work, we elected to use the black-box efficiency as the primary metric when benchmarking our device against previously reported wavelength converters. While wall-plug efficiency is ultimately the most critical figure of merit for space-based applications (where total system power consumption is a limiting factor), it is rarely reported in the context of DFG-based converters. In contrast, black-box efficiency

relies on input and output optical powers, which are almost always available in the literature. This made it the most practical choice for enabling consistent comparisons with prior work. Nonetheless, it is important to emphasize that black-box efficiency is not a substitute for wall-plug efficiency in evaluating system-level suitability for space. Moving forward, it would be beneficial if wall-plug efficiency were more widely reported, as this would enable a more direct comparison across different classes of devices and provide a clearer assessment of their potential for space-based deployment.

We performed a literature review of state-of-the-art single pass and intracavity mid-infrared bulk DFG devices. In 2020, Guha et al. reported a single pass DFG configuration, emitting 3.55 W at 3400 nm with 43.3 W 1064 nm via fiber laser pump and 31 W 1550 nm signal via EDFA, corresponding to a DFG efficiency of 0.264 $\%W^{-1}$ and a black box efficiency of 0.159 $\%W^{-1}$ [14]. In 2019, Huang et al. demonstrated 60 mW of DFG power at 3393 nm for 1 W of 1064 nm fiber laser pump and 1 W of 1550 nm, corresponding to a DFG efficiency of 5.8 $\%W^{-1}$ and a black box efficiency of 2.43 $\%W^{-1}$, which accounts for the additional loss of the wavelength division multiplexer used [15]. Huang et al's cavity is also actively stabilized via dither-locking. These devices represent the highest efficiency single pass and intracavity efficiencies we found, respectively, but other devices were reviewed with efficiencies in the same order of magnitude [16]–[20]. These works serve as a representative sample of the state-of-the-art for bulk crystals.

Additionally, waveguides allow for tight confinement of the pump and signal beams over the entire length of the nonlinear medium, which boosts efficiency versus bulk crystals. For example, the highest efficiency mid-infrared waveguide nonlinear frequency converter we found has an internal DFG efficiency of 100 $\%W^{-1}$ and a black box efficiency of 60 $\%W^{-1}$ [21]. However, the reported coupling losses are ~-17 dB for both the pump and signal, which would lower the black box efficiency to less than 1 %/W. Hu et al. demonstrated a high-efficiency coupler that could reduce losses for similar thin-film lithium niobate devices to -0.5 dB [22]. Should this low insertion loss be coupled with a high efficiency waveguide device, it would have much higher efficiency than the bulk crystal devices reviewed above [23], [24]. For now, the main niche for bulk devices is relative cost, ease of manufacturing, and ease of use. Nonlinear waveguide properties are critically dependent on their fabrication quality, as even small imperfections can degrade final performance [25]. So, in the short term, bulk crystals remain easy to source off the shelf with a high level of quality, and linear cavities like the one presented in this manuscript are easy to set up and align. However, as manufacturing continues to improve, waveguide-based mid-infrared sources will be preferable to bulk crystals for many applications. As such, we want to make it clear we limit the novelty claim for our device to bulk crystal devices.

In this work, we implement a hemispherical cavity using Nd:YVO4 as a gain medium to produce a 1064 nm pump. The resonator contains a periodically poled

lithium niobate (PPLN) nonlinear crystal, as well as a dichroic mirror that couples an amplified tunable C-band laser into the cavity. We obtained a black box efficiency of 2.20 %W^(-1), emitting at 3499 nm with 4.5 W 808 nm pump and 310 mW of 1529 nm signal. This device offers the highest black box efficiency for bulk nonlinear crystal frequency converters in a linear cavity without the use of active cavity stabilization. Additionally, our modelling work shows good agreement with experimental results. What follows is a detailed examination of the experimental set-up and a brief review of the theoretical modelling work.

4.3 Materials and Methods

A schematic diagram of the experimental setup is depicted in Fig. 4-1. It consists of a diode-pumped solid-state (DPSS) laser resonator (Nd:YVO4, Dientech) with a PPLN nonlinear crystal inserted into the cavity. The hemispherical resonator was intentionally selected as it allows for a compact cavity set up and is easy to align. Additionally, this linear cavity requires no active stabilization as we've demonstrated experimentally. This reduces complexity and costs without the need for piezoelectric transducers or lock-in amplifiers to facilitate long-term cavity stability. The following cavity parameters were designed with the help of reZonator, an open-source cavity modelling software capable of modelling arbitrary optical systems [26]. The reZonator model is summarized in Figure 4-1 below:

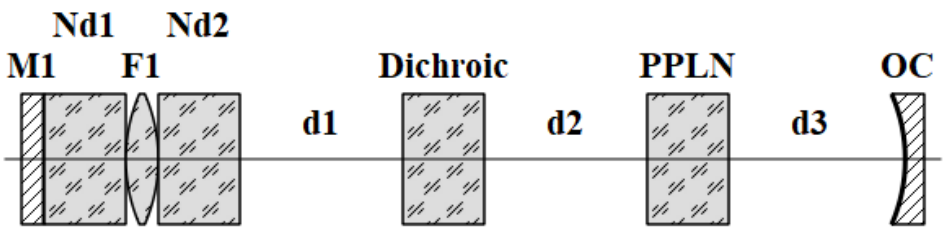

Figure 4-1 Simplified cavity layout as modelled in reZonator. Note that the components are not to scale.

In this model, M1 represents the HR coating at 1064 on the Nd:YVO4. The 5 mm gain medium has been split into two 2.5 mm slabs with refractive index n = 2.16 and a thin lens in the middle, in order to approximate the thermal lens as well. The thermal lens focal length was determined to be ~50 mm, which matched the output beam parameters and output power well, and lines up with similar experimental data [27]. Distances d1, d2, and d3 are 5 mm, 10 mm, and 5 mm, respectively. The dichroic is a 1.8 mm slab with refractive index n = 1.5, while the PPLN is 50 mm with a refractive index of n = 2.2. The OC has a radius of curvature of 100 mm. This results in a 1064 nm pump beam radius in the middle of the PPLN of ~100 μm, which will be used as an input to the nonlinear simulation later.

An 808 nm 125 μm core diameter multimode fiber pigtailed diode laser (AeroDIODE 808LD-2-0-0) emitting up to 4.5 W optical power was imaged onto the Nd:YVO4 gain medium using a GRIN lens (Edmund Optics #64-544). The Nd:YVO4 gain medium was HR coated at 1064 nm (R>99.9%) and high transmission (HT) coated at 808 nm (T>95%) at the input facet, and anti-reflection

(AR) coated at 1064 nm (T>99.8%) at the output facet. This was followed by a dichroic mirror (Custom unit fabricated at National Research Council) with a transmission of 99.3% at 1064 nm and a reflectivity of 70% at 1529 nm, both at an angle of incidence of 45°, for s-polarized light. A 50 mm-long 5mol% MgO doped PPLN crystal (Custom from HCPhotonics) with a period of 30.3 μm was mounted to a copper heat sink with a thermoelectric cooler that can be controlled to within 0.05 °C. The input facet of the PPLN was AR coated for 1064 nm and 1529 nm (T>99.7%) and the output facet was AR coated for 1064 nm (T>99.7%) and 3.5 μm (T>95%). The output coupler (OC) was a CaF2 plano-concave mirror (Custom from Fuzhou Witoptics) with radius of curvature of 100 mm, HR coated for 1064 nm (R=99.85%) and AR coated for ~3.5 μm (T=92%). A 50 mm focal length AR coated CaF plano-convex lens (Thorlabs LA5183-E) was placed after the OC to collimate the divergent 3499 nm light. A thermal power sensor (Thorlabs S401C) was used to measure the DFG power after filtering out the pump and signal with a Germanium (Ge) filter (Thorlabs WH91050-C9). The dichroic mirror was used to couple in a tunable C-band laser (Agilent 8164B) at 1529 nm, which was amplified via a polarization-maintained EDFA (CiviLaser EDFA-C-BA-26-PM). To increase the working distance of the C-band laser, the collimated EDFA output was passed through a 5x beam expander (Thorlabs GBE05-C) followed by a 100 mm focal length plano-convex lens (Thorlabs LA1050-C) to focus the laser into the center of the PPLN. This design was simulated in Zemax which predicted a beam waist radius of 55 μm in the center of the PPLN, ensuring that the confocal focusing

criterion was met. This was required due to space limitations on the optical bench.

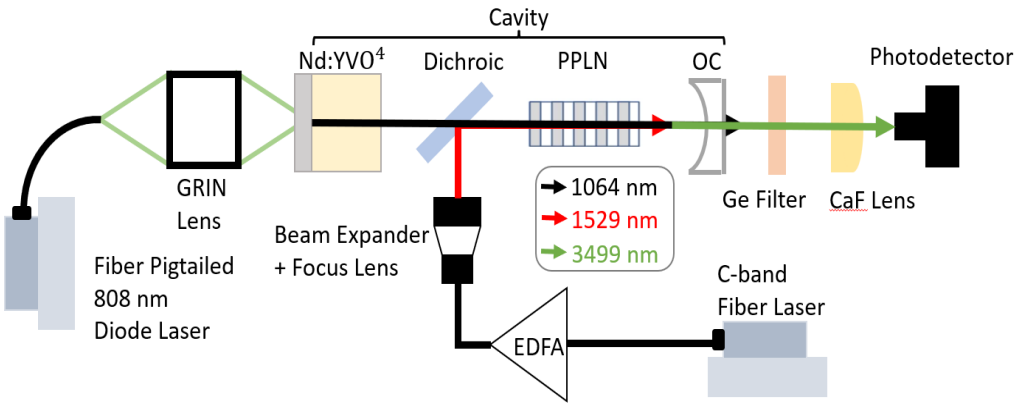

Figure 4-2 Experimental schematic diagram of the intracavity DFG laser. The fibers for the C-band laser and EDFA are polarization maintaining and single mode, and the total cavity length is <8 cm.

A scanning slit beam profiler (Thorlabs BP209IR1) was used to verify the beam diameters. For the C-band laser, the beam profiler was placed at the focus after the beam expander assembly. The distance from the beam profiler and the beam waist matched a Zemax simulation well, with a waist diameter of 110 μm at 10.5 cm from the assembly output. The cavity waist was confirmed by taking several measurements of the gaussian beam diameter outside of the cavity, and then deriving the gaussian waist using the experimental data. The measured waist diameter of 200 μm was close to the predicted value of 190 μm.

We also describe the simulation work presented in the results section. This is a significantly modified version of work our group has presented previously,

although adapted for DFG as opposed to SHG [28]. A flowchart summarizing the flow of the simulation step by step is presented in Fig. 4-3.

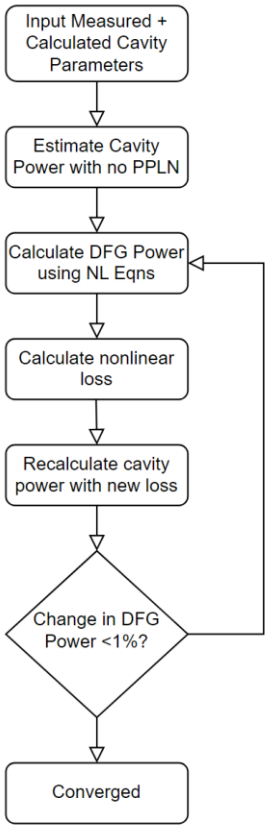

Figure 4-3 A flowchart summarizing the modelling work. Input parameters are experimentally measured where possible, otherwise they are simulated, or use known values from literature.

To start, we must estimate the incident pump and signal power incident on the nonlinear medium. The signal power is measured experimentally before it is coupled into the cavity, while estimating the intracavity 1064 nm pump power is

more involved. A spatially dependent rate equation model was used to derive the intracavity 1064 nm power as detailed by Risk and summarized below in Equation 4-3: [29]

$$F = \frac{1+\frac{B}{fS}\ln(1+fS)}{f\int_0^{\infty}\frac{\exp[-(a^2+1)x]}{1+fS\exp(-a^2x)}}, \tag{4-3}$$

Where $a = \omega_P/\omega_L$ is the ratio of the 808 nm pump and 1064 nm laser beam waists, f is the total Boltzmann factor of the gain medium, $B=(2N_1^0\ \sigma l)/(L+T)$ is the ratio of reabsorption loss to fixed cavity loss with L being the total cavity loss, T is the transmission loss from the output coupler, σ is the emission cross section of the gain medium, l is the length of the gain medium, and N_1^0 is the doping concentration of the Nd in the gain medium. F is a normalized variable proportional to pump power, and S is a normalized variable proportional to internal laser power. Then, by solving for dS/dF, we can derive the pump threshold and slope efficiency in terms of S and F and convert them to real pump power and output laser power as follows.

Once dS/dF has been found numerically, the external slope efficiency of the laser can be found using equation 4-4:

$$\frac{dP_{out}}{dP_P} = \frac{T}{L+T}\frac{v_L}{v_P}\eta_a\frac{dS}{dF}, \tag{4-4}$$

Where ν_L/ν_P is the ratio of frequencies of the lasing and pump light, also known as the quantum defect. η_a is the absorption efficiency of the incident pump photons in the gain medium, and the ratio T/(L+T) is the ratio of laser photons exiting the cavity via the output coupling mirror. We can then solve for the pump threshold of the laser to fully define the expected output power vs pump power curve, as shown in equations 4-5 and 4-6 below:

$$P_{P,th} = \frac{\pi h \nu_p (\omega_L^2 + \omega_P^2)(L+T+2\sigma N_1^0 l)}{4\sigma\tau\eta_a f}, \tag{4-5}$$

$$F_{th} = \frac{(1+a^2)(1+B)}{f}, \tag{4-6}$$

Where τ is the upper manifold lifetime of the gain medium and h is the Planck's constant. Finally, we convert F to P_P by $P_P = \left(\frac{P_{th}}{F_{th}}\right) F$, and we use the derived slope efficiency to determine the expected output power from the laser from the threshold onwards. Then, since the output coupler reflectivity is well known, this allows us to estimate the circulating power within the cavity as well. This determines the input power to the nonlinear medium for the following step of the modelling work.

After determining the input pump and signal power, we use the nonlinear wave equations for DFG to estimate the output idler power as shown in equations 4-7 and 4-8 [30]:

$$\frac{dA_1}{dz} = \frac{2id_{eff}\omega_1^2}{k_1 c^2} A_3 A_2^* e^{i\Delta k z}, \tag{4-7}$$

$$\frac{dA_2}{dz} = \frac{2id_{eff}\omega_2^2}{k_2c^2} A_3 A_1^* e^{i\Delta kz}, \tag{4-8}$$

Where A1 represents the signal wave, A2 represents the idler wave, and A3 represents the pump wave. In this form, we have assumed that the cavity pump power is strong and effectively constant, as the conversion efficiency of the DFG process is low enough that nonlinear losses from conversion are negligible. We still include the nonlinear loss step in Fig. 4-3 as we anticipate the nonlinear loss to become significant in the future once we increase both the pump and signal power, thus increasing the overall efficiency for nonlinear conversion. This increased conversion efficiency acts as an additional source of loss within the cavity, and so must be accounted for to accurately model intracavity frequency conversion at high powers. We temperature tune our PPLN to achieve good phase matching, and the temperature dependence of the PPLN is modelled using the Sellmeier equation for MgO doped PPLN [31]. By using this model, we can accurately predict the output DFG power as a function of input pump power, as well as the temperature dependence of the DFG power via the Sellmeier equation. These results are presented in the following Results section alongside our experimental results, and the two are in good agreement. Future work for expanding the simulation in the future is covered in the Discussion section. Finally, we present our simulation inputs used to generate our results in Table 4-1 below.

Table 4-1 Input parameters to the model. Any value measured experimentally or simulated by the authors is designated by "This work". Cited values are from literature.

Parameter	Value	Ref.
Nonlinear coefficient (d_{33})	27 pm/V	[30]
Nd:YVO_4 length (l)	8 mm	This work
Output Coupler Transmission (T) at 1064 nm	0.15%	This work
Round-trip Losses (L)	3%	This work
Absorption efficiency η_a	99%	This work
Boltzmann Factor (f)	0.6	[32]
Upper manifold lifetime (τ)	90 μs	[33]
Lasing beam radius (ω_L)	190 μm	This work
Pump beam radius (ω_P)	250 μm	This work
Pump beam diameter in PPLN	100 μm	This work
Signal beam diameter in PPLN	55 μm	This work
Nd doping	0.5 at. %	This work
PPLN refractive index	~2.2	[31]

Stimulated emission cross section (σ)	$25 \times 10^{-19}\text{cm}^2$	[34]

4.4 Results

4.4.1 Output Power Testing

Fig. 4-4 shows the leaking 1064 nm power from the laser cavity as a function of the 808 nm optical pump power. The squares represent the experimental data while the solid line represents the predicted leaking power from the simulation. The leaking 1064 nm power was measured with all components in the resonator and the PPLN temperature tuned to minimize nonlinear losses. The simulation used the measured reflectivity and transmission values for intracavity components to generate a total intracavity loss. The measured and simulated power values are in good agreement, implying that the estimated loss and 1064 nm input power for the DFG simulation is accurate.

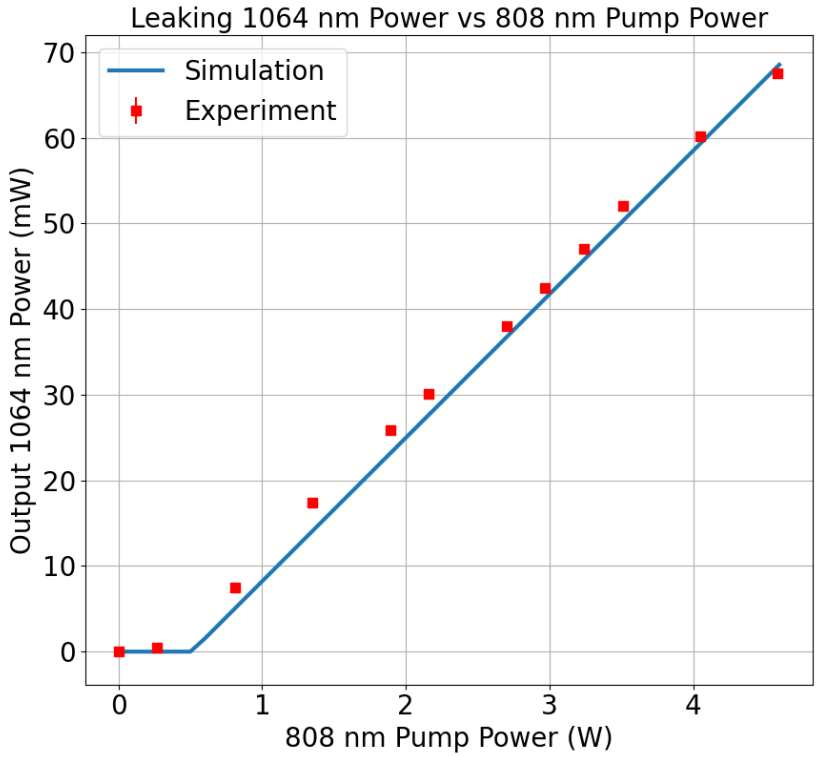

Figure 4-4 Measured and simulated leaking 1064 nm power vs. 808 nm pump power with all devices in the resonator to account for linear losses. Error bars are present but smaller than the data markers.

After collecting the 1064 nm data, the C-band laser was coupled into the PPLN, and DFG power as high as 31 mW at 3499 nm was obtained at a pump power of 4.5 W 808 nm and a C-band power of 310 mW (measured at the output facet of the C-band collimator). This corresponds to a black box efficiency of 2.20 $\%W^{-1}$. The simulated DFG power is compared to the measured experimental results, as shown in Fig. 4-5. The x-axis is the 808 nm optical pump power, and the y-axis is the DFG output power after the Ge filter. The squares represent experimental data while the solid line is the simulated DFG power. The simulation assumes that both input

beams are focused at the center of the PPLN, and the beam diameters and power values are those measured earlier. The trend is in good agreement, with some outliers in the 2-3 W pump range. This discrepancy could be attributed to non-ideal overlap of the 1064 nm and C-band beams, as the hemispherical cavity prevents strong focusing of the 1064 nm beam at the center of the PPLN, and the thermal lens power will change with pump power as well. Nonetheless, the simulated trend can still be used to predict the order of magnitude experimental DFG performance to a reasonable level of accuracy.

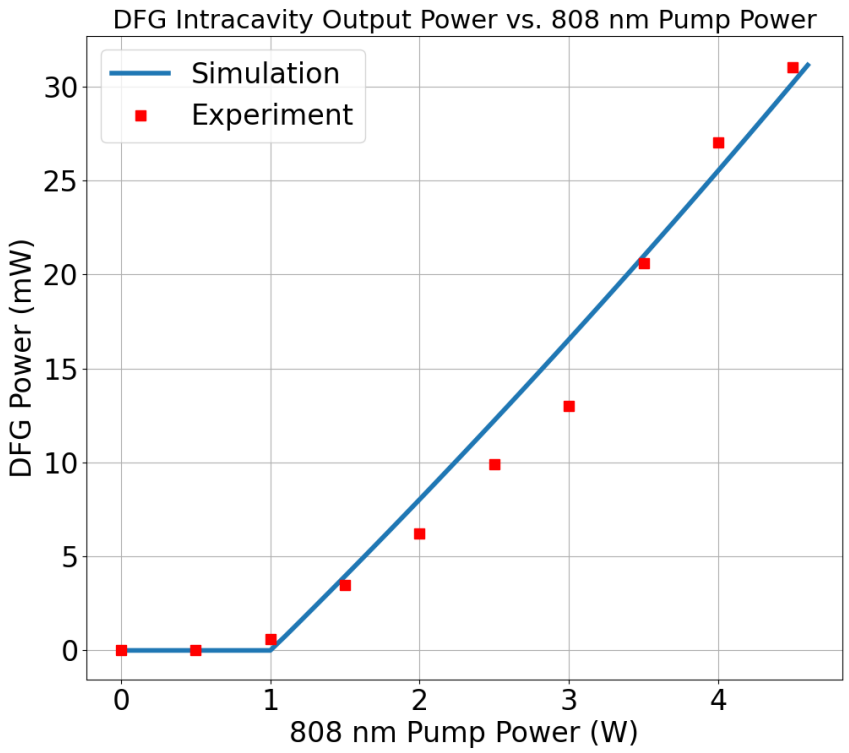

Figure 4-5 Measured and simulated output DFG power vs 808 nm pump power with all losses accounted for. The simulation data is the solid line.

4.4.2 Temperature Testing

To study the temperature tolerance of the DFG laser, the temperature tuning curve of the DFG power was measured. We then simulated the temperature dependence of DFG, using the Sellmeier equation for MgO doped lithium niobate [31]. The results are presented in Fig. 4-6. The x-axis is the temperature of the PPLN, and the y-axis is the normalized DFG power. The squares are experimental data, while the solid line is the simulated curve. The good agreement of the peak power location and full width at half maximum (FWHM) confirms the presence of DFG output. The tail on the left side can be attributed to the theory discussed in sections 2.5.2 and 2.5.3: as we are using a tightly focused gaussian signal beam, we see asymmetry in the tuning curve due to the Guoy phase contribution to the overall phase matching condition. This can also be caused by elliptical focusing, and tilt of the input beams with respect to the optical axis [35]. This was obtained using a standard off-the-shelf thermoelectric cooler, and a machined in-house copper heat sink that also served as the housing for the nonlinear crystal. The FWHM of the main peak is ~6 deg C, demonstrating that the laser can easily be operated at a stable temperature with standard components.

One method of tailoring the temperature response is to modify the grating design of the nonlinear crystal. Compared to uniformly poled devices like those presented here, chirped designs can significantly increase both the temperature and wavelength bandwidth of the conversion process. However, these advantages come at the cost of reduced peak conversion efficiency and greater fabrication

complexity. In contrast, uniform periodically poled structures provide the highest peak efficiency and simplest fabrication process. As such, any potential application must consider the trade-off between maximizing the narrowband efficiency and enabled robust broadband operation. These trade-offs have been explored in the literature if a more in-depth analysis is desired [37], [38].

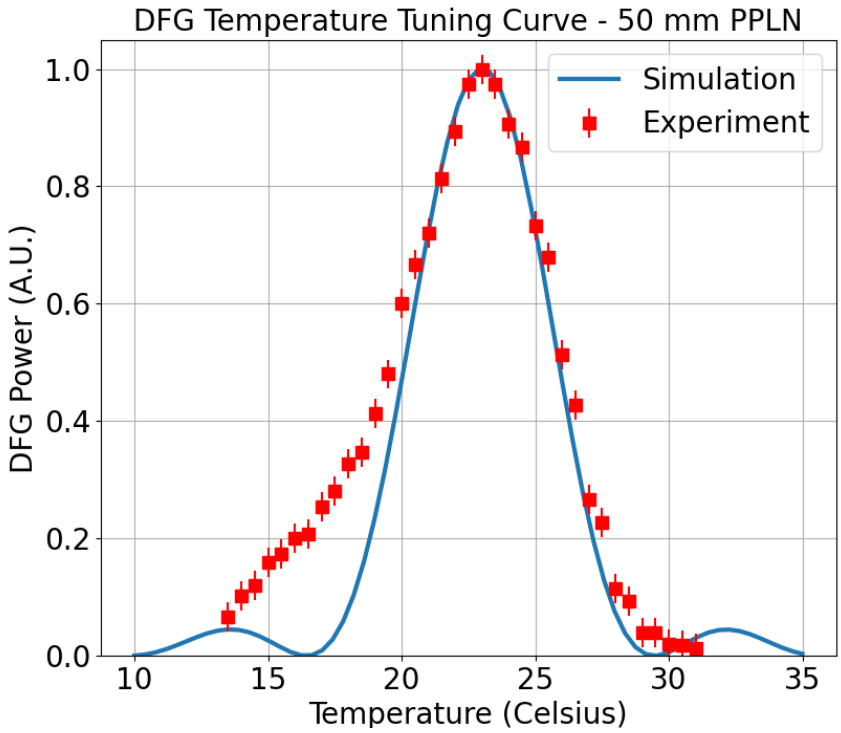

Figure 4-6 Theoretical temperature tuning curve vs measured experimental data.

4.5 Discussion

The results are promising, showing that we can easily achieve state-of-the-art black box efficiency with a compact, linear cavity without stabilization. According to our

modelling, this represents close to the best-case black box efficiency we can reasonably expect for this design. While it is theoretically possible to improve our efficiency to up to ~2.40-2.50 %/W, this was only achieved by further improving the optical coatings, which are already close to the upper limit of performance. A larger efficiency gain would be possible if the pump beam could be made smaller to better overlap with the 55 μm signal beam waist at the center of the PPLN, as there is a noticeable mismatch with the ~100 um pump derived from the cavity simulation. However, this may require a significant cavity redesign, and something other than the hemispherical cavity that we selected due to its simplicity. We will have to investigate in future work whether decreasing the pump beam size is possible, or if increasing the signal beam size is worth the loss in intensity versus the increase in overlap between the pump and signal.

While our model agrees well with the current experimental results, there are several areas where it could be improved to facilitate future work. First, the model does not consider thermal effects outside of the thermal lensing approximated in the cavity simulation. A future test would involve increasing both the pump 808 nm power and the signal C-band power to see if higher output power and black box efficiency can be achieved. However, this will increase the prevalence of thermal lensing in the Nd:YVO4 such that it may affect cavity stability. Additionally, the higher thermal load of a multi-watt level signal coupled with the tens of watts of pump present in the cavity may change the beam properties inside of the nonlinear crystal.

Another important factor is the increased nonlinear losses within the cavity at higher efficiencies and pump powers. Currently, the DFG conversion efficiency is low enough that the nonlinear losses are not significant relative to the linear losses within the cavity (scattering, absorption, non-ideal coatings, etc.). Any attempts to increase efficiency will also increase the prevalence of intracavity nonlinear loss. We have previously demonstrated that in a simple nonlinear process like SHG, the nonlinear loss can significantly affect the expected output power and thermal properties of intracavity frequency conversion at higher efficiencies [28]. We have no reason to believe there won't be similar phenomena to observe at higher device powers and higher efficiencies with intracavity DFG as well. These are important points to consider and investigate in future work, as the efficiency we've reported may not be maintained at higher pump and signal powers as a result.

Future work will focus on adapting the device presented here for free space optical communications. Experiments will include using a 10 W EDFA and 10 W 808 nm pump to push for watt-level DFG power. This is a vital milestone for satellite-to-ground optical communication in low earth orbit, as previous work has identified that 1-2 W CW power is recommended for high link availability and low bit error rates [36]. We will also pursue modulating the C-band source at gigabit speeds, as this opens the door to high-speed weather resistant free space optical links for both last mile applications and longer distance links, due to the combination of high speed and high transmitter power. To the best of our knowledge, a gigabit speed

mid-infrared link has not been demonstrated over distances greater than a few kilometers, so we hope to perform a practical demonstration using drones and high-altitude platforms in the coming months as further proof of principle.

4.6 Conclusions

In conclusion, a compact intracavity DFG MWIR laser with promise for free space communication has been demonstrated. A black box efficiency as high as 2.20 $\%W^{-1}$ has been achieved with a maximum output power of 31 mW for input pump and signal powers of 4.5 W and 310 mW, respectively. The cavity is under 8 cm in length and could be made more compact with professional packaging. The linear cavity requires no active stabilization, which is also a notable benefit. In future work, we expect that this laser will be capable of watt-level output power and provide what may be the first opportunity for a long-distance free space link in the mid-infrared between either a drone or high-altitude platform.

4.7 Patents

This work is a developed version of the transmitter device laid out in the patent US20210141282A1 – Mid-infrared wavelength optical transmitter and receiver.

4.8 Acknowledgements

The authors would like to thank Saju Thomas of MDA (Kanata) and Dr. Atieh of Optiwave Sys-tems Inc. for helpful discussions.

4.9 References

[1] A. Trichili, M. A. Cox, B. S. Ooi, and M.-S. Alouini, "Roadmap to free space optics," *J. Opt. Soc. Am. B, JOSAB*, vol. 37, no. 11, pp. A184–A201, Nov. 2020, doi: 10.1364/JOSAB.399168.

[2] M. M. Abadi, Z. Ghassemlooy, N. Mohan, S. Zvanovec, M. R. Bhatnagar, and R. Hudson, "Implementation and Evaluation of a Gigabit Ethernet FSO Link for 'The Last Metre and Last Mile Access Network,'" in *2019 IEEE International Conference on Communications Workshops (ICC Workshops)*, May 2019, pp. 1–6. doi: 10.1109/ICCW.2019.8757150.

[3] A. Carrasco-Casado *et al.*, "Intersatellite-Link Demonstration Mission between CubeSOTA (LEO CubeSat) and ETS9-HICALI (GEO Satellite)," in *2019 IEEE International Conference on Space Optical Systems and Applications (ICSOS)*, Oct. 2019, pp. 1–5. doi: 10.1109/ICSOS45490.2019.8978975.

[4] K. Iwamoto *et al.*, "Experimental results on in-orbit technology demonstration of SOLISS," in *Free-Space Laser Communications XXXIII*, SPIE, Mar. 2021, pp. 51–57. doi: 10.1117/12.2578089.

[5] E. Leitgeb *et al.*, "Analysis and evaluation of optimum wavelengths for free-space optical transceivers," in *2010 12th International Conference on Transparent Optical Networks*, Jun. 2010, pp. 1–7. doi: 10.1109/ICTON.2010.5549009.

[6] M. A. Khalighi and M. Uysal, "Survey on Free Space Optical Communication: A Communication Theory Perspective," *IEEE Communications Surveys & Tutorials*, vol. 16, no. 4, pp. 2231–2258, 2014, doi: 10.1109/COMST.2014.2329501.

[7] L. Flannigan, L. Yoell, and C. Xu, "Mid-wave and long-wave infrared transmitters and detectors for optical satellite communications—a review," *J. Opt.*, vol. 24, no. 4, p. 043002, Mar. 2022, doi: 10.1088/2040-8986/ac56b6.

[8] N. S. Prasad, "Optical Communications in the mid-wave IR spectral band," in *Free-Space Laser Communications: Principles and Advances*, A. K. Majumdar and J. C. Ricklin, Eds., in

Optical and Fiber Communications Reports. , New York, NY: Springer, 2008, pp. 347–391. doi: 10.1007/978-0-387-28677-8_8.

[9] F. Grillot *et al.*, "Recent advances in high-speed data communications using mid-infrared quantum cascade lasers," in *Novel In-Plane Semiconductor Lasers XXII*, SPIE, Mar. 2023, pp. 97–102. doi: 10.1117/12.2651132.

[10] B. Hinkov, A. Hugi, M. Beck, and J. Faist, "Rf-modulation of mid-infrared distributed feedback quantum cascade lasers," *Opt. Express, OE*, vol. 24, no. 4, pp. 3294–3312, Feb. 2016, doi: 10.1364/OE.24.003294.

[11] A. Calvar *et al.*, "High frequency modulation of mid-infrared quantum cascade lasers embedded into microstrip line," *Applied Physics Letters*, vol. 102, no. 18, p. 181114, May 2013, doi: 10.1063/1.4804370.

[12] C. Xi, P. Wang, X. Li, and Z. Liu, "Highly efficient continuous-wave mid-infrared generation based on intracavity difference frequency mixing," *High Power Laser Science and Engineering*, vol. 7, p. e67, Jan. 2019, doi: 10.1017/hpl.2019.45.

[13] S. Unger, A. Schwuchow, S. Jetschke, V. Reichel, A. Scheffel, and J. Kirchhof, "Optical properties of Yb-doped laser fibers in dependence on codopants and preparation conditions," in *Optical Components and Materials V*, SPIE, Feb. 2008, pp. 270–280. doi: 10.1117/12.762967.

[14] S. Guha, J. O. Barnes, and L. P. Gonzalez, "Multiwatt-level continuous-wave midwave infrared generation using difference frequency mixing in periodically poled MgO-doped lithium niobate," *Opt. Lett., OL*, vol. 39, no. 17, pp. 5018–5021, Sep. 2014, doi: 10.1364/OL.39.005018.

[15] K. Huang *et al.*, "Observation of spectral mode splitting in a pump-enhanced ring cavity for mid-infrared generation," *Opt. Express, OE*, vol. 27, no. 8, pp. 11766–11775, Apr. 2019, doi: 10.1364/OE.27.011766.

[16] Q. Hao *et al.*, "Mid-infrared transmitter and receiver modules for free-space optical communication," *Appl. Opt., AO*, vol. 56, no. 8, pp. 2260–2264, Mar. 2017, doi:

10.1364/AO.56.002260.

[17] Y. Su *et al.*, "10 Gbps DPSK transmission over free-space link in the mid-infrared," *Opt. Express, OE*, vol. 26, no. 26, pp. 34515–34528, Dec. 2018, doi: 10.1364/OE.26.034515.

[18] A. C. Gray, S. A. Berry, L. G. Carpenter, J. C. Gates, C. B. E. Gawith, and P. G. R. Smith, "Upconversion detection of 1.25 Gb/s mid-infrared telecommunications using a silicon avalanche photodiode," *Opt. Express, OE*, vol. 28, no. 23, pp. 34279–34289, Nov. 2020, doi: 10.1364/OE.404855.

[19] M. F. Witinski, J. B. Paul, and J. G. Anderson, "Pump-enhanced difference-frequency generation at 3.3 μm," *Appl. Opt., AO*, vol. 48, no. 13, pp. 2600–2606, May 2009, doi: 10.1364/AO.48.002600.

[20] K. Wang, X. Li, P. Wang, W. Hua, Z. Wang, and K. Han, "Broadband, Continuous-Wave, Mid-Infrared Generation Based on ASE Fiber Source," *Photonics*, vol. 9, no. 10, Art. no. 10, Oct. 2022, doi: 10.3390/photonics9100724.

[21] J. Mishra *et al.*, "Mid-infrared nonlinear optics in thin-film lithium niobate on sapphire," *Optica, OPTICA*, vol. 8, no. 6, pp. 921–924, Jun. 2021, doi: 10.1364/OPTICA.427428.

[22] C. Hu *et al.*, "High-efficient coupler for thin-film lithium niobate waveguide devices," *Opt. Express, OE*, vol. 29, no. 4, pp. 5397–5406, Feb. 2021, doi: 10.1364/OE.416492.

[23] L. Ledezma *et al.*, "Octave-spanning tunable infrared parametric oscillators in nanophotonics," *Science Advances*, vol. 9, no. 30, p. eadf9711, Jul. 2023, doi: 10.1126/sciadv.adf9711.

[24] A. Y. Hwang *et al.*, "Mid-infrared spectroscopy with a broadly tunable thin-film lithium niobate optical parametric oscillator." arXiv, Jul. 09, 2023. doi: 10.48550/arXiv.2307.04199.

[25] M. Santandrea, M. Stefszky, V. Ansari, and C. Silberhorn, "Fabrication limits of waveguides in nonlinear crystals and their impact on quantum optics applications," *New J. Phys.*, vol. 21, no. 3, p. 033038, Mar. 2019, doi: 10.1088/1367-2630/aaff13.

[26] N. I. Chunosov, "reZonator." Accessed: Jun. 06, 2023. [Online]. Available: http://rezonator.orion-project.org/

[27] “Detailed study of thermal lensing in Nd:YVO/sub 4/ under intense diode end-pumping.” Accessed: Sep. 25, 2023. [Online]. Available: https://ieeexplore.ieee.org/document/947669/

[28] L. Flannigan, T. Kashak, and C.-Q. Xu, “Study of fundamental wave depletion in intracavity second harmonic generation,” *Opt. Express, OE*, vol. 29, no. 5, pp. 6810–6823, Mar. 2021, doi: 10.1364/OE.417191.

[29] W. P. Risk, “Modeling of longitudinally pumped solid-state lasers exhibiting reabsorption losses,” *J. Opt. Soc. Am. B, JOSAB*, vol. 5, no. 7, pp. 1412–1423, Jul. 1988, doi: 10.1364/JOSAB.5.001412.

[30] R. Boyd, *Nonlinear Optics*, 4th ed. Academic Press. Accessed: Sep. 26, 2023. [Online]. Available: https://shop.elsevier.com/books/nonlinear-optics/boyd/978-0-12-811002-7

[31] O. Gayer, Z. Sacks, E. Galun, and A. Arie, “Temperature and wavelength dependent refractive index equations for MgO-doped congruent and stoichiometric LiNbO3,” *Appl. Phys. B*, vol. 91, no. 2, pp. 343–348, May 2008, doi: 10.1007/s00340-008-2998-2.

[32] Y. Bai, “Pumping wavelength related population inversion in Nd:doped laser,” *AIP Advances*, vol. 10, no. 10, p. 105309, Oct. 2020, doi: 10.1063/5.0006436.

[33] L. Fornasiero, S. Kück, T. Jensen, G. Huber, and B. H. T. Chai, “Excited state absorption and stimulated emission of Nd3+ in crystals. Part 2: YVO4, GdVO4, and Sr5(PO4)3F,” *Appl Phys B*, vol. 67, no. 5, pp. 549–553, Nov. 1998, doi: 10.1007/s003400050543.

[34] Y.-F. Chen and Y. P. Lan, “Comparison between c-cut and a-cut Nd:YVO4 lasers passively Q-switched with a Cr4+:YAG saturable absorber,” *Appl Phys B*, vol. 74, no. 4, pp. 415–418, Apr. 2002, doi: 10.1007/s003400200814.

[35] T. W. Tukker, C. Otto, and J. Greve, “Elliptical-focusing effect on parametric oscillation and downconversion,” *J. Opt. Soc. Am. B, JOSAB*, vol. 15, no. 9, pp. 2455–2461, Sep. 1998, doi: 10.1364/JOSAB.15.002455.

[36] S. Gagnon, B. Sylvestre, L. Gagnon, A. Koujelev, D. Gratton, and S. Hranilovic, “Recent developments in satellite laser communications: Canadian context,” in *International Conference on Space Optical Systems and Applications (ICSOS)*, Corsica, France, Oct. 2012,

pp. 1–8.

[37] M.M. Fejer, G. A. Magel, D. H. Jundt, and R. L. Byer, "Quasi-phase-matched second harmonic generation: tuning and tolerances," *IEEE J. Quantum Electronics,* vol. 28, no. 11, pp.2631-2654, Nov. 1992, doi: 10.1109/3.161322

[38] M. Charbonneau-Lefort, B. Afeyan, and M.M. Fejer, "Optical parametric amplifiers using chirped quasi-phase-matching gratings I: practical design formulas," *J. Opt. Soc. Am. B, JOSAB,* vol. 25, no. 4, pp .463-480, Mar. 2008.

Chapter 5. Compact Intracavity Mid-infrared Upconversion Detector – A Systematic Study

This chapter is reproduced from a journal article T. Kashak, ***L.Flannigan,*** *A. Atwi, Daniel Poitras, and C.Q. Xu, "Compact Intracavity Mid-Infrared Upconversion Detector – A Systematic Study," Opt. Continuum 3, 1660-1678 (2024). Reproduced with permission from Optica under BOIA open access agreement. The author is a shared first author and contributed significant work to this publication.*

Preface: The goal of this research was to develop a proof-of-principle prototype for the mid-infrared intracavity SFG receiver. This paper represents the most up-to-date modelling work. The new model keeps the spatially dependent rate equation from the prior chapter while updating the nonlinear wave equation model to include the overlap integral. Derived by Boyd and Kleinman in their 1968 paper for SHG and later generalized to other three-wave mixing processes, the overlap integral allows us to account for the gaussian shape and complicated efficiency dependence on the overlap between the two input beams for DFG and

SFG. This revealed further optimization work that could be performed in the future by re-designing the cavity to better optimize the focus parameter of the fundamental 1064 nm wave. It also allowed for modelling the temperature tuning curve "tail" seen in prior work, which can be caused by beam tilt, ellipticity, and tight focusing which cannot be modelled by the old plane wave approach. The modelling work is the most accurate to date and matched the experimental data well, and also led to future improvements mentioned in the Chapter 6 conclusion. This represented the completion of prototypes for both the transmitter + receiver, allowing high-speed communication experiments to begin with National Research Council partner Ross Cheriton's help.

This paper was co-authored by Tyler Kashak, a shared first author who contributed significantly to the experimental design and fabrication of the nonlinear crystals used in the experiment. Ali Atwi helped with experimental work and editing the manuscript, and Daniel Poitras who provided optical coatings for some of the experimental components. This research article has been published in Optics Continuum.

5.1 Abstract

Mid-IR light detection based on intracavity upconversion using a compact structure has been studied both experimentally and theoretically. The mid-IR detector consists of a 47.5 mm MgO doped periodically poled lithium niobate crystal placed in a resonant cavity of a 1064 nm diode-pumped Nd:YVO_4 laser to enhance efficiency. The generated 1064 nm light is mixed with a mid-infrared source emitting at 3469 nm using an intracavity dichroic mirror. This produces short wave infrared 814.2 nm light via sum frequency generation (SFG). The upconverted light overlaps with the high responsivity for commercial off-the-shelf silicon photodetectors, enabling high speed and high sensitivity detection, surpassing direct mid-infrared detection. The lowest power detected was 150 nW, and the theoretical noise equivalent power for state-of-the-art Si detectors is $1.7 \cdot \mathrm{fW}/\sqrt{\mathrm{Hz}}$. The free running cavity requires no active stabilization, and the total packaged prototype size is 3.75x3.0x8.0 cm, which is relatively compact. An experimental power conversion efficiency up to 36.0% is observed, which agrees well with theoretical simulations. A systematic theoretical study is performed to investigate potential for further optimization of the device.

5.2 Introduction

Optical free space communication has benefitted from rapid development and an increase in interest from the broader scientific community in recent years. It is

clear to see why, given the benefits of optical carriers over radio: larger bandwidths, higher link security, smaller size, weight and power (SWaP) for transmitters and receivers, and lighter regulatory burden [1]. Most current efforts focus on using the short-wave infrared (SWIR), specifically the C-band (1525-1565 nm), for long distance links. This is in large part due to the availability of mature off-the-shelf sources and detectors with high speed and sensitivity due to advances in fiber telecommunications. While the SWIR will no doubt serve as the backbone of free space optical communication, it is not without problems. Atmospheric effects such as scattering and turbulence/scintillation, as well as weather including fog and haze can greatly reduce link availability. One potential mitigation technique is to move to longer wavelengths that still fall within one of the atmospheric transmission windows. A promising candidate is the mid infrared (mid-IR, 3-5 microns) which greatly reduces scattering and scintillation, and can relax requirements for adaptive optics over long distances [2,3].

One of the major challenges posed by switching to the mid-IR for atmospheric mitigation is the lack of detectors with sufficient speed and sensitivity for long distance communications. Current commercial solutions tend to fall into either of two categories. The first is thermal detectors making use of microbolometers, which can be made relatively cheap. However, these detectors must often trade sensitivity for response time, while high speed optical communication often requires both to be maximized. The other category is small bandgap semiconductor materials, such

as HgCdTe or InSb. These are commercially available and tend to have much higher bandwidths than thermal detectors. However, the small bandgap leads to high dark currents due to thermal noise that typically require cooling to mitigate. While in some instances Peltier coolers are sufficient for the application, peak performance often requires cryogenic cooling, while SWIR detectors operate well at room temperature by default [4]. Even with this cooling, direct mid-infrared detection is several orders of magnitude below comparable SWIR detectors in terms of detectivity. Detectivity is an important figure of merit classifying the overall performance of a detector and is defined as the inverse of the noise-equivalent power normalized per square root of the sensor's area and frequency bandwidth, with units of Jones ($\mathrm{cm} \cdot \sqrt{\mathrm{Hz}}/\mathrm{W}$). It is a method of directly comparing detectors while controlling for variables that affect detector performance such as active area and the signal frequency. Typical values for state-of-the-art direct SWIR detectors are $10^{13} - 10^{14}$ Jones, while direct mid-infrared detectors have detectivities of $10^{10} - 10^{11}$ Jones [3,5,6].

Mid-infrared upconversion using nonlinear optics stands as an established method of overcoming these limitations. By mixing an intense pump beam with a mid-infrared idler beam inside a nonlinear crystal, the mid-infrared idler can be upconverted to wavelengths in the 700-900 nm range while maintaining the spatial and spectral content of the signal [7]. This coincides with high responsivity silicon detectors which offer lower noise, higher speed, and the potential for room

temperature operation over both short bandgap semiconductors as well as InGaAs detectors used in the C-band [5,8]. Before discussing the state-of-the-art for mid-IR upconversion, it is necessary to clarify some important terminology. Throughout this work, there are many references to power conversion efficiency and quantum efficiency (QE). Power conversion efficiency is derived from taking the output upconverted signal power just after the output crystal facet and dividing it by input mid-infrared idler power just before the nonlinear crystal facet:

$$\mathrm{PE} = \frac{\mathrm{P_s}}{\mathrm{P_i}} \tag{5-1}$$

This is a useful metric for how efficient the overall nonlinear process is. Another important metric for certain applications like imaging and quantum communications is the quantum efficiency. When referring to quantum efficiency, the experimental efficiency can be retrieved from the power conversion efficiency (Eq. 5-1) by multiplying by the ratio between the signal and idler wavelengths, converting it to a photon ratio, which is the definition of quantum efficiency:

$$\mathrm{QE} = \frac{\mathrm{P_s}}{\mathrm{P_i}}\frac{\lambda_\mathrm{s}}{\lambda_\mathrm{i}} \tag{5-2}$$

Therefore, by Equations 5-1 and 5-2, we end up with our device's power efficiency

of 36% and a quantum efficiency of ~8.5%. There is also a useful formula for the theoretical maximum quantum efficiency derived by Dam et al, who currently hold the intracavity QE record of 20% [9,10]:

$$QE_{max} = \frac{16\pi d_{eff}^2 l^2 P_{Gauss}}{n_1 n_2 n_3 \epsilon_0 c \lambda_1 \lambda_3 w_0^2} \tag{5-3}$$

Where *l* is the length of the nonlinear crystal, P_{Gauss} is the circulating pump power of Gaussian beam in the cavity, d_{eff} is the effective nonlinear coefficient of the nonlinear medium, n_i is the refractive index of the PPLN for the indicated beam, λ_n is the wavelength for the indicated beam, and w_0 is the beam radius of the pump beam in the center of the PPLN. The main limitation of this formula is that it was derived assuming the pump and idler beams are defocused inside of the nonlinear medium to the point that they can be approximated as plane waves. For devices making use of tightly focused gaussian beams, such as ours, this formula is not applicable. It will still serve as a useful formula for suitable devices in the literature, since it estimates the upper limit of quantum efficiency achievable for a certain pump power and upconversion wavelength.

Now that we have clarified the efficiency terms, we can discuss the state of the art for upconversion detectors. This technology is already well established in the SWIR, with upconversion quantum efficiencies >90% used in imaging and single

photon counting applications [8,11–14]. Experimentally demonstrated quantum efficiencies for mid-infrared upconversion tend to be lower than the SWIR. This is due to the inherent efficiency loss from converting longer wavelengths and therefore lower energy photons into higher energy ones, as can be seen by the inverse wavelength dependence in Eq. 5-2 and 5-3. This is also due to the difficulty of sourcing high quality mid-IR optics and coatings relative to the SWIR. Another consideration is that for wavelengths longer than 3.6 microns, higher absorption in the mid-infrared in PPLN is to blame. PPLN is often used due to its broad transmission spectrum, but it exhibits increasing absorption past 3.6 microns that limits conversion efficiencies significantly [7,15,16].

There have been a number of interesting developments in the state of the art for mid-infrared upconversion over the last two decades. Starting with bulk crystal intracavity continuous wave devices, much work has been performed by Ajanta Barh, Rasmus Pedersen, Peter Tidemand-Lichtenberg, and Jeppe Dam. As mentioned previously, Dam et al. holds the record for a CW intracavity bulk crystal upconversion detector with a quantum efficiency of 20% [10,17]. Pedersen et al. and Barh. et al. have iterated on this work, deriving thermal noise equivalent power for mid-IR upconversion and demonstrating ultra-broadband mid-IR upconversion using fanned grating PPLN crystals and non-collinear phase matching [7,9,16,18–20]. While this is the experimental record for intracavity bulk crystal devices, higher quantum efficiencies have been demonstrated in the

mid-IR using pulsed sources, PPLN waveguides, and high pump power single-pass schemes.

Hogstedt et al. demonstrated a pulsed mid-IR upconversion detector with a signal-to-noise ratio 500 times higher than that of a cryogenically cooled InSb detector, due to the large reduction in dark current from using a Si-based detector [21]. In 2007, Imaki and Kobayashi demonstrated a pulsed upconversion setup with 40% QE, in 2013 Gu et al. achieved 64% QE efficiency using a pulsed setup, and in 2017 Wolf et al. demonstrated up to 82% QE efficiency using very high energy pulses [22–24]. A recent development in April 2024 was quantum entanglement and interference demonstrated at 3 microns by Ge et al [25]. Using a single-pass upconversion scheme in PPLN with 45 W pumping power, they demonstrated 37.9% QE, which is the current record for bulk continuous wave PPLN to the best of our knowledge.

Literature on mid-IR waveguide upconverters is harder to find. This is due to the fact that, until recently, it was difficult to manufacture lithium niobate waveguides with low losses at wavelengths <2.0 μm, preventing efficient upconversion [26–29]. To the best of our knowledge the current state of the art is 85%/W internal SFG efficiency with a pump power of 0.192 W using a PPLN ridge waveguide by Lehmann et al [30]. This corresponds to a QE of 16% derived from values in the paper. This demonstrates that the QE of waveguides can be higher than bulk for much lower pump powers, given the pump powers in the bulk

demonstrations are typically tens of watts. All of these structures have applications in mid-infrared imaging, military countermeasures, spectroscopy, remote sensing, gas detection, and free space optical communication, making upconversion a versatile option with a demonstrated record of performance in the literature [3,20,31–34].

In this paper, we aim to fill a gap in the literature identified above. While the general operating principles of upconversion detection are understood, a systematic study utilizing focused gaussian beams has not been presented recently. We present a systematic study on mid-infrared upconversion based on quasi phase matched PPLN in a compact intracavity structure both experimentally and theoretically using tightly focused gaussian beams. We utilize the thermal lens generated by high power pumping of a Nd:YVO_4 gain medium to achieve a smaller beam radius in the nonlinear crystal, while making use of a longer nonlinear crystal to maximize conversion efficiency. The 1064 nm light emitted by the Nd:YVO_4 is confined in a cavity and mixed with 3469 nm mid-IR light generated via difference frequency generation using a previously reported laser from our research group [35]. This generates upconverted light at 814.2 nm, and we achieved 9.5 mW of 814.2 nm light for 26.3 mW of 3469 nm mid-IR light. As such, we report a measured upconversion efficiency of 36% and a calculated quantum efficiency of 8.5%. The lowest optical power measured was 150 nW of DFG which corresponded to 53 nW of SFG power, limited by the detection circuit. A theoretical calculation of the

noise-equivalent power limit shows a possible floor of $\sim 1.7 \cdot f\mathrm{W}/\sqrt{\mathrm{Hz}}$, enabling single photon counting applications. It is worth noting that mixing 1064 nm and 3.5 microns is not the only way to generate light suitable for silicon detectors. Another approach would be to mix 808 nm and 3.5 microns to generate visible wavelengths around 650-660 nm. We simply adopted the 1064 nm approach as Nd:YVO_4 is a medium that our research group has significant experience with, and building a compact resonant cavity for the 1064 nm light is straightforward with commercially available parts.

While our device does not currently surpass the previous state of the art currently in terms of efficiency, it is quite compact at 3.75x3x8 cm which is important for free space communication, remote sensing, and other relevant applications. Additionally, we show through detailed theoretical analysis that if certain optimizations are made, it is possible for the device to meet and even exceed the performance bar set by Dam et al. for significantly lower circulating powers inside of the cavity thanks to the focusing of the beams in the PPLN coupled with higher pump powers. We hope that this study will serve as a useful reference point for those looking to create high efficiency mid-infrared upconversion detectors in the future through a solid fundamental understanding of the operating principles.

Following this Introduction, we present in the Methods section the experimental set-up, the cavity design and optimization, the cavity and upconversion simulation work, and the theory for beam overlap. In the Results section, we present the leaking

1064 nm and SFG output power dependence on pump power, show the potential optimization work to be done with the beam overlap, characterize the linearity of the SFG response, measure the stability of the output SFG light, measure the conversion efficiency for various lengths of nonlinear crystal, and determine the temperature response of the upconversion process. In the Discussion section, we calculate the theoretical noise equivalent power for a state-of-the-art silicon detector and discuss the potential optimizations and future work identified in the results section from the experimental and theoretical results.

5.3 Methods

A schematic diagram of the SFG intracavity setup is shown in Fig. 5-1.

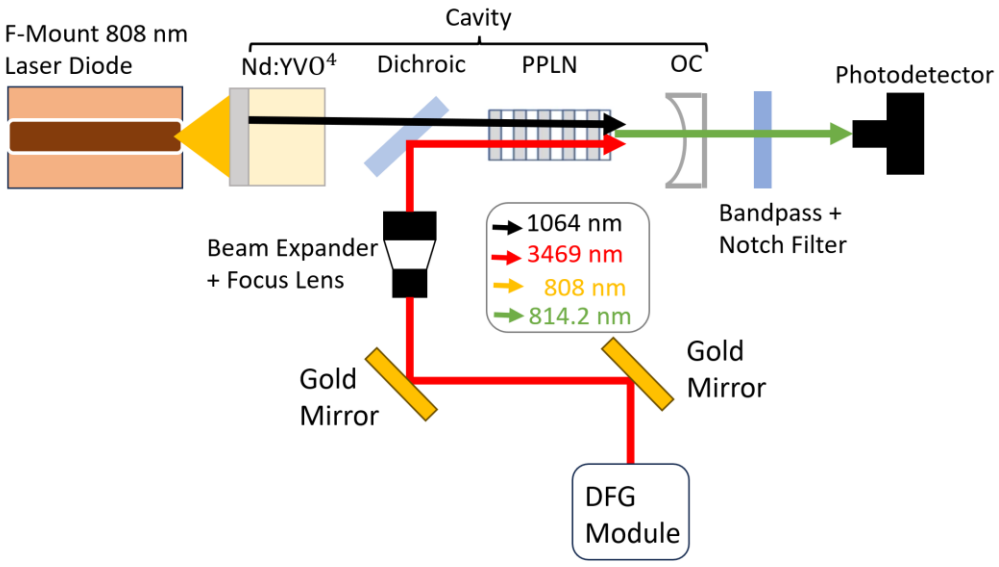

Figure 5-1 Experimental schematic diagram of the intracavity SFG laser. The DFG module is

described in a previous manuscript from our research group [35].

The setup consists of an 808 nm F-mount diode that is linearly polarized, has an integrated fast-axis collimator, and is capable of up to 10W output power (Focuslight FL0FM01-10-808-Y). This was followed by an Nd:YVO_4 gain medium where the facet facing the 808 LD was coated for high reflection at 1064 nm (R>99.9%) and high transmission at 808 nm (T>95%), while the output facet had an anti-reflection coating for 1064 nm (T>99.8%). A dichroic mirror was used to couple mid-infrared light into the cavity. This mirror was a custom unit fabricated at the National Research Council: it was a 1.8-mm thick N-BK7 substrate coated on both surfaces with high transmission at 1064 nm (R~99.4%), high reflectivity in the mid-infrared (R>82.4%), and high reflectivity at 808 nm (R>99.9%) to help reduce leaking 808 nm light. These values were valid only for an angle of incidence of 45° and for s-polarized light. To confirm the filters removed leaking 808 nm light, the output was measured via optical spectrum analyzer down to the nanowatt level. There was no signal at or around 808 nm, and the only signal present was the 814.2 nm light from the upconversion process. The mid-infrared light was generated by a DFG module previously described by our research group [35]. It was coupled into the cavity via two gold-coated mirrors (Thorlabs PF05-03-M01) in a Z-fold configuration, then passed through a 2X beam expander (Thorlabs LA5763-E, LA5817-E) and focusing lens (Thorlabs LA5042-E) in order to achieve the desired focus in the center of the nonlinear crystal. In the future, this setup will

be replaced by an appropriate fiber collimator and focusing lens to make the signal arm of the setup more compact.

The nonlinear crystal was a 47.5 mm long periodically-poled 5% MgO-doped lithium niobate crystal (MgO:PPLN) with a period of 22.75 μm that was fabricated in-house by our group. The MgO:PPLN was coated on both facets with an AR coating at 1064 nm (T>99.8%) and at 3369 nm (T>95%), while the output facet was also coated for high transmission at the SFG wavelength of 814.2 nm (T>99%). The MgO:PPLN was mounted to a copper heatsink via thermal compound and temperature controlled via a thermoelectric cooler (TEC) to an accuracy of 0.05 °C. The output coupling mirror (OC) was a custom unit on a Calcium Fluoride substrate that was 6 mm in diameter and had a high reflectivity coating at 1064 nm (R>99.85%) and high transmission at the SFG wavelength (T>99.9%). Residual 1064 nm and 3469 nm light was filtered after the OC using a bandpass filter centered at 820 nm with 10 nm FWHM (Thorlabs FBH820-10) and a 1064 nm notch filter (Thorlabs NF1064-44). Measurements above 0.01 mW were captured using a Thorlabs S401C thermal power meter, while measurements below this value were captured using a Thorlabs PDA36A2 variable gain Si detector. The cavity was <8 cm in length measured from the Nd:YVO_4 HR coating to the OC.

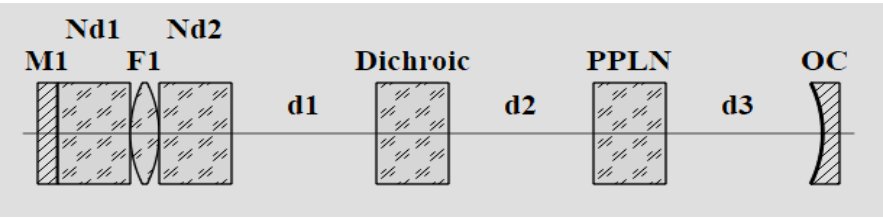

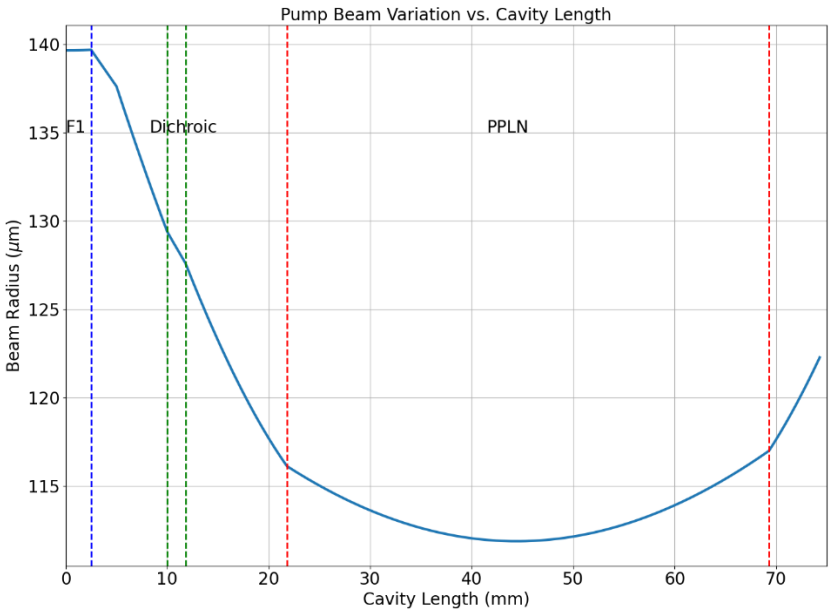

Figure 5-2 A block diagram of the cavity model (upper) and a plot of the 1064 nm pump beam radius as it evolves through the cavity left to right (lower). The distance is measured relative to the plane cavity mirror M1.

A hemispherical cavity was selected due to its relative simplicity and ease of alignment. In order to optimize the pump beam distribution inside of the PPLN, a cavity model was set up using the open-source ReZonator software [36]. This software implements ABCD matrix methods for cavity mode simulations in standing wave and ring resonators. A block diagram of the cavity and a plot of the pump beam evolution inside of the cavity can be seen in Fig. 5-2. The cavity consists of a plane mirror representing the HR coating of the Nd:YVO_4 (M1) immediately followed by the 5 mm long Nd:YVO_4. To model the effect of thermal lensing, a thin lens F1 is inserted in the middle of the Nd:YVO_4 sample and a

thermal lens of 75 mm was found to match the experimental results well, and is in line with prior characterizations of thermal lensing effects in Nd:YVO_4 [37]. The thermal lens is important as it allows us to attain a smaller beam radius in the PPLN for the pump, which increases the efficiency due to the higher intensity. Following the Nd:YVO_4 is a 5 mm gap (d1) and then a 1.8 mm thick plate of N-BK7 representing the dichroic mirror. This is followed by a 10 mm gap (d2) and a 47.5 mm slab of material representing the PPLN. The final gap of 5 mm (d3) leads into the output coupler for the cavity with a radius of curvature of 100 mm (OC). In the beam radius plot, the vertical dashed lines represent the location of the thermal lens (blue), the dichroic facets (green), and the PPLN facets (red). A beam radius of ~110 μm is obtained in the center of the PPLN with a symmetric Gaussian profile. The focus for the mid-IR beam in the center of the PPLN was found to be 55 μm.

In order to simulate the expected SFG output power, we first simulated the cavity to estimate the circulating intracavity power, and then used the nonlinear wave equations for SFG to estimate the output power without accounting for beam overlap. This allows us to account for the nonlinear conversion process, which is an additional source of loss within the cavity. Once the SFG power was estimated, a nonlinear loss was calculated and the intracavity simulation was run again. This updates the circulating intracavity power which was then used to generate a new SFG power estimate. This process repeated until the SFG power and intracavity power converged, i.e. the change between iterations was negligible. In this case, the nonlinear loss ends up being negligible as the depletion was negligible, due to the

pump intensity being many orders of magnitude higher than both the signal and SFG intensities. Should the signal and SFG intensity approach that of the pump, depletion and thus the nonlinear loss would become noticeable. The cavity simulation is the same as the one presented in our previous work for a DFG intracavity source using a spatially dependent rate equation from Risk, omitted here for brevity [35,38]. The nonlinear wave equations are the same as those presented by Boyd [39]:

$$\frac{dA_1}{dz} = \frac{2i\omega_1 d_{eff}}{k_1 c^2} A_2^* A_3 e^{-i\Delta kz} \tag{5-4}$$

$$\frac{dA_3}{dz} = \frac{2i\omega_3 d_{eff}}{k_3 c^2} A_2 A_1 e^{+i\Delta kz} \tag{5-5}$$

Where A_1, A_2, A_3 represent the electric field amplitude of the mid-IR signal, the 1064 nm pump, and the upconverted 814 nm SFG, respectively. d_{eff} is the nonlinear coefficient (14 pm/V typ. for PPLN). Δk is the phase mismatch for SFG where k_i is the wave vector for the indicated wave ($\Delta k = k_1 + k_2 - k_3$), c is the speed of light, ω_i is the optical frequency for the indicated wave, and z is the propagation direction along the optical axis in the nonlinear crystal. In this case, there is no rate equation for the pump A_2, as it is assumed to be high enough in intensity that depletion is negligible and thus A_2 is constant.

Another important consideration for optimizing the output power of the SFG device is the beam overlap inside of the crystal. The most straightforward way to treat this

problem for tightly focused gaussian beams is using overlap integrals as covered by Guha and Falk [40,41]. While the treatments are derived for single pass, we have found that using the above cavity simulation to estimate the circulating power coupled with Guha and Falk's approach gives results that agree well with the experimental data. The derivation for the formula itself is several pages and so is omitted here, although it can be found in its entirety in the cited works by Guha and Falk. The general idea is to integrate over the entire plane of the output crystal facet to obtain the output signal power for a given pump and idler power. The result of the derivation is the complex double integral h with many variable terms, found below:

$$h = \left(\frac{1}{4\xi_4}\right) I,$$

$$I = \int_0^1 \int_0^1 dz_1 dz_2 \times \frac{\exp[i\Delta kl(z_1 - z_2)] \exp\left[-\left(\frac{4B^2}{\alpha}\right)(z_1 - z_2)^2 f\right]}{(z_1 - A)(z_2 - A_1^*) + C_1} \tag{5-6}$$

$$k = \frac{k_1}{k_2}$$

$$B = \frac{\rho}{2}\left(\frac{l(k_1+k_2)}{2}\right)^{\frac{1}{2}}$$

$$\xi_1 = l/(2z_{R1})$$

$$\xi_2 = l/(2z_{R2})$$

$$\xi_3 = \frac{\xi_1\xi_2(1+k)}{\xi_2+k\xi_1}$$

$$\xi_4 = \frac{\xi_1 + k\xi_2}{1+k} \tag{5-7}$$

$$\alpha = \frac{\xi_1 + k\xi_2}{(1+k)\xi_1\xi_2}$$

$$A_1 = \frac{1}{2} + \frac{i}{4}\left(\frac{1}{\xi_3} + \frac{1}{\xi_4}\right)$$

$$C_1 = -\frac{1}{16}\left(\frac{1}{\xi_3} - \frac{1}{\xi_4}\right)^2$$

$$z_3' = \frac{1}{2} + \frac{i}{2\xi_3}$$

And

$$f = \frac{(z_1 - z_3')(z_2 - z_3'^{*})}{(z_1 - A_1)(z_2 - A_1^*) + C_1} \tag{5-8}$$

Where * denotes complex conjugates where appropriate. The resulting integral is $h((\Delta kl), \xi_1, \xi_2, k, B)$ where (Δkl) represents the phase mismatch for a crystal of length l, with phase mismatch for quasi-phasematching determined by $\Delta k = k_1 + k_2 - k_3 - \frac{2\pi}{\Lambda}$, where $k_i = \frac{2\pi n_i}{\lambda_i}$ and Λ is the period of the periodically poled crystal. ξ_i is the focus factor, found by dividing the length of the crystal by twice the Rayleigh length of the given beam inside of the crystal (also known as the confocal parameter). $k = k_1/k_2$ is the ratio of the wavenumbers of the pump and idler, and B is a term representing the phase walk-off. Since we are using PPLN, $B = 0$ for all cases. By varying the phase mismatch through adjusting the temperature of the PPLN, the value of the integral h can be maximized for a given

crystal. By doing this, h is then only a function of the focus factors, allowing us to see how adjusting the size of the beams in the crystal may affect the output power. The goal is to maximize h for a given crystal. This treatment can be found in the results section, as it is relevant to future improvements for the device. The simulation work above is compared to the experimental results in the following section.

5.4 Results

5.4.1 Output Power Characterization

The leaking 1064 nm power was experimentally measured with the dichroic mirror and PPLN crystal in the cavity. This allows accurate characterization of the total cavity loss for the simulation, while also enabling estimation of the circulating intracavity power for PE estimation. Fig. 5-3 shows the experimental results compared with our simulation results. The 1064 nm power is measured after the output coupler and is used to determine the circulating power in the cavity for both the QE calculation and the SFG calculation. To simulate this, the cavity simulation from earlier is used with all known loss values from coatings and other intracavity components accounted for. The agreement between simulation and experiment is good, with the simulation overestimating slightly with respect to the best fit line. This agreement means that we can be confident that the input circulating power estimates for the SFG simulation are accurate with respect to the real cavity setup. For all plots, a 3% error bar is applied, as this was the dominant error from the

uncertainty of the Thorlabs S401C photodetector used. However, given the size of the red square markers used to designate the experimental data, these bars are not always visible. In this case, the marker itself is an accurate representation of the experimental error.

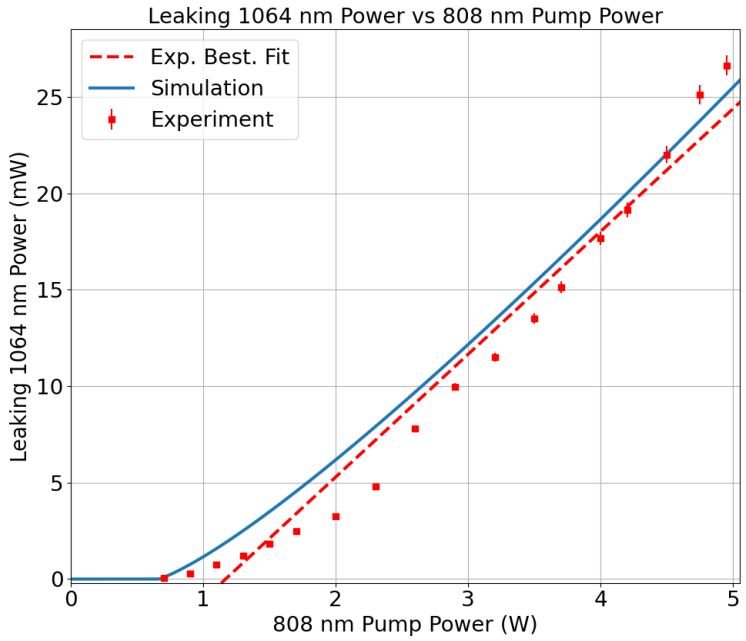

Figure 5-3 Measured and simulated leaking 1064 nm power vs 808 nm pump power. Error bars are present on all markers but are smaller than the data markers for most points. The solid blue line is the simulation, while the dashed red line is the line of best fit for the experimental data.

After characterization of the circulating 1064 nm power, the next step is to measure and estimate the produced SFG power. The results are shown in Fig. 5-4, where again we see good agreement between the simulated predictions and the experimental line of best fit. For the simulation work, the cavity power from the simulation is used as input to the nonlinear wave equations and the beam overlap

simulation as described in the Methods section. The simulated SFG power is estimated just after the output facet, and so need to be adjusted for the transmission of the OC and filters before the detector. A maximum SFG power of 8.5 mW is measured at the detector and needs to be adjusted for optical filter transmission. The output coupler (T=99.9%), 1064 nm notch filter (Thorlabs NF1064-44, T=99.57%), and bandpass filter (FBH820-10, T=90%) are considered to estimate the SFG power just after the PPLN output facet. The adjusted maximum SFG power obtained just after the PPLN output facet was 9.5 mW for 26.3 mW of input mid-IR power measured just before the PPLN input facet, leading to a measured power efficiency of 36.0%.

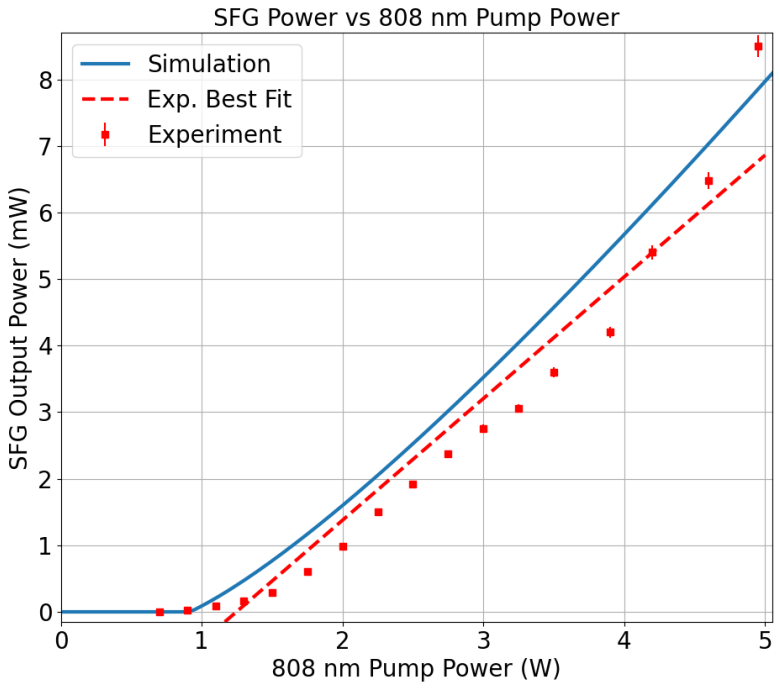

Figure 5-4 Measured and simulated output SFG power vs 808 nm pump power. Error bars are

present on all markers but are smaller than the data markers for most points. The solid blue line is the simulation, while the dashed red line is the line of best fit for the experimental data.

5.4.2 Beam Overlap Characterization

Here we evaluate the overlap of the pump and idler beams in the nonlinear crystal, and see if any further improvements could be made. From Eq. 5-7, the focus factors for the pump and idler for refractive indices of 2.15 and 2.08 and beam radii of 110 μm and 55 μm are $\xi_1 = 0.31$ for the 1064 nm pump and $\xi_2 = 4.2$ for the idler, respectively. This shows that the idler beam is overfocused while the pump beam could be focused further, and so there is room for improvement in terms of device efficiency. In practice, further focusing of the pump beam is difficult to achieve with the hemispherical cavity, as cavity simulation suggests further decreasing the beam size in the PPLN would require a larger thermal lens, which could lead to significant cavity instability. However, since a different cavity design could theoretically be utilized, we will examine two cases. First, we will look at the value of h for the current device and see how changing the idler focus factor could lead to further efficiency gains. We will then calculate a second curve for h assuming an ideal pump beam in the nonlinear crystal as well, with a target focus factor of 2.3. In the following discussion, the pump focus factor is assumed fixed since we cannot significantly change the focus factor for the current cavity design. Both curves have been optimized for ideal phase matching as well. The results can be found below in Fig. 5-5:

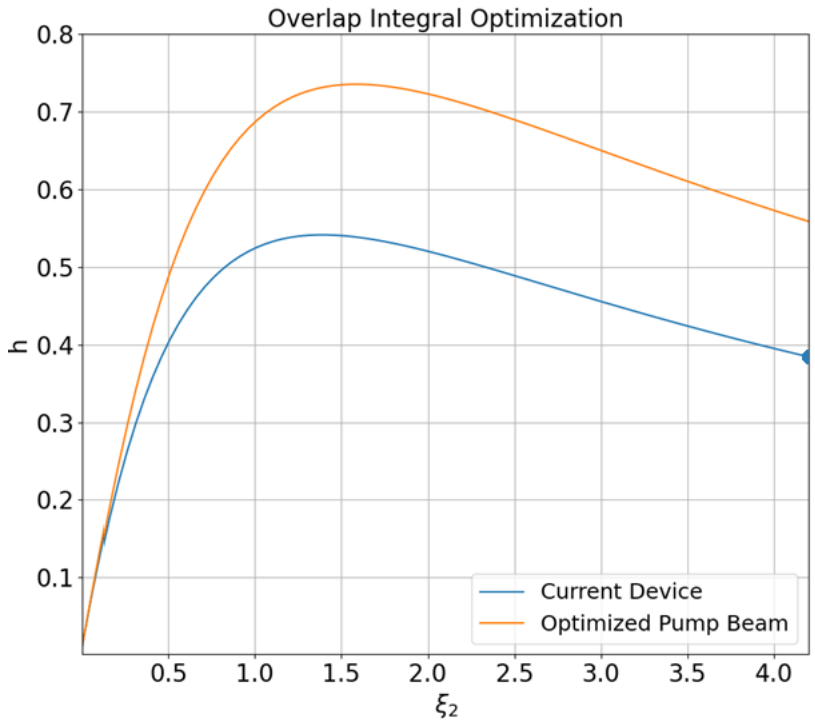

Figure 5-5 A plot of the overlap integral for the current device (blue curve) as well as a hypothetical fully optimized device (orange curve). The current device efficiency is marked with the blue circle. We can see that there are significant efficiency gains to made with the current device even if the pump beam is not changed due to cavity design restrictions.

We can see that there are significant efficiency gains that could be made to the current device structure. Starting with the blue curve representing the current device and the fixed pump focus factor of 0.31, the current value of h is 0.385 for $\xi_2 = 4.2$. However, since the idler beam is overfocused, we could relax the beam focusing such that we hit the maximum value of h, which is 0.541 at a idler focus factorof $\xi_2 = 1.39$ (or a radius of 94 microns vs the current 55). This alone would correspond to an increase in efficiency of $\sim\frac{0.541}{0.385} = 40.5\%$, increasing the power

efficiency and quantum efficiency to 50.6% and 11.9% respectively. This will require reconfiguring the focus lens and collimator used for the idler arm of the experiment, which can be accomplished by using a lower power focusing lens, which we do not currently have to perform this experiment.,That being said, it is otherwise a straightforward change to make. A harder change is optimizing the pump beam, as achieving the target focus factor of 2.3 requires a pump beam radius of 40 microns. Using ReZonator, there are no configurations that can achieve such a small beam size in the PPLN while retaining the compact hemispherical cavity. However, if we assume an equally compact alternate cavity design is possible, the maximum value of h is 0.735 with an idler focus factor of 1.58 (or an idler radius of 88 microns). In this case, that would represent a total efficiency gain of 91% over the current device, with theoretical power and quantum efficiencies of 68.8% and 16.1% respectively. This is for a circulating power of 17W, which is about 6 times lower than that required for Dam et al's record quantum efficiency of 20%, which required 100W of circulating power in the cavity. On paper, if we were to apply this circulating power to the theoretical optimized device, quantum efficiencies >90% seem possible. Despite this, an important consideration that our treatment lacks are the effects of temperature and intense focusing inside of the nonlinear medium. Tightly focused gaussian beams for cavity powers as high as Dam et al's could potentially lead to significant thermal effects if not outright damage to the crystal, which is a concern that would require more detailed modelling to overcome. One possible work-around is to move to a pulsed regime, where intensities can be

maximized for short periods of time, limiting the potential for damage. A recent example of this is from Huang et al. in 2021, where they utilized ultrafast lasers to achieve a quantum efficiency of 80% in the mid-infrared [42]. Additionally, there are trade-offs to using tightly focused gaussian beams depending on the application. Tighter focuses inside of the nonlinear medium coupled with longer crystals significantly limits the field of view (FOV), which can be limiting for imaging and remote sensing applications. As our target domain is optical satellite communication, the FOV is already quite low compared to other domains, and so this is less of a concern. It still bears repeating however and it shows that tightly focused gaussian beams, while potentially more efficient, are not always a suitable solution.

5.4.3 Device Linearity and Limit of Detection

An important practical and theoretical consequence of upconversion is that the SFG output power should have a linear dependence with respect to input mid-IR signal power. It is important to validate this, as linear responses are typically desirable for photodetectors, and a nonlinear response would introduce additional difficulties when using the device. To ensure linearity, the SFG power was measured as a function of input mid-IR light power. Then, we produce a log-log plot using base 10 logarithms and fit a linear curve to the data. In theory, the closer the slope of the curve is to 1, the more confident we can be that the y variable depends linearly on the x variable. The results are plotted in Fig. 5-6, where we can see the equation for the line of best fit is $y = 1.0059x - 0.5864$. As our slope is quite close to 1, we

can confidently say that the SFG upconversion demonstrates a linear dependence on the input mid-IR signal power.

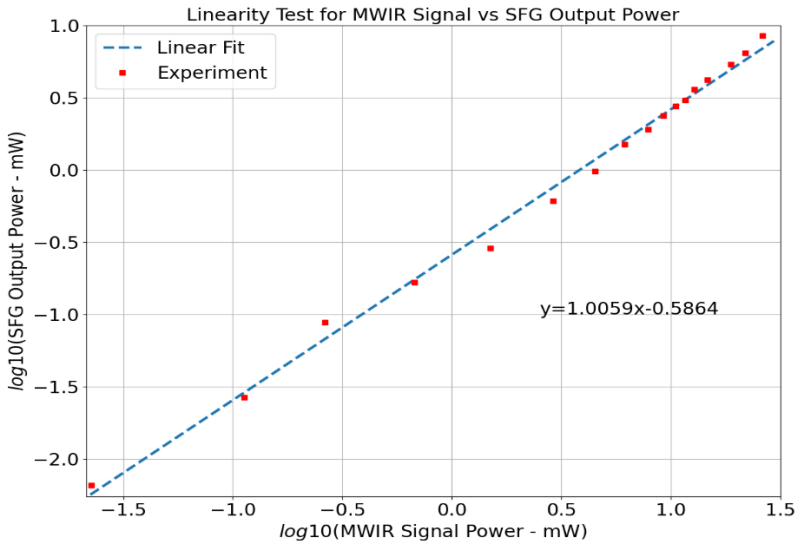

Figure 5-6 A base 10 log-log plot of the SFG power dependency on the input signal power. This is done to check linearity, as in theory the closer the slope of the line of best fit to 1, the more confidently we can say the SFG has a linear dependence on input mid-IR power.

We also tested the limit of detection using the equipment on hand. The lowest power we measured was 53 nW (-42.8 dBm) of SFG corresponding to ~150 nW of DFG. The results are plotted in units of dBm in Fig. 5-7 to demonstrate the continued linearity on the low end of the power scale. The error bars represent a 3% error from the detector and an additional flat error from the limited precision of the oscilloscope used to read the output voltage from the detector (~2 mV). This is why the error bars get more pronounced with decreasing magnitude of the measured power. While the selected photodetector could detect lower powers than this, we ran into issues with electronic noise introduced by the old model of oscilloscope

being used for the readings. A full re-design of the detector circuit using more modern components would allow us to provide an experimental demonstration of the practical limit of detection. As we currently lack the equipment to measure the limit of detection, a theoretical value for the noise equivalent power for this detector can be found in the Discussion, alongside other important noise considerations.

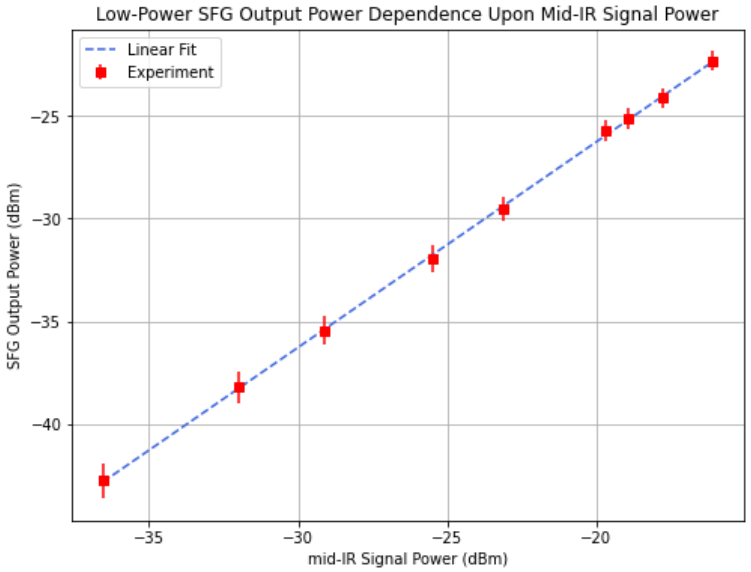

Figure 5-7 A plot in dBm showing the lowest powers detected in our experiments. In theory much lower powers can be detected, but the detection electronics proved to be insufficient for this purpose. A theoretical discussion of the limit of detection is included in the discussion as a result.

5.4.4 Length Dependence

Since our group has in-house PPLN fabrication capabilities, several lengths of PPLN were produced with the same period of 22.75 μm. Each sample was tested to see if the measured conversion efficiency deviated from the theoretical expectation, and to test the variability in PPLN quality between samples. The results

are shown in Table 5-1 below.

Table 5-1: Nonlinear Crystal Length Dependence Results

PPLN Length (mm)	Measured Power Efficiency (%)	Length Corrected Power Efficiency (%)	Nonlinear Conversion Efficiency per unit length (%/W-cm)
35	25.34	34.39	1.61
43	31.13	34.38	1.61
47.5	36.0	36.0	1.69

We see that, as expected, the conversion efficiency drops with nonlinear crystal length. For the third column, "length corrected" refers to adjusting each crystal's conversion efficiency by the ratio between the crystal length with respect to the longest crystal. For example, to length correct the second sample, the conversion efficiency is multiplied by $\frac{47.5}{43} = 1.10$, since SFG power is linearly proportional to PPLN length for small mid-IR intensities [43]. In theory, if all PPLN are identical, then the length corrected conversion efficiencies would be identical. We can see some variance in the corrected conversion efficiencies, though they are all within ~1.6% of the expected value of 36%. This can be attributed to manufacturing errors in the PPLN coupled with variations in alignment caused by removing and inserting different PPLN samples repeatedly. This is also shown with the conversion

efficiency per unit length in the final column, which was found by dividing the SFG power by the product of the input idler power and the 808 nm pump power used. In a well-poled crystal, there is minimal dependence on crystal thickness, so long as the crystal is thick enough to fully contain both the pump and idler beams to avoid beam clipping. However, manufacturing errors during the domain inversion of the crystal could lead to imperfect poling (i.e. domain inversion not remaining vertical with respect to the input beam), and poling may not be uniform in the direction perpendicular to the input beam, leading to a position dependence as well. On top of this, lithium niobate does not have a high thermal conductivity, meaning the closer the beam is to the surface of the PPLN, the better the thermal dissipation is. All of this can account for potential differences between PPLN samples. The main takeaway is that there is no significant difference between any of the PPLN samples tested, and longer crystals directly lead to higher power efficiencies as expected.

5.4.5 Stability and Beam Profile

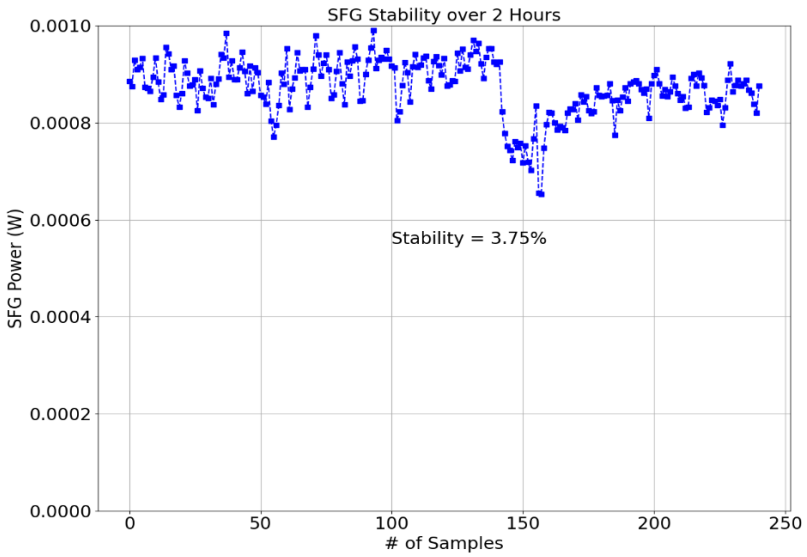

Figure 5-8 The measured SFG power fluctuations over a two-hour period to determine stability. Each sample represents a 30 second interval, after which SFG power was measured.

Stability over time is another important metric for an optical instrument. To test this, the DFG module was held at a constant input power while the SFG measurement was allowed to run freely for two hours with no adjustments. The SFG power was measured over this two-hour period, and then the stability is calculated as the root mean square deviation of the SFG dataset. The experimental measurements are plotted in Fig. 5-8. To keep the number of data points reasonable, the SFG power was sampled every 30 seconds during the two-hour experiment. Typical stability values for nonlinear DPSS-based lasers are 1-4% [12,44,45]. The stability of the SFG upconversion was found to be 3.75% after 2 hours, which

is in line with this range. The dip in power around 140 samples is due to a sudden drop in power from the DFG input module because of instability from using an unpolarized 808 nm pump source and is not due to a change in performance from the SFG module.

5.4.6 Temperature Dependence

Finally, the temperature dependence of the SFG power was measured to ensure the poling period was accurate and the developed mid-IR detector has sufficient temperature tolerance for practical applications. Experimentally, the temperature of the PPLN was varied by 1 degree increments, tracing out a temperature tuning curve. In the simulation, the temperature dependence of the refractive index of the lithium niobate was modelled using Sellmeier equations [46]. The results can be seen in Fig. 5-9. The FWHM of the experimental curve is ~8 degrees Celsius, while the theoretical curve fits well. 8 degrees Celsius temperature tolerance should be sufficient for most of the practical applications. In general, there is good agreement, although the peak is slightly off from the experimental value, perhaps due to experimental error and not allowing enough time for the crystal to reach thermal equilibrium. We see that focused gaussian beam theory can also account for the elongated "tail" on the left-hand side of the experimental data. This is a well-known phenomenon that occurs when one or both of the pump and idler beams deviate from plane wave behavior and begin to transition into focused gaussian beams. This can also be due to ellipsoidal beams or tip/tilt misalignment of one or both beams with respect to the optical axis [39–41]. In our case, it is likely due to strong

focusing of the idler beam and moderate focusing of the pump, leading to a confocal parameter smaller than the length of the nonlinear crystal. If a broader temperature response is required, the use of chirped nonlinear gratings will help at the cost of conversion efficiency [43]. Alternatively, Barh et al. demonstrated ultra-broadband mid-IR upconversion by physically translating a fanned grating PPLN crystal to achieve upconversion from 3.6 – 4.85 microns in the mid-IR [16,19].

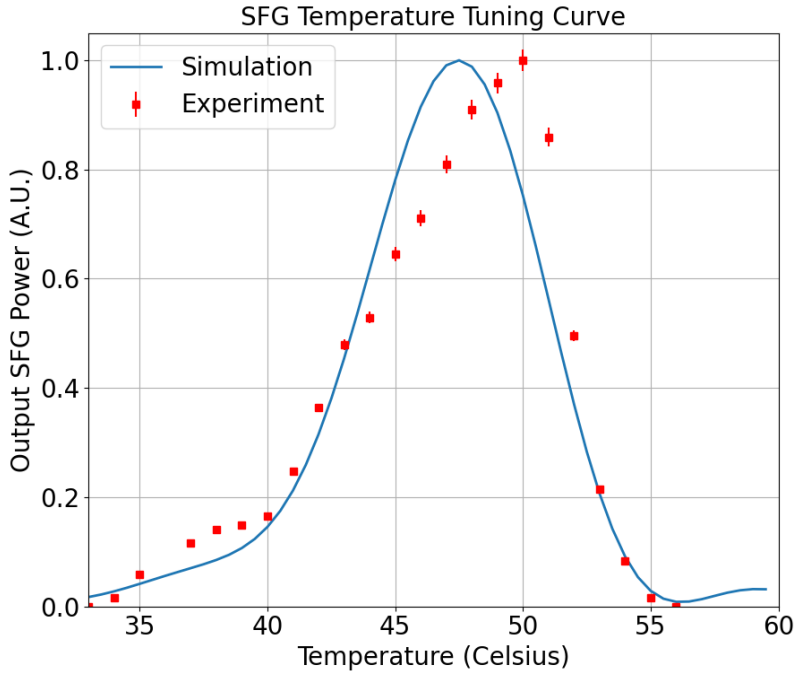

Figure 5-9 Theoretical temperature tuning curve calculated via Sellmeier equations compared to experimental data. The solid blue line is simulated while the red dots are experimental data.

5.5 Discussion

The results show that we have achieved a power conversion efficiency of 36% (QE 8.5%) with good agreement to a theoretical treatment using focused gaussian beams. We also see that the main area for improvement is in the overlap between

pump and idler, with a potential 40% gain to be implemented by defocusing of the idler beam. This will be implemented in a future iteration after simulating the appropriate focus lens and fiber collimator to pair with the signal, as in the future we anticipate the idler beam originating from a fiber-coupled source. This alone raises the PE to 50.6% (QE 11.9%), and we've seen a fully optimized pump beam could theoretically push the device to a PE of 68.8% (QE 16.1%). This is for an 808 pump power of 5W and a circulating power of 17W 1064 nm, which means comparable performance to Dam et al's intracavity conversion record of 20% with significantly less circulating power required. One potential way to surpass the intracavity record set by Dam et al. would be to increase the 808 nm pump power, as the Nd:YVO4 easily supports 10W pumping. Assuming a linear relation, this would double the circulating 1064 nm power and thus the efficiency, meaning that our current device with an optimized idler beam could reach a PE of 101.2% (QE 23.8%), and a fully optimized cavity redesign might reach a PE of 137.6% (QE 32.1%) which would represent a new experimental record. Another method of improving the efficiency would be optimization of the cavity itself, mainly by improving the coatings further on any intracavity components. Simulation work suggests this could lead to further improvement of the circulating 1064 nm power for a given 808 nm pump, although the coatings are already performing well so this may not be worth the cost. Regardless of the selected path forward, there is significant work to be done to implement this, and there may be additional problems like the aforementioned thermal effects that limit the total efficiency. However, the

theoretical analysis is promising and shows that there is a possibility for our device to meet and even exceed the current state of the art for intracavity upconversion detectors, which is an exciting avenue for future work. Of course, for readers interested in developing improved mid-IR upconverters, the FOV required by the intended application must be considered heavily as well, as focused beams do limit FOV heavily.

The noise properties of upconversion detection are important as well. While we currently lack the necessary equipment to present a detailed treatment of upconversion noise considerations, this has been covered thoroughly in the literature. Specifically, Pedersen et al. and Barh et al. have theoretically and experimentally determined the various noise limits due to thermal considerations, SPDC, and other relevant phenomena [7,18,20]. Another consideration is phase noise and intensity noise, which is relevant depending on the modulation format used, given the device is intended for free space communication. This requires characterization of the power spectral density of the phase noise, typically using an RF spectrum analyzer. Unfortunately, we do not currently have access to this equipment, which is why the treatment is missing from this study. We hope to perform this in a future study alongside gigabit modulation detected via upconversion. However, Gray et al. and Tawfieq et al. performed a similar analysis for an upconversion detector in 2020, and so interested readers can refer to their manuscript for a breakdown on the contributions from shot noise, relative intensity noise, and other phenomena [47,48].

Another important metric for upconversion detection is the effective noise-equivalent power (NEP) achievable in the mid-infrared via the use of upconversion detection. As one might expect, higher conversion efficiencies lead to lower effective NEPs, which can broadly be considered an increase in sensitivity for a given measurement bandwidth. First, we must characterize the NEP limit from the upconversion process alone. This has been extensively derived by Pedersen et al. and Barh et al. and can be calculated from the following formula [7,18]:

$$NEP = \frac{\sigma E_p \omega_{IR}}{\omega_{up}\eta_{up}\sqrt{\Delta f}} \tag{5-9}$$

Where E_p is the energy per photon, η_{up} is the upconversion efficiency, σ is the square root of the mean number of events for a Poisson distribution, Δf is the frequency bandwidth, and ω represents the mid-IR and upconverted optical frequencies. Now that the upconversion NEP is known, we must consider two different regimes for potential detector set-ups. The first is represented by the formula above, and is valid when the electronic noise of the detector is negligible relative to the magnitude of the upconversion NEP. In the second, the electronic noise in the detector dominates, and the NEP of the upconversion setup can be estimated as:

$$NEP = \frac{\omega_{IR}}{\omega_{up}\eta_{up}} NEP_{det} \tag{5-10}$$

We can see both cases have the same dependence on upconversion efficiency. Our quantum efficiency may be 42% that of the record set by Dam et al., but it can still produce a respectable NEP. Using previous estimates by Pedersen et al. as a baseline, our device is theoretically capable of a floor for upconversion noise of $\sim 1.7 \cdot f\mathrm{W}/\sqrt{\mathrm{Hz}}$. This would be for upconversion at 810 nm with an integration time of 1 second [18]. This is still suitable for a number of high sensitivity applications and outcompetes direct mid-infrared detection with low-bandgap semiconductor materials.

Another goal of this work was to make the mid-IR detector more compact to enable portable remote sensing and gas detection applications. The current cavity length is <8 cm and is mainly limited by the length of the PPLN. As we tested multiple lengths of PPLN, we have shown that PE values >25% can be maintained for crystal lengths as low as 35 mm, so there is potential to reduce this further depending on the specific application needs. We are also currently pursuing professional packaging in-house, and we have machined a prototype module with dimensions of 3.75 x 3.0 x 8.0 cm. Through redesigning the optical lens train coupling the mid-infrared light into the cavity according to the findings of the simulation work, we hope to reduce this further in the future. This should allow an upconversion module to be used in a wide variety of applications where a portable, high quality room temperature mid-infrared detector is needed. We also hope to demonstrate a mid-

infrared free space optical link in atmosphere as part of the High Throughput Secure Networks program in Canada. This is part of a broader goal to demonstrate gigabit speed mid-infrared communication for atmospheric mitigation purposes and will be explored in more detail in future work from our group.

5.6 Conclusion

In conclusion, we have demonstrated a compact intracavity SFG upconversion with an experimental power efficiency of 36.0% (quantum efficiency 8.5%). This was achieved in a compact packaged form factor of 3.75x3.0x8.0 cm, making it suitable for remote sensing, free space communication, and other applications where a compact, high speed, high sensitivity mid-infrared detector is required. The experiment generated a maximum upconverted output power of 9.5 mW of 814.2 nm for 26.3 mW of input 3469 nm light using bulk PPLN. The experimental results agree well with theoretical predictions from cavity simulations and focused gaussian beam theory. This has been achieved using a novel linear cavity design to for ease of alignment and to minimize size. Given the short time scale of nonlinear optical phenomena, the input mid-IR signal could be modulated at high speed to enable a new class of detectors for mid-IR optical communication links. In future work, we hope to improve the device efficiency considerably according to the optimizations identified by the simulation work, which could lead to almost double the power and quantum efficiency for the same pump power. We also aim to demonstrate long-distance communication at gigabit signal rates using a high-speed

modulated mid-infrared source to further emphasize the usefulness of this module for free space optical communication. The module also has other applications in mid-infrared spectroscopy, gas detection, autonomous vehicle LIDAR, imaging, and more.

5.7 Acknowledgements

The authors thank the National Research Council of Canada for help identifying collaborators for this work.

5.8 References

1. A. Trichili, M. A. Cox, B. S. Ooi, and M.-S. Alouini, "Roadmap to free space optics," J. Opt. Soc. Am. B, JOSAB **37**, A184–A201 (2020).
2. E. Leitgeb, T. Plank, M. S. Awan, P. Brandl, W. Popoola, Z. Ghassemlooy, F. Ozek, and M. Wittig, "Analysis and evaluation of optimum wavelengths for free-space optical transceivers," in *2010 12th International Conference on Transparent Optical Networks* (2010), pp. 1–7.
3. L. Flannigan, L. Yoell, and C. Xu, "Mid-wave and long-wave infrared transmitters and detectors for optical satellite communications—a review," J. Opt. **24**, 043002 (2022).
4. A. Rogalski, P. Martyniuk, M. Kopytko, and W. Hu, "Trends in Performance Limits of the HOT Infrared Photodetectors," Applied Sciences **11**, 501 (2021).
5. A. Rogalski, "Infrared detectors: an overview," Infrared Physics & Technology **43**, 187–210 (2002).
6. P. Martyniuk, J. Antoszewski, M. Martyniuk, L. Faraone, and A. Rogalski, "New concepts in infrared photodetector designs," Applied Physics Reviews **1**, 041102 (2014).
7. A. Barh, P. J. Rodrigo, L. Meng, C. Pedersen, and P. Tidemand-Lichtenberg, "Parametric upconversion imaging and its applications," Adv. Opt. Photon., AOP **11**, 952–1019 (2019).
8. R. Demur, R. Garioud, A. Grisard, E. Lallier, L. Leviandier, L. Morvan, N. Treps, and C. Fabre, "Near-infrared to visible upconversion imaging using a broadband pump laser," Opt. Express, OE **26**, 13252–13263 (2018).
9. J. S. Dam, C. Pedersen, and P. Tidemand-Lichtenberg, "Theory for upconversion of incoherent images," Opt. Express, OE **20**, 1475–1482 (2012).

10. J. S. Dam, P. Tidemand-Lichtenberg, and C. Pedersen, "Room-temperature mid-infrared single-photon spectral imaging," Nature Photon **6**, 788–793 (2012).

11. H. Pan, H. Dong, H. Zeng, and W. Lu, "Efficient single-photon counting at 1.55μm by intracavity frequency upconversion in a unidirectional ring laser," Applied Physics Letters **89**, 191108 (2006).

12. H. Pan and H. Zeng, "Efficient and stable single-photon counting at 1.55 μm by intracavity frequency upconversion," Opt. Lett., OL **31**, 793–795 (2006).

13. T.-H. Wong, J. Yu, Y. Bai, W. Johnson, S. Chen, M. Petros, and U. N. Singh, "Sensitive infrared signal detection by upconversion technique," OE **53**, 107102 (2014).

14. M. Mathez, P. J. Rodrigo, P. Tidemand-Lichtenberg, and C. Pedersen, "Upconversion imaging using short-wave infrared picosecond pulses," Opt. Lett., OL **42**, 579–582 (2017).

15. P. Tidemand-Lichtenberg, M. Aagaard, A. S. Ashik, C. Pedersen, and B. Julsgaard, "Tunable infrared upconversion module for the 1.9 to 5.5 μm range," Opt. Lett., OL **47**, 6189–6192 (2022).

16. A. Barh, C. Pedersen, and P. Tidemand-Lichtenberg, "Ultra-broadband mid-wave-IR upconversion detection," Opt. Lett., OL **42**, 1504–1507 (2017).

17. Y. Li, Y. He, Y. Wang, W. He, G. Gu, and Q. Chen, "Ultra-sensitive mid-wavelength-infrared upconversion detector," Optics & Laser Technology **168**, 109993 (2024).

18. R. L. Pedersen, L. Høgstedt, A. Barh, L. Meng, and P. Tidemand-Lichtenberg, "Characterization of the NEP of Mid-Infrared Upconversion Detectors," IEEE Photonics Technology Letters **31**, 681–684 (2019).

19. A. Barh, M. Tawfieq, B. Sumpf, C. Pedersen, and P. Tidemand-Lichtenberg, "Upconversion spectral response tailoring using fanout QPM structures," Opt. Lett., OL **44**, 2847–2850 (2019).

20. A. Barh, P. Tidemand-Lichtenberg, and C. Pedersen, "Thermal noise in mid-infrared broadband upconversion detectors," Opt. Express, OE **26**, 3249–3259 (2018).

21. L. Høgstedt, J. S. Dam, A.-L. Sahlberg, Z. Li, M. Aldén, C. Pedersen, and P. Tidemand-Lichtenberg, "Low-noise mid-IR upconversion detector for improved IR-degenerate four-wave mixing gas sensing," Opt. Lett., OL **39**, 5321–5324 (2014).

22. M. Imaki and T. Kobayashi, "Infrared frequency upconverter for high-sensitivity imaging of gas plumes," Opt. Lett., OL **32**, 1923–1925 (2007).

23. X. Gu, K. Huang, H. Pan, E. Wu, and H. Zeng, "Efficient mid-infrared single-photon frequency upconversion detection with ultra-low background counts," Laser Phys. Lett. **10**, 055401 (2013).

24. S. Wolf, T. Trendle, J. Kiessling, J. Herbst, K. Buse, and F. Kühnemann, "Self-gated mid-infrared short pulse upconversion detection for gas sensing," Opt. Express, OE **25**, 24459–24468 (2017).

25. Z. Ge, Z.-Q.-Z. Han, F. Yang, X.-H. Wang, Y.-H. Li, Y. Li, M.-Y. Gao, R.-H. Chen, S.-J. Niu, M.-Y. Xie, Z.-Y. Zhou, and B.-S. Shi, "Quantum entanglement and interference at 3 μm," Science Advances **10**, eadm7565 (2024).

26. A. Shams-Ansari, G. Huang, L. He, Z. Li, J. Holzgrafe, M. Jankowski, M. Churaev, P. Kharel, R. Cheng, D. Zhu, N. Sinclair, B. Desiatov, M. Zhang, T. J. Kippenberg, and M. Lončar, "Reduced material loss in thin-film lithium niobate waveguides," APL Photonics **7**, 081301 (2022).

27. L. Cai, Y. Wang, and H. Hu, "Low-loss waveguides in a single-crystal lithium niobate thin film," Opt. Lett., OL **40**, 3013–3016 (2015).

28. Y. Zhang, Q. Luo, S. Wang, D. Zheng, S. Liu, H. Liu, F. Bo, Y. Kong, and J. Xu, "On-chip ytterbium-doped lithium niobate waveguide amplifiers with high net internal gain," Opt. Lett., OL **48**, 1810–1813 (2023).

29. M. Bazzan and C. Sada, "Optical waveguides in lithium niobate: Recent developments and applications," Applied Physics Reviews **2**, 040603 (2015).

30. L. Lehmann, L. Grossard, L. Delage, F. Reynaud, M. Chauvet, and F. Bassignot, "Single photon MIR upconversion detector at room temperature with a PPLN ridge waveguide," Opt. Express, OE **27**, 19233–19241 (2019).

31. P. Colarusso, L. H. Kidder, I. W. Levin, J. C. Fraser, J. F. Arens, and E. N. Lewis, "Infrared Spectroscopic Imaging: From Planetary to Cellular Systems," Appl. Spectrosc., AS **52**, 106A-120A (1998).

32. A. Sijan, "Development of military lasers for optical countermeasures in the mid-IR," in *Technologies for Optical Countermeasures VI* (SPIE, 2009), Vol. 7483, pp. 32–45.

33. Y. J. Kaufman and L. A. Remer, "Detection of forests using mid-IR reflectance: an application for aerosol studies," IEEE Transactions on Geoscience and Remote Sensing **32**, 672–683 (1994).

34. D. Richter, A. Fried, and P. Weibring, "Difference frequency generation laser based spectrometers," Laser & Photonics Reviews **3**, 343–354 (2009).

35. L. Flannigan, A. Atwi, T. Kashak, D. Poitras, and C.-Q. Xu, "Compact Diode-Pumped Solid-State Laser with Intracavity Pump-Enhanced DFG Emitting at ~3.5 Microns," Photonics **10**, 1164 (2023).

36. N. I. Chunosov, "reZonator," http://rezonator.orion-project.org/.

37. I. O. Musgrave, W. A. Clarkson, and D. C. Hanna, "Detailed study of thermal lensing in Nd:YVO/sub 4/ under intense diode end-pumping," in *Technical Digest. Summaries of Papers Presented at the Conference on Lasers and Electro-Optics. Postconference Technical Digest (IEEE Cat. No.01CH37170)* (2001), pp. 171–172.

38. W. P. Risk, "Modeling of longitudinally pumped solid-state lasers exhibiting reabsorption losses," J. Opt. Soc. Am. B, JOSAB **5**, 1412–1423 (1988).

39. R. Boyd, *Nonlinear Optics*, 4th ed. (Academic Press, n.d.).

40. S. Guha and J. Falk, "The effects of focusing in the three-frequency parametric upconverter," Journal of Applied Physics **51**, 50–60 (2008).

41. S. Guha, J. O. Barnes, and L. P. Gonzalez, "Multiwatt-level continuous-wave midwave infrared generation using difference frequency mixing in periodically poled MgO-doped lithium niobate," Opt. Lett., OL **39**, 5018–5021 (2014).

42. K. Huang, Y. Wang, J. Fang, W. Kang, Y. Sun, Y. Liang, Q. Hao, M. Yan, and H. Zeng, "Mid-infrared photon counting and resolving via efficient frequency upconversion," Photon. Res., PRJ **9**, 259–265 (2021).

43. S. M. M. Friis and L. Høgstedt, "Upconversion-based mid-infrared spectrometer using intra-cavity $LiNbO_3$ crystals with chirped poling structure," Opt. Lett., OL **44**, 4231–4234 (2019).

44. N. Savage, "Ultraviolet lasers," Nature Photon **1**, 83–85 (2007).

45. G. Dudzik, J. Sotor, K. Krzempek, G. Soboń, and K. M. Abramski, "Single-frequency, fully integrated, miniature DPSS laser based on monolithic resonator," in *Solid State Lasers XXIII: Technology and Devices* (SPIE, 2014), Vol. 8959, pp. 243–250.

46. O. Gayer, Z. Sacks, E. Galun, and A. Arie, "Temperature and wavelength dependent refractive index equations for MgO-doped congruent and stoichiometric LiNbO3," Appl. Phys. B **91**, 343–348 (2008).

47. A. C. Gray, S. A. Berry, L. G. Carpenter, J. C. Gates, C. B. E. Gawith, and P. G. R. Smith, "Upconversion detection of 1.25 Gb/s mid-infrared telecommunications using a silicon avalanche photodiode," Opt. Express, OE **28**, 34279–34289 (2020).

48. M. Tawfieq, A. K. Hansen, O. B. Jensen, D. Marti, B. Sumpf, and P. E. Andersen, "Intensity Noise Transfer Through a Diode-Pumped Titanium Sapphire Laser System," IEEE Journal of Quantum Electronics **54**, 1–9 (2018).

Chapter 6. Conclusions

6.1 Summary

A proof-of-principle prototype of a MWIR transmitter using DFG and a MWIR receiver using SFG have been presented. The prototypes were experimentally characterized and compared to a novel model for intracavity DFG and SFG as well. The novel model was initially applied to SHG using a simplified plane wave model. This was iterated through successive experiments and chapters of this thesis, with the final model fully treating the two-dimensional gaussian nature of the beams interacting in the nonlinear medium. This model provides a computationally simple method of estimating the intracavity circulating fundamental power, can account for both linear and nonlinear losses, and also allows for modelling beam overlap, ellipticity, and misalignment for three-wave mixing nonlinear processes. It was shown that the intracavity transmitter design presents a compact wavelength conversion module suitable for converting C-band light into MWIR light for improved atmospheric resilience. It was also shown that the intracavity receiver design is capable of converting the incoming MWIR light back into SWIR light to use with high performance off-the-shelf silicon detectors for improved performance over direct MWIR detection. The DFG transmitter demonstrated a 10% power conversion efficiency, converting 310 mW of C-band light into 31 mW of 4399 nm light. The SFG receiver demonstrated a power conversion efficiency of 36%,

converting 26.3 mW of input mid-IR power into 9.5 mW of 814 nm light. This is comparable to other state-of-the-art wavelength conversion experiments while maintaining a significantly smaller device profile, with the machined prototype coming in at a size of 3.75 x 3.0 x 8.0 cm.

There are further advancements not covered in the published papers serving as Chapters 3 to 5 that are worth mentioning as well. The updated modelling work from Chapter 5 suggested that beam overlap in the DFG module could be significantly improved by de-focusing the C-band laser. This theory was tested in the publication *S. Rizi, Saeed,* ***L. G. K. Flannigan****, A. Chiasson, T. Kashak, D. Poitras, and C.-Q. Xu. "Efficient, Compact Mid-Infrared Sources: A Systematic Study of Intracavity Difference-Frequency Generation," Photonics 12, no. 1: 25. (2025) https://doi.org/10.3390/photonics12010025.* The author contributed to the experimental design, methodology, simulation, and manuscript drafting. The defocusing improved the overall conversion efficiency to 15.75% from the prior 10%, converting 400 mW of C-band light into 63 mW of MWIR light. This aligned very well with the predicted improvement, demonstrating the improved utility and accuracy of the new model incorporating two dimensional gaussian beams for beam overlap modelling inside of the nonlinear medium.

Finally, the modulation capabilities for the transmitter + receiver working in tandem have been partially demonstrated at the National Research Council with the help of

Ross Cheriton. The NRC facilities have high-speed modulation equipment that can modulated the C-band signal laser in the transmitter at gigabit per second speeds. The transmitter and receiver modules have been packaged and transported to the NRC, with experiments occurring during May 2025 that showed successful modulation of the DFG transmitter and SFG receiver at 20 MHz. The modulation speed was limited due to a malfunctioning high-speed silicon detector, and there was no indication that gigabit speeds would not be possible as the C-band source was successfully modulated up to 2.5 Gbps. A replacement detector was ordered and new experiments demonstrating the gigabit modulation capabilities will be taking place in the latter half of 2025. A long-distance (>1 km) free-space link using the transmitter and receiver module and a drone retrofitted with a retroreflector to simulate a complete link will take place at the NRC facility in the second half of 2025 as well.

6.2 Recommendations for Future Work

The work presented focused on the development of proof-of-principle prototypes and the novel intra-cavity three-wave mixing model to simulate the DFG and SFG module performance. While the model matched the experimental results well, there are opportunities to improve both the prototype designs to increase device efficiency and the model to allow for the prediction of how temperature gradients may affect overall nonlinear conversion efficiency. The following is a discussion covering both of these topics and how they might be improved in the future.

The goal behind using an intra-cavity approach to wavelength conversion is that the cavity resonator greatly increases the circulating fundamental wave intensity for a given pump power when compared to an equivalent pump power in the single pass regime. As three-wave mixing processes generally get more efficient with increasing intensity (to a point), the intra-cavity approach can be made more compact and should have significantly higher conversion efficiencies versus comparable single pass approaches. This was demonstrated experimentally for the SFG and DFG devices, and a hemispherical cavity (one planar mirror and one spherical mirror) was used due to its relative simplicity, small form factor, and ease of fabrication.

Unfortunately, there is one notable flaw with the hemispherical cavity design. In order to maximize the efficiency, the beam overlap must be maximized. However, detailed cavity simulations showed that while the C-band signal beam was well-focused, the circulating 1064 nm pump beam was under focused, leading to poor overlap. The level of focus is measured using the beam focus parameter, which is the length of the nonlinear medium divided by two times the Rayleigh range of the beam in the medium. To achieve the maximum efficiency possible, the beam factor of the pump and signal beams should be similar, and the ideal value is typically between 1.0 – 2.8 depending on the wavelengths of the two input beams. We can adjust the C-band focus factor easily, but the 1064 nm focus factor is heavily restricted by the hemispherical cavity design, and so the focus factor is limited to 0.3-0.4. This is not something that can be addressed while keeping the

hemispherical cavity, and a literature review suggests that the most straightforward approach would be to use a bowtie resonator or similar configuration instead. This would increase the cavity complexity, requiring 4 mirrors instead of two. However, this configuration offers extremely precise control over the beam waist of the circulating 1064 nm power and would easily remedy the overlap problem. This could lead to an additional 30-50% increase in overall device efficiency based on modelling predictions, and the form factor could still be kept compact enough for many MWIR optical payloads.

Another potential method to increase overall device efficiency is to improve the coating quality of the objects inside of the cavity. Losses in laser cavities affect power as a negative exponential function, meaning that even small increases in loss can lead to disproportionately large decreases in circulating power. The most straightforward way to achieve this decrease in loss is by improved AR coatings on the nonlinear medium, the gain medium, the output coupler, and especially the dichroic mirror. The dichroic mirror is the largest source of linear loss, as the coating quality is only 99.3%, compared to 99.5 – 99.85% on the other mentioned components. Our NRC colleague Daniel Poitras fabricated this dichroic mirror and did an excellent job, but it is simply quite difficult to achieve better performance while targeting high 1064 nm transmission and high 1550 nm reflectance. One method that could work is switching the dichroic so that it targets high 1064 nm reflectance and high 1550 nm transmission. According to Daniel, it is generally easier to achieve optimal reflectance versus optimal transmission. As the overall

device efficiency depends more heavily on the 1064 nm coating performance versus the C-band coupling performance (1064 nm being exponential with loss while C-band coupling is linear), it would make sense to attempt this approach in the future. This could lead to straightforward gains in performance without having to drastically redesign the laser cavity.

Finally, the model could be improved by adding a component to simulate the temperature gradient that forms in the nonlinear medium. While the current model can simulate gaussian beams interacting within the nonlinear medium, it assumes that the temperature of the nonlinear medium is fixed. At higher laser powers, a temperature gradient will form in the nonlinear medium even with sufficient cooling of the medium due to the large intensities at the beam foci and non-zero absorption coefficients. This nonuniform temperature distribution is most notable in the longitudinal direction parallel to the beam propagation direction. Given that achieving maximum efficiency depends on maintaining zero phase mismatch across the crystal, it is a reasonable assumption that at higher input powers this gradient would negatively affect overall device efficiency. One possible method to implement this model would be solving the heat conduction equation with a heat source representing the absorption in the nonlinear medium, perhaps using a finite element approach. This would greatly increase the computational complexity of the model but would open the door to modelling thermal effects in much greater detail. If multi-watt continuous wave operation using the intracavity structures is to be

achieved, this will likely be required to avoid thermal fracture and other complications from the increased pump and signal intensities.

References for Chapters 1-2

[1] T. Tolker-Nielsen and G. Oppenhauser, "In-orbit test result of an operational optical intersatellite link between ARTEMIS and SPOT4, SILEX," in *Free-Space Laser Communication Technologies XIV*, SPIE, Apr. 2002, pp. 1–15. doi: 10.1117/12.464105.

[2] R. Fields *et al.*, "NFIRE-to-TerraSAR-X laser communication results: satellite pointing, disturbances, and other attributes consistent with successful performance," in *Sensors and Systems for Space Applications III*, SPIE, May 2009, pp. 211–225. doi: 10.1117/12.820393.

[3] O. V. Sindiy, M. J. Abrahamson, A. Biswas, M. W. Wright, and J. H. Padams, "Lessons learned from Optical Payload for Lasercomm Science (OPALS) mission operations." Root, Mar. 30, 2024. Accessed: June 10, 2025. [Online]. Available: http://dataverse.jpl.nasa.gov/dataset.xhtml?persistentId=hdl:2014/45876

[4] M. Toyoshima *et al.*, "Research and development on a hybrid high throughput satellite with an optical feeder link — Study of a link budget analysis," in *2017 IEEE International Conference on Space Optical Systems and Applications (ICSOS)*, Nov. 2017, pp. 267–271. doi: 10.1109/ICSOS.2017.8357424.

[5] T. Kubo-oka *et al.*, "Development of 'HICALI': high speed optical feeder link system between GEO and ground," in *International Conference on Space Optics — ICSO 2018*, SPIE, July 2019, pp. 2158–2165. doi: 10.1117/12.2536135.

[6] A. Trichili, M. A. Cox, B. S. Ooi, and M.-S. Alouini, "Roadmap to free space optics," *J. Opt. Soc. Am. B, JOSAB*, vol. 37, no. 11, pp. A184–A201, Nov. 2020, doi: 10.1364/JOSAB.399168.

[7] E. Leitgeb *et al.*, "Analysis and evaluation of optimum wavelengths for free-space optical transceivers," in *2010 12th International Conference on Transparent Optical Networks*, June 2010, pp. 1–7. doi: 10.1109/ICTON.2010.5549009.

[8] M. A. Khalighi and M. Uysal, "Survey on Free Space Optical Communication: A Communication Theory Perspective," *IEEE Communications Surveys & Tutorials*, vol. 16, no. 4, pp. 2231–2258, 2014, doi: 10.1109/COMST.2014.2329501.

[9] Z. Huang, L. Yin, J. Wang, and H. Li, "Atmospheric Attenuation Correction Based on a Constant Reference for High-Precision Infrared Radiometry," *Applied Sciences*, vol. 7, no. 11, Art. no. 11, Nov. 2017, doi: 10.3390/app7111165.

[10] L. Flannigan, L. Yoell, and C. Xu, "Mid-wave and long-wave infrared transmitters and detectors for optical satellite communications—a review," *J.*

Opt., vol. 24, no. 4, p. 043002, Mar. 2022, doi: 10.1088/2040-8986/ac56b6.
[11] G. Scalari and J. Faist, "30 years of the quantum cascade laser," *Commun Phys*, vol. 7, no. 1, pp. 1–3, Dec. 2024, doi: 10.1038/s42005-024-01888-z.
[12] X. Pang *et al.*, "Free-Space Communications Enabled by Quantum Cascade Lasers," *physica status solidi (a)*, vol. 218, no. 3, p. 2000407, 2021, doi: 10.1002/pssa.202000407.
[13] F. Xie *et al.*, "Watt-Level Room Temperature Continuous-Wave Operation of Quantum Cascade Lasers With λ >10 μm," *IEEE Journal of Selected Topics in Quantum Electronics*, vol. 19, no. 4, pp. 1200407–1200407, July 2013, doi: 10.1109/JSTQE.2013.2240658.
[14] S. Guha, J. O. Barnes, and L. P. Gonzalez, "Multiwatt-level continuous-wave midwave infrared generation using difference frequency mixing in periodically poled MgO-doped lithium niobate," *Opt. Lett., OL*, vol. 39, no. 17, pp. 5018–5021, Sept. 2014, doi: 10.1364/OL.39.005018.
[15] A. C. Gray, S. A. Berry, L. G. Carpenter, J. C. Gates, C. B. E. Gawith, and P. G. R. Smith, "Upconversion detection of 1.25 Gb/s mid-infrared telecommunications using a silicon avalanche photodiode," *Opt. Express, OE*, vol. 28, no. 23, pp. 34279–34289, Nov. 2020, doi: 10.1364/OE.404855.
[16] M. R. Majewski, R. I. Woodward, and S. D. Jackson, "Dysprosium-doped ZBLAN fiber laser tunable from 2.8 μm to 3.4 μm, pumped at 1.7 μm," *Opt. Lett., OL*, vol. 43, no. 5, pp. 971–974, Mar. 2018, doi: 10.1364/OL.43.000971.
[17] F. Grillot, T. Poletti, and S. Pes, "Progress in mid-infrared optoelectronics for high-speed free-space data throughput," *APL Photonics*, vol. 10, no. 1, p. 010905, Jan. 2025, doi: 10.1063/5.0230260.
[18] A. Rogalski, P. Martyniuk, M. Kopytko, and W. Hu, "Trends in Performance Limits of the HOT Infrared Photodetectors," *Applied Sciences*, vol. 11, no. 2, Art. no. 2, Jan. 2021, doi: 10.3390/app11020501.
[19] K. Karstad *et al.*, "Detection of mid-IR radiation by sum frequency generation for free space optical communication," *Optics and Lasers in Engineering*, vol. 43, no. 3, pp. 537–544, Mar. 2005, doi: 10.1016/j.optlaseng.2004.05.006.
[20] K.-D. F. Büchter, H. Herrmann, C. Langrock, M. M. Fejer, and W. Sohler, "All-optical Ti:PPLN wavelength conversion modules for free-space optical transmission links in the mid-infrared," *Opt. Lett., OL*, vol. 34, no. 4, pp. 470–472, Feb. 2009, doi: 10.1364/OL.34.000470.
[21] G. Temporao *et al.*, "Feasibility study of free-Space quantum key distribution in the mid-infrared," *QIC*, vol. 8, no. 1 & 2, pp. 1–11, Jan. 2008, doi: 10.26421/QIC8.1-2-1.
[22] N. S. Prasad, "Optical Communications in the mid-wave IR spectral band," in *Free-Space Laser Communications: Principles and Advances*, A. K. Majumdar and J. C. Ricklin, Eds., in Optical and Fiber Communications Reports. , New York, NY: Springer, 2008, pp. 347–391. doi: 10.1007/978-0-387-28677-8_8.
[23] A. P. Vandevender and P. G. and Kwiat, "High efficiency single photon

detection via frequency up-conversion," *Journal of Modern Optics*, vol. 51, no. 9–10, pp. 1433–1445, June 2004, doi: 10.1080/09500340408235283.
[24] J. S. Dam, P. Tidemand-Lichtenberg, and C. Pedersen, "Room-temperature mid-infrared single-photon spectral imaging," *Nature Photon*, vol. 6, no. 11, pp. 788–793, Nov. 2012, doi: 10.1038/nphoton.2012.231.
[25] J. S. Dam, C. Pedersen, and P. Tidemand-Lichtenberg, "Theory for upconversion of incoherent images," *Opt. Express, OE*, vol. 20, no. 2, pp. 1475–1482, Jan. 2012, doi: 10.1364/OE.20.001475.
[26] L. Høgstedt *et al.*, "Low-noise mid-IR upconversion detector for improved IR-degenerate four-wave mixing gas sensing," *Opt. Lett., OL*, vol. 39, no. 18, pp. 5321–5324, Sept. 2014, doi: 10.1364/OL.39.005321.
[27] K. Huang *et al.*, "Mid-infrared photon counting and resolving via efficient frequency upconversion," *Photon. Res., PRJ*, vol. 9, no. 2, pp. 259–265, Feb. 2021, doi: 10.1364/PRJ.410302.
[28] A. Barh, P. J. Rodrigo, L. Meng, C. Pedersen, and P. Tidemand-Lichtenberg, "Parametric upconversion imaging and its applications," *Adv. Opt. Photon., AOP*, vol. 11, no. 4, pp. 952–1019, Dec. 2019, doi: 10.1364/AOP.11.000952.
[29] R. L. Pedersen, L. Høgstedt, A. Barh, L. Meng, and P. Tidemand-Lichtenberg, "Characterization of the NEP of Mid-Infrared Upconversion Detectors," *IEEE Photonics Technology Letters*, vol. 31, no. 9, pp. 681–684, May 2019, doi: 10.1109/LPT.2019.2904325.
[30] Z. Ge *et al.*, "Quantum entanglement and interference at 3 μm," *Science Advances*, vol. 10, no. 10, p. eadm7565, Mar. 2024, doi: 10.1126/sciadv.adm7565.
[31] Y. Su *et al.*, "10 Gbps DPSK transmission over free-space link in the mid-infrared," *Opt. Express, OE*, vol. 26, no. 26, pp. 34515–34528, Dec. 2018, doi: 10.1364/OE.26.034515.
[32] R. Boyd, *Nonlinear Optics*, 4th ed. Academic Press. Accessed: Sept. 26, 2023. [Online]. Available: https://shop.elsevier.com/books/nonlinear-optics/boyd/978-0-12-811002-7
[33] Powers, Peter E. and Haus, Joseph W., *Fundamentals of Nonlinear Optics*, 2nd ed. CRC Press Taylor & Francis Group, 2017.
[34] K. Thyagarajan and A. K. Ghatak, "FIBER AND GUIDED WAVE OPTICS | Nonlinear Optics," in *Encyclopedia of Modern Optics*, R. D. Guenther, Ed., Oxford: Elsevier, 2005, pp. 472–486. doi: 10.1016/B0-12-369395-0/00700-4.
[35] "Compact Blue-Green Lasers." Accessed: June 11, 2025. [Online]. Available: https://www.cambridge.org/core/books/compact-bluegreen-lasers/87E263B69559E60DCFF9880E45C78EF7
[36] O. Gayer, Z. Sacks, E. Galun, and A. Arie, "Temperature and wavelength dependent refractive index equations for MgO-doped congruent and stoichiometric LiNbO3," *Appl. Phys. B*, vol. 91, no. 2, pp. 343–348, May 2008, doi: 10.1007/s00340-008-2998-2.
[37] W. P. Risk, "Modeling of longitudinally pumped solid-state lasers exhibiting reabsorption losses," *J. Opt. Soc. Am. B, JOSAB*, vol. 5, no. 7, pp. 1412–1423,

July 1988, doi: 10.1364/JOSAB.5.001412.
[38] L. Flannigan, A. Atwi, T. Kashak, D. Poitras, and C. Xu, "High Efficiency Pump-Enhanced Difference Frequency Generation for Mid-IR Communications," in *2024 Photonics North (PN)*, May 2024, pp. 1–2. doi: 10.1109/PN62551.2024.10621807.
[39] N. I. Chunosov, "reZonator." Accessed: June 06, 2023. [Online]. Available: http://rezonator.orion-project.org/
[40] A. E. Siegman, *Lasers*. Mill Valley, CA: University Science Books, 1986.
[41] H. Kerdoncuff *et al.*, "Cavity-enhanced sum-frequency generation of blue light with near-unity conversion efficiency," *Opt. Express, OE*, vol. 28, no. 3, pp. 3975–3984, Feb. 2020, doi: 10.1364/OE.385826.
[42] E. Mimoun, L. D. Sarlo, J.-J. Zondy, J. Dalibard, and F. Gerbier, "Sum-frequency generation of 589 nm light with near-unit efficiency," *Opt. Express, OE*, vol. 16, no. 23, pp. 18684–18691, Nov. 2008, doi: 10.1364/OE.16.018684.
[43] "RK45 — SciPy v1.15.3 Manual." Accessed: June 12, 2025. [Online]. Available: https://docs.scipy.org/doc/scipy/reference/generated/scipy.integrate.RK45.html
[44] "ode45 - Solve nonstiff differential equations — medium order method - MATLAB." Accessed: June 12, 2025. [Online]. Available: https://www.mathworks.com/help/matlab/ref/ode45.html
[45] G. D. Boyd and D. A. Kleinman, "Parametric Interaction of Focused Gaussian Light Beams," *Journal of Applied Physics*, vol. 39, no. 8, pp. 3597–3639, July 1968, doi: 10.1063/1.1656831.
[46] S. Guha and J. Falk, "The effects of focusing in the three-frequency parametric upconverter," *Journal of Applied Physics*, vol. 51, no. 1, pp. 50–60, July 2008, doi: 10.1063/1.327353.
[47] S. Salimian Rizi, L. G. K. Flannigan, A. Chiasson, T. Kashak, D. Poitras, and C.-Q. Xu, "Efficient, Compact Mid-Infrared Sources: A Systematic Study of Intracavity Difference-Frequency Generation," *Photonics*, vol. 12, no. 1, Art. no. 1, Jan. 2025, doi: 10.3390/photonics12010025.
[48] N. Lastzka and R. Schnabel, "The Gouy phase shift in nonlinear interactions of waves," *Opt. Express, OE*, vol. 15, no. 12, pp. 7211–7217, June 2007, doi: 10.1364/OE.15.007211.
[49] H. E. Major, C. B. E. Gawith, and P. G. R. Smith, "Gouy phase compensated quasi phase matching (GQPM)," in *2008 Conference on Lasers and Electro-Optics and 2008 Conference on Quantum Electronics and Laser Science*, May 2008, pp. 1–2. doi: 10.1109/CLEO.2008.4552305.
[50] T. Kashak, L. Flannigan, A. Atwi, D. Poitras, and C. Xu, "Compact intracavity mid-infrared upconversion detector – a systematic study," *Opt. Continuum, OPTCON*, vol. 3, no. 9, pp. 1660–1678, Sept. 2024, doi: 10.1364/OPTCON.533926.